Université catholique de Louvain

Faculté des Sciences, Département de Physique

Libration and obliquity of Mercury from the BepiColombo radio science and camera experiments

Gregor Pfyffer

Thèse présentée en vue de l'obtention du grade
de Docteur en Sciences

Février 2010

A mon Grand-Père

Remerciements

Je souhaite remercier toutes les personnes qui ont rendu ce travail possible. Je commencerai par remercier Véronique Dehant d'avoir accepté d'encadrer cette thèse et de m'avoir ainsi permis de travailler dans ce domaine passionnant et cet environnement enrichissant. Je remercie également Tim Van Hoolst et Pascal Rosenblatt pour leur grand investissement dans l'encadrement de ma thèse, leurs nombreux conseils et leur disponibilité. Je tiens à remercier les membres de mon jury, Bernard Piraux, Véronique Dehant, Tim Van Hoolst, Anne Lemaître, Johannes Benkhoff, Bernard Ducarme et Pascal Rosenblatt, d'avoir accepté ce rôle et d'avoir lu en détail mon manuscrit ainsi que pour leurs critiques constructives. J'aimerai aussi remercier Sébastien Le Maistre et Quentin Baire pour les nombreuses discussions que nous avons eues au sujet de mon travail durant toutes ces années et qui m'ont beaucoup aidé. Je voudrai ensuite remercier toutes les personnes qui participent à l'ambiance extraordinaire de l'Observatoire et qui en font un endroit agréable pour travailler. Un grand merci à Sébastien, Pascal, Quentin, Mikael, Tilio, Ozgür, Antony, Aurélien, Rose-Marie, Lebi, Nicolas et Juliette ainsi qu'à celles qui ont déménagé à l'IRM, Sandrine et Justine. Je pense aussi à ceux qui ont séjourné à l'Observatoire plus ou moins longtemps pendant la durée de ma thèse : Laurence Koot, Valery Lainey, Nicolas Rambaux, Olivier Verhoeven, Sébastien Lambert, Nicolas Guyennon, Séverine Rosat, Olivier de Viron et Georges Carpentier. Je remercie aussi tout particulièrement Mikael Beuthe, Georges Carpentier, Nicolas Guyennon, Quentin Baire et Marie Yseboodt dont j'ai partagé le bureau au fil des années passées à l'Observatoire. Je les remercie pour leur bonne humeur, leur disponibilité, leurs conseils avisés et les nombreuses discussions que nous avons eues. Merci également à toute ma famille pour leur soutien et leurs encouragements, et pour avoir relu en détail mon manuscrit en un temps record. Enfin, je terminerai en pensant à Cécile qui m'a accompagné et soutenu pendant toutes ces années et sans qui ce travail n'aurait pas été possible. Je la remercie de tout mon coeur pour l'amour dont elle m'entoure chaque jour. Sa patience inépuisable et sa capacité à absorber mon stress m'ont permis de mener à bien cette aventure.

Contents

Chapter 1

Introduction

Geophysics is the science that studies Earth through the measurement of the physical consequences of its state and dynamics. It is fundamentally an interdisciplinary endeavour, built on the foundations of mathematics, physics, astronomy and geology amongst others. The roots of geophysics go far back in history, but the science has blossomed only in the last century due to the enormous increase in our ability to measure the properties of the Earth and the processes unfolding below, on and above its surface. Advances in space exploration have been of a particularly great importance through satellite based remote-sensing that provide us with a unique global view of our planet and processes unravelling above, on and inside it. In addition to the enhanced ability to make crucial measurements and collect and interpret enormous amounts of data, progress in geophysics was facilitated by the acceptance of the theoretical framework of plate tectonics and mantle convection in the late 1960s. This new view of how the Earth *works* enabled deeper understanding of earthquakes, volcanoes and mountain building processes. The exploration of the Moon beginning with the first unmanned lunar probes and culminating in the Apollo missions have invigorated geophysics and extended its scope beyond Earth. The present wealth of solar system probes extends this legacy to the confines of our solar system. Today the interdisciplinary and global nature of geophysics identifies it as one of the great unifying endeavours of humanity.

This work aims to be part of the interdisciplinary effort to better understand the interior composition and processes of the planet Mercury. Mercury, which is closer to the Sun than any other planet or known natural satellite, plays an important role in constraining and testing theories of planetary formation as an end member of the planetary family.

Mercury was a messenger, and a god of trade, profit and commerce, the son of Maia Maiestas, the Roman version of Rhea, and Jupiter. His name is related to the Latin word merx ("merchandise"; compare merchant, commerce, etc.). Most of his characteristics and mythology were borrowed from the analogous Greek deity, Hermes. In the course of this work references to properties of

Mercury will be referred to as "Hermean". Mercury (the God) has given its name to a number of things in a variety of scientific fields, such as the planet Mercury, and the element mercury, which was formerly associated with it. The word mercurial is commonly used to refer to something or someone erratic, volatile or unstable, derived from Mercury's swift flights from place to place. The term comes from astrology and describes the allegedly expected behaviour of someone under the influence of the planet Mercury. The planet was given this name because it moves so fast against the background stars. Recorded observations of Mercury date back to at least the first millennium BC. Before the 4th century BC, Greek astronomers believed the planet to be two separate objects: one visible only at sunrise, which they called Apollo; the other visible only at sunset, which they called Hermes. The English name for the planet comes from the Romans, who named it after the Roman god Mercury, which they equated with the Greek Hermes. The astronomical symbol for Mercury is a stylized version of Hermes' caduceus : ☿.

Mercury is the innermost and smallest planet in the solar System, orbiting the Sun once every 87.969 days. The orbit of Mercury has the highest eccentricity of all the solar System planets, and it has the smallest obliquity (axial tilt with respect to the orbital plane). It completes three rotations about its rotation axis for every two orbits.

The perihelion of Mercury's orbit precesses around the Sun at an excess of 43 arcseconds per century; a phenomenon that was explained in the 20th century by Albert Einstein's General Theory of Relativity. Mercury is bright when viewed from Earth, ranging from -2.0 to 5.5 in apparent magnitude, but is not easily seen as its greatest angular separation from the Sun is only 28.3°. Since Mercury is normally lost in the glare of the Sun, unless there is a solar eclipse, Mercury can only be viewed in morning or evening twilight.

Comparatively little is known about Mercury; ground-based telescopes reveal only an illuminated crescent with limited detail. Mercury is also a difficult target for in-situ observations due to its proximity to the Sun and the hostile environment this implicates. Space missions need to be able to withstand very high temperatures and temperature gradients, as well as higher doses of solar wind radiation than usually subjected to when orbiting other planetary targets.

The first of two spacecraft to visit the planet was Mariner 10, which mapped only about 45% of the planet's surface in three fly-by's in 1974 and 1975, and discovering an unexpectedly strong magnetic field. The second is the MESSENGER spacecraft[1], which mapped another 30% during its fly-by of January 14, 2008. Its second fly-by in October 2008 mainly mapped terrain already

[1] The MErcury Surface, Space ENvironment, GEochemistry and Ranging (MESSENGER) probe is a NASA spacecraft, launched August 3, 2004 to study the characteristics and environment of Mercury from orbit. Specifically, the mission is to characterize the chemical composition of Mercury's surface, the geologic history, the nature of the magnetic field, the size and state of the core, the volatile inventory at the poles, and the nature of Mercury's exosphere and magnetosphere over a nominal orbital mission of one Earth year. The contrived acronym MESSENGER was chosen because Mercury was the messenger of the gods according to Roman mythology.

observed through Mariner 10 albeit with a sensibly higher resolution. A final fly-by took place in September 2009 and completed the surface mapping to an astonishing 90%. MESSENGER has imaged much of the hitherto unknown surface and is now on track for an orbital insertion on March 18th, 2011, and will then survey and map the entire planet. Only then will the scientific community get access to large amounts of data needed to validate or refute the many theories about this planet's structure and formation that have built up since then.

Mercury is similar in appearance to the Moon: it is heavily cratered with regions of smooth plains, has no natural satellites and no substantial atmosphere. However, unlike the moon, it has a large iron core, which generates a magnetic field about 1% as strong as that of the Earth (*Schubert et al.* 1988). It is an exceptionally dense planet for its small size due to the large relative size of its core. Surface temperatures range from about 90 to 700 K (more precisely -183°C to 427°C , (*Chapman* 1988)) with the subsolar point being the hottest and the bottoms of craters near the poles being the coldest. Due to Mercury's very small obliquity, the subsolar point is always located very close to the equator. At high enough latitudes the Sun never rises high above the horizon, meaning that the bottom of certain polar craters is never directly illuminated.

Earth based observations are limited to the moments of maximal solar elongation of the planet which are interspersed with long and frequent blackout periods during solar conjunctions and oppositions, rendering the process cumbersome. All other solar system bodies of interest (except Venus) are situated farther away from the Sun than the Earth and are thus less susceptible to low solar elongations.

No other terrestrial planet is more unexplored than Mercury. Dozens of spaceprobes (orbiting or landing) have been launched towards Venus and Mars each in the last 50 years. Currently three satellites and one pair of rovers are in activity on and around Mars (Mars Odyssey (2001, NASA) , Mars Express (2003, ESA), Mars Exploration Rovers (2004,NASA), Mars Reconnaissance Orbiter (2006, NASA)), and one around Venus (Venus Express (2005, ESA)), and their scientific return helps the community to push for new missions to elucidate the mysteries discovered with each probe. Mercury is the subject of renewed attention through the NASA MESSENGER probe and the ESA/JAXA joint mission BepiColombo. The former has been launched in 2004 and will enter into orbit around Mercury in early 2011 while the latter consists of two specialized probes that will orbit Mercury at different altitudes scheduled to be launched in 2014 and arriving into final orbit around the year 2020.

The European Space Agency (ESA) has defined the BepiColombo mission to Mercury as one of its cornerstone missions. BepiColombo's scientific objectives range from the determination of the gravity field of the planet to the testing of general relativity.

Mercury has a slow rotation period of 58,68 days and revolves around the Sun in 87.96 days, corresponding to a 3:2 spin-orbit resonance. For every revolution around the Sun, Mercury rotates one and a half times around its polar axis.

Thus every two solar revolutions it performs three rotations about its axis. This represents a unique spin-orbit resonance for two reasons. All other occurrences of spin-orbit resonance in the solar system involve a planetary satellite and most happen to be in 1:1 resonance around their central body. The best known example is of course the Moon's 1:1 spin-orbit resonance. From the analysis of past and present radio occultation observations as well as Mariner 10 Doppler data, Mercury's mass of 3.302×10^{23}kg and mean radius of 2439 ± 1km were determined, resulting in a mean density of $5427 \pm 10\text{kgm}^{-3}$ (*Anderson et al.* 1987). This value is of the order of Earth's and Venus' mean density and much larger than for comparably sized bodies like Mars and the Moon (see fig.1.1). This peculiarity is the cause of Mercury's Mars like surface gravity of 3.7ms^{-2} despite its significantly smaller size.

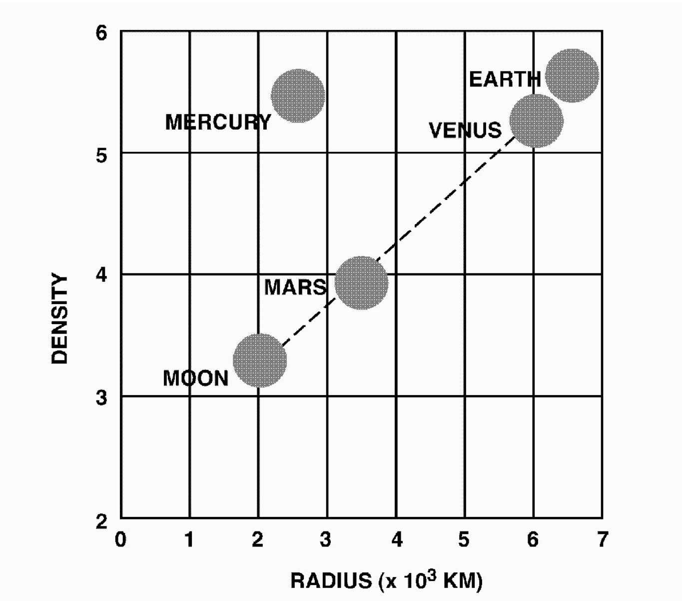

Figure 1.1: Planet bulk density in function of its radius. The main terrestrial bodies of the solar system seem to obey a linear radius over bulk density ratio, except for Mercury which is almost as dense as the *biggest* terrestrial planets despite its size being closer to the Moon and Mars.

Insight into Mercury's deep interior can be obtained from observations of variations of its uniform rotation and tidal deformations on a planetary scale, from the *BepiColombo rotation experiment*, which is the subject of this work. This experiment uses observations of the 88-day forced libration, the obliquity, and the degree-two coefficients of the gravity field of Mercury (*Peale* 1976). The gravity coefficients will be determined from the radio science experiment and the librations will be determined from the comparison of target surface positions at different times. Earth-based radar observations of Mercury surface reflections already allows the determination of the annual libration amplitude to 10% accuracy (*Margot et al.* 2007b). The future in-situ observations from the BepiColombo Mercury Planetary Orbiter (MPO) spacecraft[2] will allow us to further enhance the precision of this estimate using the on-board camera, and spatial orientation provided through the star-tracker. The position of the BepiColombo MPO as a function of time will be determined by the radio-science experiment MORE (Mercury Orbiter Radio-science Experiment).

We have performed simulations of this libration experiment under the hypothesis that all nominal instrumental precision levels will be reached and we have implemented the necessary tools for the observation analysis. The planet has an equatorial asymmetry from which a solar torque arises on Mercury. This torque causes a periodic variation of the planet's rotation with a period of 88 days, which is called the annual forced libration. The amplitude of this libration is linked to the state of Mercury's core. In the presence of a liquid core, the amplitude of the annual forced libration is about twice as large as the amplitude in the case of a completely solid planetary interior because the liquid core does (almost) not participate in the libration and the moment of inertia of the mantle is about half of the total moment of inertia of Mercury.

The gravity coefficients will be determined from the MORE radio science experiment on board the MPO. The librations will be determined from the comparison of target surface positions at different times using an on-board camera, and knowing the spatial orientation of the MPO provided through a star-tracker. The position of the spacecraft as a function of time will be determined by the radio science experiment MORE. Simulations of this libration experiment have been performed in this work and will be discussed in detail together with the necessary tools for the observation analysis implemented in chapters 3 & 4. Such an analysis requires the use of an accurate model of the rotation of Mercury, which takes into account longitudinal librations additional to the main 88day libration due to planetary perturbations on Mercury's orbit. The creation of this model together with the theoretical foundations needed are the object of chapter 2. It will also be shown that the long-period longitudinal libration amplitudes depend on the same internal structure quantities as the annual libration. Therefore we study the possibility of an independent determination of each amplitude in order to better constrain Mercury's interior structure.

In the frame of this work, we have simulated the rotation experiment and its potential outcome. We considered a known BepiColombo orbit (as defined by *Milani et al.* (2001)) affected by a variable uncertainty depending on the visibility, and therefore tracking possibility, of the spacecraft from Earth. By projecting the spacecraft orbit on the surface of the planet the distribution of potential images on the surface has been obtained. Each potential image is subject to a positioning error due to the uncertainty on the satellite position and

[2]The MPO is one of the two spacecraft of the ESA BepiColombo mission. The Mercury Planetary Orbiter (MPO) situated in a low altitude orbit optimised for planetary survey is mainly dedicated to study the surface and the internal structure of Mercury. The Mercury Magnetospheric Orbiter (MMO) is situated in a highly eccentric orbit optimised for magnetospheric studies. Both spacecraft are planned to evolve in resonant orbit so as to make certain *tandem observations* possible at regular intervals.

orientation (limit imposed by star tracker and radio science). Additional errors arise when we compare two images of the same region/target on the surface. This process is limited by the photographic resolution of the least well-resolved image and depends on the solar illumination angle. We have calculated a simulated data set, which we then used to solve for the libration amplitude. In practise, we have simulated repeated photographic measurements of selected target positions on the surface of Mercury in order to estimate the accuracy of the reconstruction of the rotational motion of the planet, as a function of the quantity of measurements made, the number of different targets considered and their locations on the surface of the planet. The observable in our system is a shift vector, constructed through subtraction of the coordinates of a ”target” on two subsequent images of it. These are then subjected to a least squares analysis yielding a value and formal error on the estimated libration amplitude. As the libration is a longitudinal motion, its absolute amplitude will be most important at lower latitudes, thus images of those regions will be of greater quality/importance to our study.

We have also determined criteria for the distribution and number of target positions to maximize the precision on the rotation determination, from which the libration amplitude is extracted. The quality of the spacecraft positioning is very important since it will greatly influence our ability to position the images taken by the spacecraft on the planetary surface and hence to reconstruct the planetary rotation. The following parameters are considered as limiting factors on the surface observability: the solar incidence on the surface seen by the camera, the solar incidence variation between two measurements of the same target, and the altitude of the spacecraft. We studied the effect of various combinations of these parameters on the libration estimation quality. In practise, we did not follow most authors who disregard the pictures above 1000 km because of the trade-off between the resolution and the amount of pictures. We have quantified the different error contributions to the observations and the associated effects on the libration determination quality. Our approach is based on general information on the mission and on required characteristics of the instruments used.

In order to assess if the goals of the rotation experiment can be achieved, a complete simulation and estimation toolchain with complex measurement and dynamic force models is required. This work aims to deliver key parts of this toolchain in order to advance our knowledge on the feasibility and precision level of the experiment under realistic circumstances.

Throughout the development of this framework the goal has always been to be able to easily expand it to any other satellite/planet couple, in particular the direct application to the future joint ESA/NASA Jupiter-Europa-System-Mission has been considered.

To study the specific estimation problem posed by the rotation experiment a dedicated software tool was developed. We will first present the features of this tool that enable the mission analysis to perform the estimation process associated with the determination of the rotation and orientation parameters of a planet or natural satellite. In a second part the specific results are applied to the BepiColombo mission and its MPO (Mercury Planetary Orbiter) spacecraft are presented and compared to those obtained by *Jehn et al.* (2004) and *Milani et al.* (2001). The mission definition in terms of measurement devices and operational orbit are also evaluated to fulfil the expected mission return.

Chapter 2

Rotation and Libration

Contents

2.1 Mercury's rotation and long term evolution

The planet Mercury is peculiar in many ways, among which its 3:2 orbital resonance stands out. Mercury rotates at an average rate of $\frac{3}{2}n$ (n = orbital mean motion) with its spin axis nearly perpendicular to its orbit plane. This value was first measured through radar observations of the planet's rotation rate made at Arecibo Observatory in Puerto Rico by *Pettengill and Dyce* (1965). The idea that Mercury has a stable rotation period of exactly two-thirds of its orbital period was first proposed by Giuseppe Colombo (*Colombo* 1965), following these observations. Before this Mercury was thought to be locked in a 1:1 resonance as it is the case for the Moon orbiting Earth.

In the time Mercury takes to perform three rotations about its rotation axis, it also performs two revolutions about the Sun. Its rotational period is thus two thirds of a Mercury year. Earth has a 23h56m04s rotational period which we call *sidereal day* and takes about 366.25 sidereal days for one revolution around the Sun which we call 1 year. The ratio of 366.25:1 thus represents the number of rotations our planet performs in the time it takes to revolve once around the Sun. For Mercury this ratio is of 1.5:1 or 3:2, as it takes 58.646 days to rotate around its axis and 87.969 days to revolve once around the Sun. The time it takes for the Sun to come back to its original position in the sky of a point on the planetary surface, *a hermean day*, consists of three rotations, or two revolutions, which equates to about 176 Earth days. One Mercury solar day thus corresponds to three Mercury sidereal days. For comparison on Earth a sidereal day is approximately 4 minutes shorter than the 24 hour solar day.

Can we say that Earth is close to a 366:1 spin-orbit resonance? No. Why? Earth's Moon slows down Earth's rotation, by about 2 milliseconds per century. This means that someday we will get to the point where 366 sidereal days (which will each be longer than the current 23h56m04s) will exactly correspond to one revolution around the Sun. But nothing will prevent the Moon from continuing to slow down Earth even further, as much as nothing stopped it in the distant past as it passed 367:1. Mercury on the other hand is in a stable "resonant" situation, which means it will not leave its current rotational state easily. Why is this the case? How has Mercury reached this state?

property	Mercury	Venus	Earth	Mars	Moon
Mass M (10^{24}kg)	0.3302	4.8685	5.9736	0.6419	0.0735
Radius R (km)	2439	6052	6371	3390	1737
a(AU)	0.38710	0.72333	1.00000	1.52366	-
e	0.20563	0.00677	0.01671	0.09431	0.0549
obliquity η(degree)	0.03	177.9	23.45	25.19	6.68
Π_{rot}(days)	58.646	243.020	0.997	1.026	27.321
Π_{orb}(days)	87.969	224.695	365.256	686.980	27.321
C_{20} (10^{-6})	60 [1]	4.404 [2]	1082.6 [3]	1960.45 [4]	203.2 [5]
C_{22} (10^{-6})	10 [1]	0.554 [2]	1.57 [3]	1844.24 [4]	22.35 [5]

Table 2.1: Mass M, mean radius R, semi-major axis a, eccentricity e, obliquity η, sidereal rotation period Π_{rot}, orbital revolution period Π_{orb} for the four terrestrial planets and the Moon. All orbital element values are given for J2000. C_{20} represents the polar flattening and C_{22} the equatorial flattening of the planetary bodies. All gravity field coefficients are given unnormalized. [1]*Anderson et al.* (1987),[2]*Konopliv et al.* (1999),[3]*Lemoine et al.* (1998),[4]*Konopliv et al.* (2006),[5]*Konopliv et al.* (2001). Other values are from *http://nssdc.gsfc.nasa.gov/planetary/factsheet/*

In table Tab.2.1 a comparison of the main physical and orbital characteristics of Mercury and the Earth and Moon is presented. Mercury has a radius about 2.6 times smaller than Earth resulting in a volume of around 5.6% of the Earth's (The volume being proportional to the radius cubed $\frac{1}{2.614^3} \simeq 5.6\%$). Mercury is closer in size to Earth's Moon. If Mercury were to have the same density as the Moon it would have a mass of $\sim 2\,10^{23} kg$, which represents around 61% of its actual mass (see Tab.2.1). This fact has fuelled many speculations as to why Mercury ended up so "heavy".

The initial rotation of Mercury was presumably faster when it first formed than today (as it is the case for all three other terrestrial planets) but through the action of tidal dissipation[1] the planetary rotation was slowed down to the present configuration. The exact mechanism on how this state initially arose is

[1]Tidal despinning is the process through which the tidal forces acting on a planetary body change its shape and orientation through dissipative mechanisms such as friction inside the planetary body.

up to this day not completely understood (*Correia and Laskar* 2009). Mercury's extreme closeness to the Sun is a key factor that enabled it to rapidly slow down to reach rotational rates commensurate with its orbital period, due to tidal friction. *Correia and Laskar* (2004) showed that the time needed to despin Mercury from an initial rotation period estimated to be around 10h would be about 300 million years without need to postulate higher than normal dissipation levels inside the planet. Following simple logic Mercury should have slowed down until it reached a synchronous rotation state (1:1 resonance); for what reason has Mercury evolved into a 3:2 resonance? A very important factor in this has been the relatively high eccentricity of Mercury's orbit around the Sun. If Mercury were to possess a synchronous rotation rate, its orbital velocity would be greater than its rotational speed around perihelion and smaller than it around aphelion. The elliptical orbit causes the intensity of the torque to change along the orbit as the planet's solar distance varies.

As the solar torques resulting from this would be greater in magnitude around perihelion than aphelion (for the obvious reason of increased solar proximity), the net effect would be to speed up the planet's rotation rendering the 1:1 spin-orbit resonance unstable. Under a spherical body assumption, i.e. considering only the torque on the retarded (or advanced) spherical bulge we can easily determine the eccentricity vs. rotation equilibrium. For the present eccentricity of $e = 0.2056$ the equilibrium rotation velocity is $\omega = 1.25685n$ and the present mean rotation rate of $3n/2$ corresponds to the tidal equilibrium rotation rate for eccentricity $e = 0.2849$. Mercury's large equatorial flattening is *the* essential ingredient to the stability of the 3:2 spin-orbit resonance, as without it the solar torque acting on Mercury would be too small to stabilise the resonance. The topography on Mercury's surface also plays a role in this process as it is not, as for the Earth, smaller than the flattening. Mercury's shape has two main deviations from the perfect spherical shape. As for Earth, there is polar flattening present, but as can be seen in table 2.1 in contrast to Earth the equatorial deformation (represented by the value of C_{22} in the spherical harmonics decomposition of the planetary gravitational field) is of the same order of magnitude as the polar deformation (represented by the value of C_{20}). Mercury's equatorial bulge gives rise to a solar torque when not properly aligned with the planet-solar axis as explained before. This mechanism is at the basis of the stability of the spin-orbit resonance and annual libration. As several resonances in the vicinity of the 3:2 resonance are also stable, how can it be explained that Mercury ended up in the present situation? The precise capture probability is very model dependent and has been the subject of many studies such as (*Goldreich and Peale* 1966; *Correia and Laskar* 2004). *Correia and Laskar* (2009) studied the capture probability in detail and found the 3:2 spin-orbit resonance to be the most likely final state, with a probability of 55% if the orbital eccentricity of Mercury descended past $e = 0.025$, and even 73% if the eccentricity descended past $e = 0.005$.

In section 2.3 the mathematical equations underlying this mechanism are studied in detail. Before this can be done the peculiarities of the spatial orientation of Mercury with respect to its orbital plane (its obliquity) will be addressed.

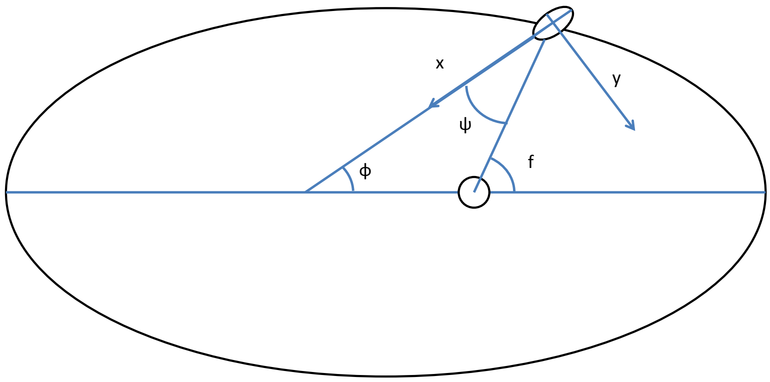

Figure 2.1: Geometry of Mercury's spin-orbit motion. Mercury's long axis makes an angle ψ with respect to the Planet-Sun direction and an angle ϕ with respect to an inertial reference axis, coinciding here with the semimajor axis of Mercury's orbital motion around the Sun.

2.2 Cassini state and nutations of Mercury

Mercury is currently locked in 3:2 spin-orbit resonance, with a very small obliquity meaning that its spin axis is almost perpendicular to its orbital plane (*Pettengill and Dyce* 1965; *Margot et al.* 2007b). The Laplace plane is defined as the plane about which Mercury's orbit precesses (such that there is a constant inclination between both planes), see Figure 2.2. The rotation axis of Mercury precesses about the orbit normal and the orbit normal precesses about the normal to the Laplace plane (*Colombo* 1966; *Peale* 1969). In the Cassini state 1, which Mercury is thought to be occupying, the rotation axis and the orbit normal remain coplanar with the normal to the Laplace plane, while the obliquity remains constant. In an idealised system, the Laplace plane would be the plane about which the orbit inclination remains constant throughout the precessional cycle. A first order approximation considering the planetary perturbations on Mercury but neglecting the effect of planetary interactions between planets, yields an orbital plane precession period of about 235ky and a constant inclination with respect to the Laplace plane [2] (*Yseboodt and Margot* 2006). In reality the motion of the orbital plane is not regular, and it is not possible to find a fixed axis in space that has a constant inclination with the orbit normal. This leads to the definition of an instantaneous Laplace plane (*Peale* 2006; *Yseboodt and Margot* 2006; *D'Hoedt et al.* 2009), about which variations in

[2]Can a Laplace plane be defined for all planets of the solar system? Yes, but as no other planet than Mercury possesses a resonant motion with the Sun it is of no use.

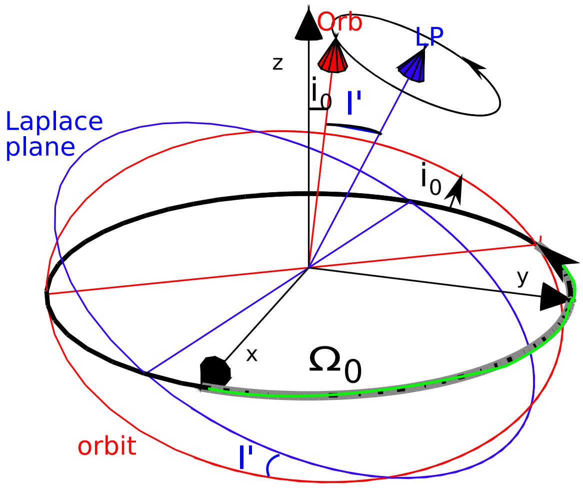

Figure 2.2: Positions of the Laplace plane and orbital plane of Mercury and their respective normal vectors. The orbital plane is precessing/rotating about the Laplace plane normal (in $\simeq$ 235ky). The x,y, and z axes represent the ecliptic reference frame, and the axes x and y form the ecliptic plane (green). This graph also defines the following angles: i_0: inclination of the orbit with respect to the inertial reference frame, Ω_0: longitude of the ascending node of the orbit with respect to the inertial reference frame, I': inclination of the orbit with respect to the *Laplace plane*. It is this inclination variation that is minimised by definition of the Laplace plane.

orbital inclination are minimised. The time interval considered and dataset used will change the position of the instantaneous Laplace plane. This would lead any reasonable person to argue that this plane is a bad choice of referential, but unfortunately the obliquity in the Cassini state must be computed with respect to the Laplace plane (see eq.(2.1) and (*D'Hoedt et al.* 2009)).

A Cassini state represents an equilibrium point in the Hamiltonian of motion (made integrable by limiting the planetary perturbations to a regular motion of the ascending node of Mercury), which was first determined empirically by *Cassini* (1693). Tidal friction drives the spin of Mercury to Cassini state 1 on a short timescale (<< 4.6Gy) from almost any initial condition (*Peale* 1974). The fact that Mercury occupies Cassini state 1 constrains Mercury's primordial obliquity to below 90°, as otherwise it could have easily drifted to Cassini state 3 (which is similar to state 1 except that the obliquity is around 180°) (*Peale* 1976). The obliquity of the final evolved Cassini state 1 is given by (*Peale* 1969):

$$\frac{C}{MR^2} = \frac{-C_{20}\left(1-e^2\right)^{-\frac{3}{2}} + eC_{22}\left(7-\frac{123}{8}e^2\right)}{\frac{\sin I}{\eta_C} - \cos I}\frac{n}{\tau}, \tag{2.1}$$

where η_C is the Cassini state 1 obliquity, I the inclination of the orbital plane with respect to the Laplace plane, and τ the precession rate of Mercury's orbit about the normal to the Laplace plane. The obliquity of the rotation axis is constant because the rotation axis is coplanar with both the orbit normal and Laplace plane normal in a Cassini state. For Mariner 10 gravitational coefficients [3], $C_{20} = (-6.0 \pm 2.0) \times 10^{-5}$ and $C_{22} = (1.0 \pm 0.5) \times 10^{-5}$ (*Anderson et al.* 1987) and $C/MR^2 \approx 0.34$, the theoretical mean obliquity obtained from eq.2.1 is equal to 1.6 arcmin, and is in agreement with recent Earth-based radar measurements by *Margot et al.* (2007b) which yield a value of 2.11 ± 0.1 arcmin. It should be noted that the theoretical value is obtained using values with very high error margins, and therefore represents only a very crude approximation. The experimental technique used by *Margot et al.* (2007b) to obtain this estimate is called Radar Speckle Displacement Interferometry (RSDI), and consists of the determination of the epoch and time delay that maximise the cross-correlation of the back-scattered radar signal at two Earth-based antennas separated by a long baseline (*Holin* 1999). Through this technique a precise measurement of Mercury's rotation rate and obliquity can be performed, with an accuracy of several arcseconds (*Margot et al.* 2007b). Future sources of obliquity measurements lie in the NASA MESSENGER mission (*Solomon et al.* 2001), and the ESA BepiColombo mission. The latter is aiming for an arcsecond precision level (*Milani et al.* 2001, *this work*). One of the main aims of this work is to determine the achievable precision level on the obliquity from BepiColombo MPO camera-based surface observations of Mercury. The exact approach and technique will be explained in detail in chapter 4.

[3] Currently no MESSENGER estimate has been published after three flyby's. This is mainly due to very unfavourable flyby geometries hampering the C_{20} and C_{22} estimation process. A significant improvement to the almost 40 years old Mariner 10 data should be available shortly after MESSENGER enters into orbit around Mercury in March 2011.

The precession period of the orbit normal and rotation axis (both are linked in the Cassini state) about the normal to the Laplace plane has been numerically calculated to be around 280ky by *Rambaux and Bois* (2004). This estimate contains indirect planetary interactions which explains its differing value from the 235ky analytical estimate cited before. If the planet does not occupy the Cassini state but is very close to it the rotation axis of Mercury will also precesses about its position in the Cassini state 1 in addition to the slow orbital precession described before (*Peale* 1974; *Rambaux and Bois* 2004). If we neglect the very slow orbital precession, the latter precession caused by the solar torque can be compared to precession of the Earth about the normal to the ecliptic. The classical analytical expression for the precession rate must be extended with a term in the equatorial flattening ($\sim C_{22}$) due to Mercury's 3:2 spin-orbit resonance. Averaging the Liouville equations without deformation effects over the orbital period of Mercury, the precession period can be derived (*Van Hoolst* 2007):

$$P_{precession} = \frac{3\pi C_m}{nMR^2}\left\{\left(\frac{-3C_{20}}{2(1-e^2)^{\frac{3}{2}}} + \frac{3}{2}eC_{22}\left(7 - \frac{123}{8}e^2\right)\right)^2 - C_{22}^2\frac{159}{16}e^6\right\}^{-\frac{1}{2}} . \tag{2.2}$$

For a solid core we have that:

$$C_m = C = 0.34MR^2 ,$$

and together with the gravitational coefficients by *Anderson et al.* (1987), this yields a precession period of 1062 years. *Rambaux and Bois* (2004) through an entirely numerical derivation obtain a value of 1066.91 years, and *D'Hoedt et al.* (2006) obtain 1065.05 years through their Hamiltonian approach. The result of the simple expression above (eq.2.2) is in good agreement with both these estimates. As the period is proportional to C_m, the mantle moment of inertia, it decreases when the size of a liquid core inside Mercury increases (because the moment of inertia of the core increases, $C_{mantle} + C_{core} = C$). *Peale* (2005) has shown that the terms in C_{22} reduce the *classical* precession period by close to 30% and also cause the precession motion to be slightly elliptical. If this precession exists today it will be difficult to measure it directly due to the long timescales involved with respect to mission lifetimes and Earth based observation backlog. However, its existence could be seen through the resulting non-coplanarity. Nevertheless this shows that another external parameter bears the signature of the planet's inner structure.

Dissipative core-mantle couplings acting together with tidal friction will damp the free precession movement, thus reducing the obliquity variations, driving the rotation axis towards the Cassini state if the orbital inclination to the invariable plane is fixed and Mercury precesses about the Cassini state at a constant rate *Peale* (1974, 2006). In reality the precession rate and inclination show large variations, due to planetary perturbations, suggesting that Mercury is unable to remain in the Cassini state. The rotation axis of Mercury is nevertheless able to accurately follow the changes in orientation of the orbit normal due to the fact that the planetary perturbations act on long timescales of 10^4 to 10^6 years compared to 10^3 years for the free precession period.

2.3 Mercury's physical librations

The interior of Mercury is not well known, and the librations offer a unique opportunity to gain a lot more information on some aspects of it. Both the amplitudes of forced librations and the period of the free libration depend on the mantle moment of inertia, which is related to the size and density distribution of the mantle, and thus represents a key geophysical parameter. By mantle we mean the solid part of the planet above a hypothetical liquid core, thus involving the crust. The mantle alone takes part in the libration movement. In the absence of a liquid core, the moments of inertia referring to the mantle coincide with the total planetary moments of inertia. The magnetic field observed by Mariner 10, if caused by dynamo action, is evidence for a liquid outer core, which, very likely contains a solid inner core according to thermal evolution models (*Stevenson et al.* 1983; *Schubert et al.* 1988; *Spohn* 1991). The recent detection of a libration amplitude of $\sim$35arcsec by *Margot et al.* (2007b) seems to confirm the existence of a liquid core. The large mean density of Mercury points towards a large core, thought to consist of iron and limited amounts of lighter elements. Sulphur is thought to be the most likely candidate (*Harder and Schubert* 2001; *Van Hoolst and Jacobs* 2003; *Schubert et al.* 1988; *Spohn et al.* 2001; *Rivoldini et al.* 2009). The concentration of sulphur and/or other light elements inside the core depends on where the planetesimals that Mercury was formed from were formed themselves in the early days of the solar system. The exact region where Mercury was accreted is of no influence on the composition of the planetesimals it was formed of. The current lack of data and Mercury's unknown origin make it impossible to constrain the core composition at the present time, but future missions such as MESSENGER and BepiColombo will help collect vital data needed to do this. If Mercury has formed close to its current position, i.e. close to the Sun, its sulphur/light element concentration is probably very low (*Lewis* 1988; *Sohl and Schubert* 2007). In the event that Mercury has formed in the same zones as Venus, Earth and Mars, its light element concentration could be a lot higher and close to that of the other three terrestrial planets [4], and for Mars a light element concentration of 14 wt.%[5] is often considered (*Van Hoolst* 2007).

The light element concentration of the core directly impacts the possible size range of the fluid core and thus the mantle moment of inertia C_m. For larger cores and smaller mantle moment of inertia, the libration amplitude increases since the libration is essentially a movement of the mantle. All things being

[4] The Earth has a core sulphur concentration of about 10wt.% .
[5] wt.% ≡ weight percentage, percentage by total weight (not volume)

equal, the libration amplitude increases with the sulphur content. It follows that the annual libration amplitude changes dramatically for different light element concentrations. The amplitude is about 21 arcsec in the case of a completely solid core, and between 36 and 78 arcsec for models with a liquid core with between 0.01 wt% and 8.6 wt% of light element (*Rivoldini et al.* 2009). This fact shows that if the mantle density can be inferred by other means, the observation of the annual libration amplitude can provide a strong constraint on the core composition.

What is a planetary libration?

A libration is a periodic variation of a uniform periodic motion (not unlike the oscillation of a pendulum about its rest state). We can distinguish two main types of libration: geometric and physical. A geometric libration is caused only by geometrical effects between the observer and the observed body/system. Physical librations are caused by gravitational interactions between celestial bodies. All planetary librations are physical librations.

Definition

In this work we call libration amplitude the maximum longitudinal angular deviation of Mercury's true rotation caused by **one specific** periodic motion with respect to its uniform rotation.

The stability of Mercury's rotation is such that the axis of minimum moment of inertia is almost aligned with the Sun-Mercury direction when the planet is at the perihelion of its orbit (*Colombo* 1965; *Goldreich and Peale* 1966). If the axis is displaced from the solar direction when Mercury is at perihelion, the solar gravitational torque acting on Mercury's axial asymmetry, averaged around the orbit, tends to realign the axis toward the Sun at perihelion thereby keeping the average spin rate at precisely $1.5n$ safeguarding the 3:2 spin-orbit resonance. If we were to view Mercury only when it is at perihelion, the axis of minimum moment of inertia would tend to librate about the direction to the Sun with a multitude of superimposed periods caused by planetary perturbations.

As seen above a physical libration in longitude results from the periodically varying amplitudes and orientations of the torques acting on Mercury's non-axisymmetric shape as the planet rotates relative to the Sun. The period of the *solar* libration is 88 days (1 Mercury year), and the amplitude and phase are determined by Mercury's gravitational asymmetry and orbital motion. In our case the perturbed movement is Mercury's uniform rotation with respect to its polar axis, (analogous to Earth's diurnal rotation). The librations of interest in this study are small periodic accelerations and decelerations of Mercury's uniform rotation. An observer in a frame rotating at the uniform rotation rate would see the planetary surface following a periodic motion about the expected uniform rotation motion. We can model this as a periodic variation superimposed on the uniform rotation. The aforementioned librations are longitudinal only due to us neglecting the planetary obliquity in the above reasoning. Latitudinal librations are caused through a similar mechanism due to a solar torque acting on North-South planetary asymmetries. Longitudinal librations impact only Mercury's rotational motion, creating a *positional shift in longitude* between the expected and actually observed position of the planetary surface. On Earth we would classify them as periodic length-of-day variations. Latitudinal librations correspond to a positional shift in latitude; the spatial orientation of the planet's polar axis changes periodically with time.

Two different families of physical librations affect Mercury's rotation, free and forced librations. A free libration is a libration at the frequency/period of an eigenmode of the planet - Sun system. Its existence does not require the presence of an external body beside the Sun, exerting a force on the planet and its frequency is deeply related to the planetary shape and composition. If it is not continuously excited at the right frequency it cannot subsist through long time scales as it is damped due to dissipation inside the planet. The second type, the forced libration is caused through an external forcing by a body of the solar System. The annual libration is caused by the interaction of Mercury and the Sun, and has a period equal to the period of the orbital path of the planet around the Sun. In the case of the annual libration the forcing on the equatorial bulge of the planet exerted by the Sun has a periodicity of 88 days corresponding to Mercury's orbital period (87.969 days = 1 Mercury year). The short-period physical libration is superimposed on any longer period libration. All librations together result in periodic variations of the spin rate about the mean value of $1.5n$, leading to deviations of the position of the axis of minimum moment of inertia from its mean $1.5n$ position.

All other *planetary induced* librations are caused through the same interaction mechanism. The periodic torque arising from the interaction of a certain solar system body with Mercury will cause a perturbation of Mercury's orbital motion, altering its position relative to the Sun and thus the solar torque acting on its equatorial bulge. This in turn will modulate the planet's libration motion and can be modelled as an additional librations of the same period as the perturbing forcing. The most important libration caused by Jupiter on Mercury has a period of 11.86 years, coinciding the time it takes for Jupiter to orbit the Sun once. The main libration caused by Venus has a period of 5.66 years corresponding to a 2:5 resonance between Venus' and Mercury's solar longitudes (orbital periods) (*Peale et al.* 2007; *Dufey et al.* 2008). Before observing the libration of Mercury, the principal dynamics have to be understood. As explained earlier the librations of Mercury arise from periodic torques applied on it by different bodies.

2.3.1 Torque exerted by the Sun on Mercury

The following paragraph will serve to how the librations can be explained from the action of the solar torque on Mercury. Let the origin $\vec{O}$ of our reference frame lie at Mercury's centre of mass. Then:

$$\begin{aligned}
\vec{M}_{☿\odot} &= \int_{☿} \vec{r} \times \rho_{☿}(\vec{r})\, \vec{g}_{\odot}(\vec{r})\, d^3\vec{r} \\
&= \int_{☿} \vec{r} \times \rho_{☿}(\vec{r})\, GM_{\odot} \frac{\vec{r} - \vec{r}_{\odot}}{|\vec{r} - \vec{r}_{\odot}|^3} d^3\vec{r}\,, \qquad (2.3)
\end{aligned}$$

where $\vec{M}_{☿\odot}$ is the torque exerted by the Sun on Mercury. ☿ and $\odot$ are the symbols we use to refer to Mercury and the Sun respectively, $\rho_{☿}(\vec{r})$ represents the density at point $\vec{r}$ inside the planet, $\vec{g_{\odot}}$ is the gravitational pull exerted by the Sun on Mercury at point $(\vec{r})$ inside the planet, which is defined as:

$$\vec{g}_{\odot}(\vec{r}) = GM_{\odot} \frac{\vec{r} - \vec{r}_{\odot}}{|\vec{r} - \vec{r}_{\odot}|^3}\,, \qquad (2.4)$$

$\vec{r}_{\odot}$ is the position vector of the Sun in our reference frame and $M_{\odot}$ stands for the solar mass, while G is the gravitational constant. The torque by Mercury on the Sun is given by:

$$\begin{aligned}
\vec{M}_{\odot☿} &= \vec{r}_{\odot} \times \vec{M}_{\odot} \vec{g}_{☿}(\vec{r}_{\odot}) \qquad (2.5) \\
&= -\vec{r}_{\odot} \times GM_{\odot} \int_{☿} \rho_{☿}(\vec{r}) \frac{\vec{r}_{\odot} - \vec{r}}{|\vec{r}_{\odot} - \vec{r}|^3} d^3\vec{r}\,. \qquad (2.6)
\end{aligned}$$

Since $\vec{M}_{☿\odot} + \vec{M}_{\odot☿} = \vec{0}$, we choose to compute $\vec{M}_{☿\odot}$ (the torque exerted by the Sun on Mercury) through $\vec{M}_{\odot☿}$ (the torque exerted by Mercury on the Sun) as the latter integral can be solved in a simpler way because the cross product lies outside the integral by the assumption of a point-like Sun. Therefore,

$$\begin{aligned}
\vec{M}_{☿\odot} = -\vec{M}_{\odot☿} &= -\vec{r}_{\odot} \times M_{\odot} \int_{☿} G\rho_{☿}(\vec{r}) \left(-\frac{\vec{r}_{\odot} - \vec{r}}{|\vec{r}_{\odot} - \vec{r}|^3} \right) d^3\vec{r} \\
&= -\vec{r}_{\odot} \times GM_{\odot} \vec{\nabla}_{\odot} \int_{☿} \frac{\rho_{☿}(\vec{r})}{|\vec{r}_{\odot} - \vec{r}|} d^3\vec{r} \\
&= \vec{r}_{\odot} \times \vec{\nabla}_{\odot} U_{☿\odot} \qquad (2.7)
\end{aligned}$$

where:

$$U_{☿\odot} = -\int_{☿} \frac{GM_{\odot}\rho_{☿}(\vec{r})}{|\vec{r}_{\odot} - \vec{r}|} d^3\vec{r}\,, \qquad (2.8)$$

is the potential energy of interaction between Mercury and the Sun. It should be stressed that this relationship between torque and interaction potential energy is not generally true but arises from the assumption of a point-like Sun. Isolating the solar mass we get:

$$U_{☿\odot} = -M_\odot \left(\int_☿ \frac{G\rho_☿(\vec{r})}{|\vec{r}_\odot - \vec{r}|} d^3\vec{r} \right) = -M_\odot V_☿(\vec{r}_\odot) \ , \tag{2.9}$$

where $V_☿$ is the well known hermeopotential, which in the Mercury principal inertial moments frame and expressed in a spherical harmonics base has the following form:

$$V_☿\big(r,\theta,\phi\big) = \frac{GM_☿}{r} \sum_{n=0}^{\infty} \sum_{m=0}^{n} \left(\frac{R_☿}{r}\right)^n P_n^m(\sin\theta) \big[C_{nm}\cos(m\phi) + S_{nm}\sin(m\phi)\big] \ , \tag{2.10}$$

where all the terms in the sum represent the perturbations to the Keplerian point-mass potential. In the equation above,

- $r_\odot$ is the distance of the Sun from the Mercury centre of mass (which was conveniently chosen as the centre of our reference frame),
- $\theta_\odot$ represents the colatitude of Mercury over which the Sun is located,
- $\phi_\odot$ represents the longitude of Mercury over which the Sun is located,
- $R_☿$ represents the equatorial radius of Mercury,
- the P_n^m are the associated Lagrange polynomials (unnormalized),
- and the C_{nm}, S_{nm} represent the coefficients of the gravitational potential in this spherical harmonics decomposition.

Each non-zero term represents a contribution to the deviation from the perfectly spherical shape of Mercury, and there exists a solar torque acting on the physical deformation it represents[6]. If we restrict ourselves to the first terms only, because they are the most important in magnitude and will thus bear the bulk of the torque interaction, we can express the hermeopotential through the

[6]While this is mostly true, it is impossible to discern between a homogeneous planet with deformations from the spherical form, and a perfectly spherical planet with a non homogeneous mass distribution. The spacecraft's orbital path is influenced through the mass distribution only, and not the physical shape of the planet. In reality both are linked through complex non linear relationships, different for each planet. To a first approximation, very large physical deformations cause very large mass redistributions.

following approximation:

$$V_{☿}\left(r,\theta,\phi)\right) = \frac{GM_{☿}}{r}\,[1 + C_{20}\left(\frac{R_{☿}}{r}\right)^2 P_2^0(\cos\theta)$$
$$+C_{22}\left(\frac{R_{☿}}{r}\right)^2 P_2^2(\cos\theta)\cos(2\phi)\Bigg] + O\left(\left(\frac{R_{☿}}{r}\right)^3\right), \tag{2.11}$$

where C_{20} and C_{22} represent the second degree gravitational field coefficients. The associated Legendre polynomials P_2^0 and P_2^2 have the following expression:

$$P_2^0 = \frac{3\cos^2\theta - 1}{2} \qquad P_2^2 = 3\sin^2\theta\,.$$

Expressing the torque in terms of the hermeopotential in a spherical coordinates basis we obtain:

$$\begin{aligned}\vec{M}_{☿\odot} &= \vec{r}_\odot \times \vec{\nabla}_\odot M_\odot V_{☿\odot}\left(r_\odot, \theta_\odot, \phi_\odot)\right)\\ &= r_\odot \vec{1}_{r_\odot} \times \left[\frac{\partial U_{☿\odot}}{\partial r_\odot}\vec{1}_{r_\odot} + \frac{1}{r_\odot}\frac{\partial U_{☿\odot}}{\partial\theta_\odot}\vec{1}_{\theta_\odot} + \frac{1}{r_\odot\sin\theta_\odot}\frac{\partial U_{☿\odot}}{\partial\phi_\odot}\vec{1}_{\phi_\odot}\right]\\ &= \frac{\partial U_{☿\odot}}{\partial\theta_\odot}\vec{1}_{\phi_\odot} - \frac{1}{\sin\theta_\odot}\frac{\partial U_{☿\odot}}{\partial\phi_\odot}\vec{1}_{\theta_\odot}\,,\end{aligned} \tag{2.12}$$

where $\vec{1}_{r_\odot}$, $\vec{1}_{\theta_\odot}$, $\vec{1}_{\phi_\odot}$ each represent a unit vector associated to the solar distance, colatitude and longitude respectively. Replacing eq. (2.11) in eq. (2.12) and calculating the derivatives we get:

$$\vec{M}_{☿\odot} = \frac{GM_{☿}M_\odot}{r_\odot}\,[$$
$$\left(\frac{R_{☿}}{r_\odot}\right)^2\left(\,3\cos\theta_\odot\sin\theta_\odot C_{20} + 6\cos\theta_\odot\sin\theta_\odot\cos 2\phi C_{22}\right)\vec{1}_{\phi_\odot}$$
$$+\frac{1}{\sin\theta_\odot}\left(-C_{22}\left(\frac{R_{☿}}{r_\odot}\right)^2 6\sin^2\theta_\odot\sin 2\phi_\odot\right)\vec{1}_{\theta_\odot}\Bigg] + O\left(\left(\frac{R_{☿}}{r}\right)^3\right). \tag{2.13}$$

If we further assume that $\theta_\odot = \frac{\pi}{2}$, i.e. that the Sun always lies in Mercury's equatorial plane [7], we can simplify the previous equation, and get:

$$\vec{M}_{☿\odot} = 6\frac{GM_{☿}M_\odot}{r_\odot}C_{22}\left(\frac{R_{☿}}{r_\odot}\right)^2\sin 2\phi_\odot\vec{1}_z + O\left(\left(\frac{R_{☿}}{r_\odot}\right)^3\right). \tag{2.14}$$

[7] This approximation can be seen as fixing Mercury's obliquity to zero. As we have seen earlier in this chapter due to Mercury being in Cassini state 1 the obliquity is very close to zero at around 2 arcmin.

$\vec{M}_{☿\odot}$ is parallel to $\vec{1}_z$ which represents the direction of the planetary spin axis. Any torque will thus speed up or slow down the planetary rotation giving rise to *Sun induced* librations, which we will identify the 88 day libration to be part of at the end of this section.

The only contribution from the hermeopotential in this case is coming from C_{22} which represents the equatorial asymmetry of Mercury. It is a measure of the ellipticity of Mercury's equator and can be expressed as follows in terms of the planetary main moment of inertia ($A < B < C$):

$$C_{22} = \frac{B - A}{4M_{☿}R_{☿}^2} \,, \tag{2.15}$$

where A is the smallest principal moment of inertia and is aligned with the equatorial short axis, B is aligned with the equatorial long axis, and C is along the planetary spin axis. This implies a choice of origin for $\phi_{\odot}$ that coincides with the planetary long axis. Replacing the above formulation of C_{22} in the previous equation (eq. (2.14)) we finally reach the expression of the torque exerted by the Sun on Mercury:

$$M_{☿\odot} = \frac{3}{2}\frac{GM_{\odot}}{r_{\odot}^3}(B - A)\sin 2\phi_{\odot} \,. \tag{2.16}$$

This expression is valid under the assumptions that we have *only* a point-like Sun in the equatorial plane of Mercury. The resulting torque will affect Mercury's spin and at the same time guarantees the stability of the 3:2 spin-orbit resonance.

2.3.2 Libration

Now that we have derived the expression for the solar torque affecting Mercury we can determine the period and amplitude of the librations caused by it. We replace the planetary subsolar longitude $\phi_{\odot}$ in eq. (2.16) with $\Psi_{\odot}$ the angle between Mercury's true equatorial long axis and the direction to the Sun in the following reasoning. This can be done because both are aligned in our hypothesis in which the planetary long axis points towards the Sun when the planet is at periherm, transforming eq. (2.16) into:

$$M_{☿\odot} = \frac{3}{2}\frac{GM_{\odot}}{r_{\odot}^3}(B - A)\sin 2\Psi_{\odot} \,. \tag{2.17}$$

From figure (2.1), the rotation angle of the planetary silicate shell in inertial space is

$$\Theta = f + \Psi, \tag{2.18}$$

where f is Mercury's true anomaly. The planetary rotation angle represents the uniform rotation of the planet with respect to its polar axis (Θ has a period of 58.646 days). The observed libration will be related to the surface displacement with respect to the uniform rotation. Why only the planetary surface? Because we do not have access to the eventual libration of deeper lying layers (i.e. the inner core) through surface displacement observations, such as those planned in the BepiColombo rotation experiment. Should Mercury possess an inner core and should it librate, this could be observed through gravitational perturbations on the MPO's trajectory if the signal is large enough. The presence of a librating inner core acts like a time varying mass distribution inside the planet in influencing the trajectory of the MPO.

If a liquid core is present it will interact with the silicate shell surrounding it and could either *follow* its movement entirely or partially or not at all. Assuming that the equatorial asymmetry (B-A) is entirely due to the mantle (spherically symmetric inner core) and that the core does not follow the libration of the mantle, the rate of change of the mantle's spin angular momentum L is given by the solar torque $M_{☿\odot}$:

$$\frac{dL}{dt} = C_m\ddot{\Theta} = M_{☿\odot} \; , \tag{2.19}$$

where C_m represents the main moment of inertia of the planetary mantle. Since Mercury's spin is in a 3:2 resonance with the orbital frequency, we introduce the libration angle as

$$\Gamma \equiv \Theta - \frac{3}{2}M \; , \tag{2.20}$$

where M is Mercury's mean anomaly. Inserting eq. (2.20) into eq. (2.19) yields:

$$C_m\ddot{\Theta} \equiv C_m\left(\ddot{\Gamma} + \frac{3}{2}\ddot{M}\right) \equiv C_m\ddot{\Gamma} = M_{☿\odot} \; , \tag{2.21}$$

as the planetary mean anomaly M advances at a constant rate and its second derivative is zero. We can therefore form the following differential equation involving the libration angle Γ:

$$\ddot{\Gamma} = -\frac{3GM_\odot}{2r_\odot^3}\left(\frac{B-A}{C_m}\right)\sin\left(2\Gamma - 2f + 3M\right) \; . \tag{2.22}$$

A more general set of differential equations including the coupling with the (different) libration of the core is discussed at depth by *Van Hoolst* (2007).

Note that the factor $r_\odot^{-3}$ in (2.22), which represents the distance between Mercury and the Sun, is time dependent due to the non-zero eccentricity of Mercury's orbit. The evolution of the true anomaly f is not constant through time as Mercury speeds up and slows down on its orbit around the Sun. The distance varies from 0.3AU at perihelion to 0.46AU at aphelion. We can replace $r_\odot$ with the constant semi-major axis a using the following definition of eccentricity functions $G_{lpq}(e)$ (*Kaula* 1966) through Hansen polynomials:

$$\left(\frac{r_\odot}{a}\right)^n \exp(imf) = \sum_{k=-\infty}^{\infty} X_{m+k}^{n,m}(e)\exp(i(m+k)M), \tag{2.23}$$

where $X_{m+k}^{n,m}(e)$ is a Hansen polynomial. The eccentricity functions are defined as:

$$G_{l,p,q}(e) = X_{l-2p+q+m}^{-(l+1),l-2p}(e) \,. \tag{2.24}$$

Replacing the expression above in 2.23 we get:

$$\begin{aligned}\left(\frac{r_\odot}{a}\right)^{-(l+1)} \exp(imf) &= \sum_{l-2p+k=-\infty}^{\infty} X_{l-2p+k+m}^{-(l+1),l-2p}(e)\exp(i(m+l-2p+k)M) \\ &= \sum_{q=-\infty}^{\infty} G_{l,p,q}(e)\exp(i(m+q)M) \,,\end{aligned} \tag{2.25}$$

as l and p are fixed values. In our case we consider the second degree gravitational field only, so $l \equiv 2$ and $m = l - 2p$. As the only gravitational coefficient present in the torque expression is C_{22} (see eq. (2.14)), we have $m \equiv 2$ implying that $p = 0$ so that 2.25 simplifies to:

$$\left(\frac{a}{r_\odot}\right)^3 \exp(2if) = \sum_{q=-\infty}^{\infty} G_{2,0,q}(e)\exp(i(2+q)M) \,. \tag{2.26}$$

Replacing the true anomaly using eq. (2.18) and eq. (2.20) we obtain:

$$\left(\frac{a}{r_\odot}\right)^3 \exp(-2i\Psi) = \sum_{q=-\infty}^{\infty} G_{2,0,q}(e)\exp(i(2+q)M - 2i(\Gamma + \frac{3}{2}M)) \,. \tag{2.27}$$

Keeping only the imaginary part, this equation simplifies to:

$$\left(\frac{a}{r_\odot}\right)^3 \sin(2\Psi) = \sum_{q=-\infty}^{\infty} G_{20q}(e)\sin\left[2\Gamma + (1-q)M\right] , \tag{2.28}$$

which can also be found in *Kaula* (1966) p. 35 .

This relation links the time dependent factor of the torque $r_\odot$ to an expansion in terms of the mean anomaly M. Looking at eq. (2.20) we can immediately see that by substituting eq. (2.28) into eq. (2.22) we can transform our differential equation into:

$$\ddot{\Gamma} = -\frac{3GM_\odot}{2a^3}\left(\frac{B-A}{C_m}\right)\sum_q G_{20q}(e)\sin\left[2\Gamma + (1-q)M\right]. \tag{2.29}$$

Using Kepler's 3rd we have

$$n^2 = \frac{GM_\odot}{a^3} \,,$$

l	p	q	$G_{lpq}(e)$
2	0	-1	$-\frac{e}{2}+\frac{e^3}{16}-\frac{5e^5}{384}+...$
2	0	0	$1-\frac{5e^2}{2}+\frac{13e^4}{16}-\frac{35e^6}{288}+...$
2	0	1	$\frac{7e}{2}-\frac{123e^3}{16}-\frac{489e^5}{128}+...$
2	0	2	$\frac{17e^2}{2}-\frac{115e^4}{6}+\frac{601e^6}{48}+...$
2	0	3	$\frac{845e^3}{48}-\frac{32525e^5}{768}+...$

Table 2.2: Values of the eccentricity function G_{lpq} needed for the Mercury libration expressions studied in this chapter.

and defining:

$$\alpha = \frac{3}{2}\frac{(B-A)}{C_m} , \tag{2.30}$$

we transform the equation 2.29 above to obtain:

$$\ddot{\Gamma} = -\alpha n^2 \sum_q G_{20q}(e)\sin\left[2\Gamma + (1-q)M\right] . \tag{2.31}$$

We know that the mean anomaly is $M = nt$ up to a constant and by substituting the derivatives with respect to time by derivatives with respect to M eq. (2.31) transforms to:

$$\begin{aligned} n^2\frac{d^2\Gamma}{d^2M} &= -\alpha n^2 \sum_q G_{20q}(e)\sin\left[2\Gamma + (1-q)M\right] \\ \frac{d^2\Gamma}{d^2M} &= -\alpha \sum_q G_{20q}(e)\sin\left[2\Gamma + (1-q)M\right] . \end{aligned} \tag{2.32}$$

This last equation is the expression we will use to derive the libration amplitudes of the most important Sun-induced librations. By developing the sine terms, we have:

$$\begin{aligned} \frac{d^2\Gamma}{d^2M} = -\alpha \sum_q G_{20q}(e)\,[&\cos(2\Gamma)\sin(M(1-q)) \\ &+2\cos(\Gamma)\sin(\Gamma)\cos(M(1-q))] . \end{aligned} \tag{2.33}$$

This differential equation represents the periodic variations of Mercury's rotational movement as a function of the orbital eccentricity e , the equatorial asymmetry $B-A$ and the mantle moment of inertia C_m (see 2.30).

2.3.3 Free Libration

The free libration in longitude results when the axis of minimum moment of inertia does not point toward the Sun when Mercury is at perihelion. The solar torque on the permanent equatorial asymmetry of the planet, averaged around the orbit, tends to restore the alignment of the axis of minimum moment of inertia with the Sun at perihelion. So viewed at perihelion, the long axis will tend to librate about the direction toward the Sun. The period of this movement is the free libration period, which we want to determine.

In order to obtain long period terms (from which M is absent) we can average (2.32) with respect to M, meaning that we can integrate with respect to M over a whole revolution (from 0 to 2π) and then divide by 2π. Only if $q \equiv 1$ do we have terms from which M is absent. Since torques are small Ψ does not change much over an orbital period, and $\dot{\Psi}$ as well as $\dot{\Gamma}$ can be considered constant over one orbital period. The angle Γ is considered very small, and time-dependent forcing terms proportional to $\sin 2\Gamma$ can be neglected in the right hand side of equation (2.33). The periodic forcing terms in the right hand member of eq. (2.33) vanish, reducing the equation to the harmonic oscillator equation:

$$\begin{aligned}\frac{d^2\Gamma}{d^2M} &= -2\alpha G_{201}(e)\cos(\Gamma)\sin(\Gamma)\\ &\cong -2\alpha G_{201}(e)\Gamma\,. \end{aligned} \tag{2.34}$$

The resulting expression from eq. (2.34) yields the period of the long-term libration (or free libration) as being equal to:

$$\Pi_{\mathrm{FreeLibration}} = (2\alpha G_{201})^{1/2}\,, \tag{2.35}$$

in Mercury revolutions. For a value of α of 2×10^{-4} (based on the values obtained by Mariner 10 (*Anderson et al.* 1987)) and G_{201} as given in table (2.2) this long-term period is $\sim$ 50.5 revolutions, i.e. $\sim$ 12 years. Due to different dissipation processes inside the planet this libration should have damped out and no observable amplitude should have remained, since *Peale* (2005) has shown that the damping time is $< 10^5$ years for all types of known excitations. This reasoning is valid except if a hitherto unknown process excites this libration.

The free period of $\sim$ 12y is very close to one of Jupiter's periodic forcings on Mercury at 11.86y (Jupiter's orbital period). Amplification of the 11.86y Jupiter induced libration amplitude due to its proximity to the $\sim$ 12 year free libration period will be important (*Dufey et al.* 2008; *Peale et al.* 2009) and helps to explain why this specific Jupiter induced libration *may* exhibit the most important amplitude of all planetary librations.

The independent measurement / determination of its amplitude will pose an additional constraint on $\frac{B-A}{C_m}$ because both the annual libration and the planetary induced librations depend on it in the same way (providing an additional opportunity to study Mercury's interior.)

2.3.4 Annual Libration

What remains to be determined is the amplitude Θ_0 of the 88-day libration which is the main quantity of interest in this work. In order to obtain terms with an 88-day period we need to keep only those proportional to $\cos M$ or $\sin M$. This condition imposes that $q = 0$ or $q = 2$ in eq. (2.33) yielding :

$$
\begin{aligned}
\frac{d^2\Gamma}{d^2M} =& -\alpha G_{200}(e)\Big[\cos(2\Gamma)\sin M + \sin(2\Gamma)\cos M\Big] \\
& -\alpha G_{202}(e)\Big[-\cos(2\Gamma)\sin M + \sin(2\Gamma)\cos M\Big] \\
\frac{d^2\Gamma}{d^2M} =& -\alpha\,(G_{200}(e) - G_{202}(e))\cos(2\Gamma)\sin M \\
& -\alpha\,(G_{200}(e) + G_{202}(e))\sin(2\Gamma)\cos M \ . \qquad (2.36)
\end{aligned}
$$

Since Γ is small we can neglect terms in $\sin 2\Gamma$ and pose $\cos 2\Gamma \cong 1$:

$$
\frac{d^2\Gamma}{d^2M} \cong -\alpha\,(G_{200}(e) - G_{202}(e))\sin M\,, \tag{2.37}
$$

so that the expression for the annual libration amplitude is:

$$
\Theta_0 = \alpha\,(G_{200} - G_{202}) \ . \tag{2.38}
$$

If $\alpha = 2 \times 10^{-4}$ (a value close to the one used by *Margot et al.* (2007b))[8] as for the free libration, then $\Theta_0 \approx 35$ arcsec. This value is in perfect agreement with the experimental value $\Theta_0 = 35.8 \pm 2$arcsec of *Margot et al.* (2007b).

There are also higher-frequency terms which need to be included to describe Mercury's libration more precisely, as can be seen from the previous reasoning. To accurately model the libration we have to take into account the semi-annual contribution Θ_1 which can be obtained if we keep only those terms in $\cos 2M$ or $\sin 2M$. Using the same reasoning as for the annual amplitude but keeping only $q = -1$ and $q = 3$ in eq. (2.33) yields:

$$
\Theta_1 = \frac{\alpha}{4}\,(G_{20-1} - G_{203}) \ , \tag{2.39}
$$

which (under the same hypothesises as before) gives $\Theta_1 \approx 3.7$ arcsec. Calculating the value of Θ_2 using the same reasoning yields an amplitude < 1as which is lower than the expected experimental accuracy of the BepiColombo libration determination experiment. We can limit ourselves to Θ_1, neglecting higher harmonics, for this reason.

[8]New values computed with data from MESSENGER flyby's in 2008/09 were not available at the time of writing. It is currently expected that new values will be available shortly after MESSENGER enters into orbit around Mercury in the spring of 2011.

We finally obtain the following approximation which we will later use as our Mercury libration model:

$$\gamma(t) = \Theta_0 \sin M(t) + \Theta_1 \sin 2M(t)\,. \tag{2.40}$$

Incidentally the appearance of the semi-annual libration amplitude does not add an unknown to our system, as the amplitudes of the higher harmonics of the annual libration are related through a fixed coefficient to the annual libration amplitude. These coefficients, which we call K only depend on the eccentricity of Mercury's orbit through the eccentricity functions. In the case of the semi-annual (44-day) libration we have that:

$$K = \frac{\Theta_1}{\Theta_0} = \frac{\frac{\alpha}{4}(G_{20-1} - G_{203})}{\alpha(G_{200} - G_{202})} = \frac{G_{20-1} - G_{203}}{4(G_{200} - G_{202})}\,, \tag{2.41}$$

where the eccentricity function $G_{l,p,q}(e)$ only depends on the eccentricity of the planetary orbit.

The current eccentricity value for Mercury is $e = 0.20563069$ and leads to a value of $K = -0.105455$. The eccentricity of Mercury's orbit varies very slowly with time so that from the year 1800 up to the year 2200 a rising trend due to a long period variation increases it from $e = 0.205597$ to $e = 0.205684$, for a difference of 1.10^{-4}. On a shorter timescale of 20 years between the year 2000 and 2020 the difference in eccentricity is even smaller 4.10^{-5}. If we take the associated K values corresponding to these extremes the change in relative amplitude of the semi-annual libration will be:

$$K(e_{min}) - K(e_{max}) = (-0.105396) - (-0.105548) = 1.5210^{-4} \approx 0.14\%K\,. \tag{2.42}$$

Unless we have a very precise measurement of Mercury's annual libration we won't be able to make a difference between these extreme situations. The precision goal for the BepiColombo libration experiment is to achieve less than 3 arcseconds error on the annual libration amplitude (*Milani et al.* 2001), which is about two order of magnitudes over the signature of a small eccentricity error. If we were to adjust both annual and semi-annual libration amplitudes independently, this would amount to adjust the K factor, which in turn amounts to a new estimate of Mercury's orbital eccentricity! As this quantity is very well know relative to the other parameters in our system, we can fix the value of K once and for any eccentricity value of the 21st century, being confident that the small resulting imprecision in K will be of no consequence on the rotation experiment.

2.3.5 Planetary induced librations

The same torque mechanism as previously explained for the Sun-Mercury torque interaction can be used to determine libration frequencies and amplitudes caused through *planet*-Mercury interactions. This tedious task is beyond the scope of our work and has been done in detail analytically as well as numerically by *Dufey et al.* (2009) and *Peale et al.* (2009). Their results will be used throughout this work. The mechanisms behind planetary induced librations can be explained very easily. Planetary interactions with Mercury will perturb Mercury's orbital movement, creating irregularities in it. If Mercury's position is shifted with respect to its unperturbed orbital motion, the solar torque acting on Mercury will be modified too. This can be modelised as a superposition of long period variations at the frequency of the perturbation on top of Mercury's *unperturbed* 88-day *solar-librational* cycle. When Mercury is close to its present final state, the timescales for damping the free libration and to approach Cassini state 1 are both of the order of 10^5 years (*Peale* 2005). Since this time is short compared to the age of the Solar System, we would expect to find Mercury in the equilibrium Cassini state 1 with completely damped free libration in longitude, only observing an annual libration except if some resonance with planetary perturbations exist. In that case only the amplifying effect of the free libration could be observed on the observed amplitudes of the long period planetary induced librations. For perturbations with periods close to the free libration period the amplification would be the most significant.

Body	Period	Forcing argument	Normalized	Amplitudes
			Peale et al. (2009)	*Dufey et al.* (2009)
Sun	43.98466 d	$2(\lambda - \omega)$	0.10223	0.11150
Sun	87.96935 d	$\lambda - \omega$	1.00000	1.00000
Venus	5.66316 y	$2\lambda - 5\lambda_V + 3\omega$	0.09697	0.10691
Jupiter	11.86295 y	$\lambda_J - \omega$	1.09339	1.2193

Table 2.3: A summary of the main libration amplitudes and associated periods, normalized relative to the annual libration amplitude.

2.4 The Peale Procedure

A major goal of the BepiColombo mission to Mercury is the determination of the structure and state of Mercury's interior. The probing of interior properties is based on the precise determination of the four following parameters:

- Mercury's obliquity η,
- Θ_0 the amplitude of the annual libration in longitude,
- and the second degree harmonic coefficients in the expansion of Mercury's gravitational field C_{20} and C_{22}.

As shown by i.e. *Peale* (1976) these parameters are sufficient for determining the factors in the following equation, which establishes a link with the planetary interior if Mercury is in the Cassini state 1:

$$\left(\frac{C_m}{B-A}\right)\left(\frac{B-A}{M_☿ R_☿^2}\right)\left(\frac{M_☿ R_☿^2}{C}\right) = \frac{C_m}{C} \leq 1\,, \tag{2.43}$$

where $M_☿$ and $R_☿$ are the mass and radius of Mercury. The first factor follows from the amplitude of the annual libration given by eq. (2.38) and only depends on the eccentricity e and the value of α. The second factor follows from the definition of the low degree gravity field coefficient as a function of the moment of inertia given in eq. (2.15), and the third from the Cassini state 1 equilibrium equation given previously in eq. (2.1) by *Peale* (1969):

$$\left(\frac{C}{M_☿ R_☿^2}\right) = \frac{\left[\frac{J_2}{(1-e^2)^{3/2}} + 2C_{22}\left(\frac{7}{2}e - \frac{123}{16}e^3\right)\right]}{\frac{\sin I}{\eta_c} - \cos I}\frac{n}{\rho}, \tag{2.44}$$

where η_c is the obliquity of Cassini state 1. Eq. (2.44) shows the dependence of $C/M_☿ R_☿^2$ on J_2, C_{22}, and η_c and together the last three equations show that we need to know I, e, η_c, Θ_0, J_2 and C_{22} to determine C_m/C, the ratio of the mantle to the polar moment of inertia. Both BepiColombo and MESSENGER are expected to measure the degree-two gravity coefficients with an accuracy better than 1% and the obliquity and forced libration amplitude better than a few arcseconds (*Solomon et al.* 2001; *Milani et al.* 2001). The realistic estimation of attainable accuracy of both obliquity and libration amplitude determination in the frame of the BepiColombo mission is the main focus of this work. Previous simulations by *Milani et al.* (2001) and *Jehn et al.* (2004) have neglected important mission constraints and only used very basic error statistics.

Since it is assumed in the derivation of the libration equations that the librations are with respect to the equilibrium state in which the core co-precesses with the mantle, the liquid core is tacitly assumed to follow the mantle during the long period precession movement (280ky). This experiment can only be successful if the following conditions are met (*Peale* 1988):

1. The liquid core *must not* follow the mantle during the 88 day forced libration in longitude. If this were to be the case, the whole planet would participate in the libration movement and no differentiation between the liquid core and solid core case could be done.

2. The core *must* follow the mantle during the 280,000 year orbit precession, where the spin axis is locked to this precession if it occupies the Cassini state. If this were not to be the case C_m would appear instead of C in eq. (2.44), thus rendering eq. (2.43) equal to 1 for all values of C_m and the experiment impossible. Since it is assumed in the derivation of the libration equation that the librations are with respect to the equilibrium state in which the core co-rotates with the mantle, the liquid core is tacitly assumed to follow the mantle during the long period precession

movement. Viscous core-mantle coupling is sufficiently large for this condition to be satisfied (*Peale* 1988).

3. Mercury's equatorial bulge must not be significantly influenced by core-mantle boundary pressure couplings due to a non axially symmetric liquid core. To a first approximation it must be due to the mantle only.

4. Mercury is assumed to occupy Cassini state 1 to determine C_m/C through this procedure. Eq. (2.1) shows that the moment of inertia C is approximately inversely proportional to the Cassini state obliquity η_C. The obliquity measurements by *Margot et al.* (2007b) yield a value of 2.11 ± 0.1arcmin, which is very close to $\eta_C = 1.6$arcmin the *theoretical* value (as shown earlier in this chapter). This guarantees that Mercury is very close to Cassini state 1 at the present time.

For a correct interpretation of the libration observations all possible perturbations of Mercury's rotation have to be quantified. These include core-mantle couplings (neglected in our expression of the libration), which have been shown to be very important for Earth[9], but as no general agreement on the underlying dominant physical mechanisms exists, nothing can be said about these for Mercury. Electromagnetic coupling has been shown not to affect the forced librations by *Peale et al.* (2002), under the condition that Mariner 10 values for the magnetic dipole moment is close to the real world value. In the case of a thin shell dynamo inside Mercury, *Stanley et al.* (2005) have shown that they can produce very strong fields inside the core with significantly different geometries than Earth's field and with Mercury-like dipolar field intensities.

In the approach to derive eq. (2.40), it is implicitly considered that the liquid core is symmetric ($A^f = B^f$) because no inertial core-mantle coupling is considered. If in reality the core is not axially symmetric, it will be very weakly coupled to the mantle. *Peale et al.* (2002) have shown that, even for large solid inner cores and large inner core flattening, the amplitude of the 88 day mantle libration is nearly unchanged by gravitational couplings. Pressure couplings have been shown to be of equally small importance to the annual libration amplitude by *Rambaux et al.* (2007) staying below 0.01arcsecond even for a large core-mantle boundary flattening up to 10^{-3}. This ensures that the third condition is respected as well.

The first two conditions are satisfied for topographical coupling due to core-mantle boundary (CMB) irregularities, viscous core-mantle coupling, magnetic core mantle coupling, and gravitational coupling between an axially asymmetric solid inner core and the mantle (*Peale et al.* 2002)

A value of C_m/C equal to one would be an indication of a core closely coupled to the mantle, and thus solid. If part of the core is fluid (independently of the presence of a solid inner core) the C_m/C ratio will be close to 0.5 in the case of a core radius of the order of ($r_{core} \simeq 0.75 R_{☿}$) as we expect from current models

[9]This has been attributed to the exchange of angular momentum between the liquid core and solid mantle (*Jault et al.* 1988) .

of Mercury's interior (*Van Hoolst et al.* 2007; *Rivoldini et al.* 2009). Such a core size is relatively larger than for the three other terrestrial planets.

The preceding explanation of the Peale procedure justifies our drive to determine Mercury's libration, because it will enable us to obtain information on the internal structure of the planet.

Chapter 3

Planetary rotation and spacecraft orbit model

Contents

This chapter is entirely dedicated to the modelling aspect of our work. We will discuss our choice of modelisation for Mercury's rotation and for Bepi-Colombo's MPO orbit around the planet. The simulation approach will be explained in the second part. The goal is to justify our choices in approximations of the systems considered. For our simulation purposes some effects can be completely neglected or their expression heavily simplified but others have to be taken into account very precisely.

3.1 Reference frames

We use several reference frames throughout this work :

1. Mercury body-fixed reference frame based on the IAU2000 constants. This frame is fixed to and does not move with respect to *surface* features

of the planet, but it does move with respect to inertial frames as Mercury rotates. The orientation of this frame is determined from the IAU model for the body defined by *Seidelmann et al.* (2002). This frame is centred on the planet's centre of mass, has its z-axis in the direction of the planet's spin axis, and its x-axis aligned to pass through the prime meridian of the planet with the remaining y-axis complementing the right-handed frame. Mercury's prime meridian is defined relative to the position of the Hun Kal crater which is fixed at a longitude of 20°.

2. The Hermean Mean Equator (HME) is a frame attached to Mercury's equator at J2000. It can be summarized as a non rotating version of the body-fixed frame, with a special orientation of the x-axis along the prime meridian of the planet at the freezing epoch of J2000.

3. The Hermean Mean Ecliptic of J2000 (HME2000) We will use this frame as our reference frame of choice when performing our simulations. Its z-axis is defined as the normal to the orbital plane. Its x-axis is defined as the direction pointing towards the vernal point of Mercury at the J2000 epoch. This frame is separated from the Hermean Mean Equator through a (3-1-3) Euler axis rotation. The angle between the z-axis of the Mean Equator frame and Mean Ecliptic frame represent the planet's obliquity.

4. ICRF2000 inertial frame based on the Earth Mean Equator of J2000 and the mean equinox of J2000. Planetary coordinate systems are defined relative to their mean axis of rotation and various definitions of longitude depending on the body. The longitude systems of most of those bodies with observable rigid surfaces have been defined by references to a surface feature such as a crater. Approximate expressions for these rotational elements with respect to the J2000 inertial coordinate system have been derived. The International Celestial Reference Frame (ICRF) (*Ma et al.* 1998) is the reference coordinate frame of epoch 2000 which is 12 o'clock January 1st 2000 (JD 2451545.0).

5. Topographic frames are used in conjunction with the associated body-fixed frame to express quantities as *seen* by a surface point. The z-axis corresponds to the local zenith and the x-axis points to the local north, while the y-axis completes the right handed frame (pointing eastward). This is extremely useful when trying to establish if an Earth based ground station is able to *see* the spacecraft or not or to determine the separation angle between the Sun and Mercury. We also use a similar reasoning when determining the Mercury surface illumination conditions, for a specific target.

3.2 Mercury orientation model

To be able to reconstruct the rotation of the planet Mercury in order to estimate the libration amplitude in a later stage we must first create a model of this rotation and the planet's spatial orientation with respect to an inertial frame.

3.2.1 Rotation

The rotation period of the planet Mercury corresponds to exactly two thirds of its revolution period : 58.6461 days. Its properties have been extensively discussed in chapter 2. Had Mercury's orbit been circular and the planet perfectly spherical, the 3:2 spin orbit resonance would not have been stable and the science community would not have this opportunity of insight into the planetary interior through the libration determination. Additionally we consider the main planetary perturbations on Mercury's revolution and their effects on its rotation. The mechanism and main perturbations are described in section 2.3 and in table (2.3). We limit the planetary perturbations to those periods creating/inducing the largest libration amplitudes (amplitudes above the expected experimental threshold of 1-3 arcsec). The main Venus induced libration has an amplitude which is comparable to the semi-annual libration amplitude, while the main Jupiter induced libration is expected to have an amplitude of the order of the annual libration amplitude (depending on the proximity with the free libration period). Libration frequencies with smaller amplitudes should remain unresolved by the BepiColombo rotation experiment which has requirements to attain a 1 to 3 arcsecond precision on the annual libration amplitude, as their amplitudes are below the arcsecond level.

Annual libration

The forced libration has been shown to be a periodic motion with an annual period in section 2.3. To be more precise it is actually a combination of a movement with an annual period and a harmonic series of lesser amplitudes (with periods 2^{-n} multiples of the original one as seen in eq.(2.40). We adopt the following form for the annual libration as part of our Mercury rotation model:

$$\begin{aligned} \Gamma &= \gamma_0 \sin\lambda_0 + \gamma_1 \sin 2\lambda_0 \\ &= \gamma_0 (\sin\lambda_0 + K \sin 2\lambda_0) \ , \end{aligned} \tag{3.1}$$

with λ_0 the Mercury mean anomaly and γ_0 and γ_1 the amplitude of the annual and semi-annual libration respectively.

Recent Earth based radar measurements of Mercury *Margot et al.* (2007b) have shown a value of 35.8 ± 2 arcsec for the annual libration amplitude indicating the probable presence of a liquid/molten core. We will use this value in our simulations.

Jupiter induced libration

The main libration caused by Jupiter has a period of 11.86y corresponding to Jupiter's orbital period. This libration is heavily amplified by the close presence of Mercury's free libration which is currently estimated to be very close to a period of 12 years (see *Peale et al.* (2009), *Dufey et al.* (2009) and section 2.3.3). A small error on the free libration frequency results in a very large change in the 11.86 years Jupiter induced libration amplitude because of this proximity. Therefore the amplitude of this libration is extremely responsive to a small change in the parameters of Mercury's interior models, and because of this expected amplitudes range from 32% of the annual amplitude up to 120% or more. Both *Peale et al.* (2009) and *Dufey et al.* (2009) using the latest parameter values tend to predict a Jupiter libration amplitude around 100% of the annual libration amplitude.[1]. In our simulations we use a value of 42 arcsec for this amplitude. The form of this libration is given by:

$$\Gamma_{♃} = \gamma_{♃} \sin(\lambda_{♃} - \bar{\omega}), \tag{3.2}$$

where $\lambda_{♃}$ is Jupiter's solar longitude and $\bar{\omega} = \omega + \Omega$ the longitude of perihelion composed of ω the argument of perihelion and Ω the longitude of the ascending node of the orbit plane on the ecliptic. As can be seen the phase of this libration is constrained by the relative solar longitudes of Mercury's perihelion and Jupiter. Only the amplitude $\gamma_{♃}$ is unknown. As we have shown in Chapter 2 there exists a relationship between all planetary induced libration amplitudes and the annual libration amplitude which depends on the value of α via the free libration frequency. Therefore the Jupiter induced libration amplitude can be used as a measure of the moment of inertia ratio.

Venus induced libration

The main libration caused by Venus is of the form:

$$\Gamma_{♀} = \gamma_{♀} \sin(2\lambda_{☿} - 5\lambda_{♀} + 3\bar{\omega}), \tag{3.3}$$

with $\lambda_{♀}$ Venus' solar longitude and $\lambda_{☿}$ Mercury's solar longitude and $\bar{\omega}$ as previously. As for all other planetary perturbations the phase is fixed by the relative position of the bodies with respect to each other and the repetitiveness of the pattern gives the period. This particular Venus induced libration is the most important planetary perturbation if all amplification effects are ignored. Because of its 5.66 years period which is farther away from the free period of 12 years than the 11.86years Jupiter libration, it is only weakly amplified. To a first approximation its amplitude is therefore only marginally affected by the error on the free libration frequency.

[1]When using the current values for Mercury's C/MR^2, C_{20} and C_{22} (*Anderson et al.* 1987)

Complete Mercury rotation model

If we define θ as the uniform rotation rate of the planet and θ_0 the initial angle of the prime meridian at time $t_0 = J2000.0$ the complete model of Mercury's rotation is then:

$$\begin{aligned}\Theta(t) &= \theta_0 + \theta t + \Gamma(t) + \Gamma_{♃}(t) + \Gamma_{♀}(t) \\ &= \theta_0 + \theta t + \gamma_0 (\sin \lambda_0 + K \sin 2\lambda_0) \\ &+ \gamma_{♃} \sin(\lambda_{♃} - \bar{\omega}) + \gamma_{♀} \sin(2\lambda_0 - 5\lambda_{♀} + 3\bar{\omega})\,. \end{aligned} \tag{3.4}$$

Θ as defined above is expressed in Mercury's non-rotating equatorial frame (HME2000). To represent the motion of a point on the planetary surface in an inertial frame centred on Mercury we place the frame in Mercury's orbital plane through a rotation of an angle η about x^*, an axis in the equatorial (xy) plane of the planet. The axis x^* corresponds to the x axis of the Hermean Mean Ecliptic Frame. This angle η represents the planet's obliquity.

3.2.2 Mercury's obliquity

The radar observations of Mercury's rotation by *Margot et al.* (2007b) also yielded information about the orientation of the planet's spin axis and thus on its obliquity. In the following we have adopted their estimated value of η = 2.11arcmin in our simulations.

a	e	i	Ω	$\bar{\omega}$
0.387098 AU	0.205632	7.004986°	48.3309°	77.4561°

Table 3.1: Orbital elements of Mercury at epoch J2000. $\bar{\omega}$ is the longitude of perihelion: $\Omega + \omega$.

3.3 Libration determination method

In the following paragraphs we lay out the BepiColombo libration determination experiment working method.

Broadly stated, the BepiColombo Mercury Planetary Orbiter (MPO) will take repeated pictures of specific *targets* on the planetary surface whenever it flies over them. By comparing the position in inertial space of points on Mercury's surface at specified epochs it is possible to visualise their movement in space through time, which contains information on the planetary libration and obliquity. To achieve this the BepiColombo science team will have to identify several easily spotted and convenient targets on the planetary surface which will have to be observed repeatedly over the mission lifetime. Such targets could be very bright albedo spots or craters with well defined borders of a sufficient size, enabling an easy distinction of them from their surroundings. In the rest of this document those *targets* will be alternatively called *spots*, *targets* or *points*. One of the aims of this study is to determine how many such targets are needed to achieve the required precision on libration and obliquity and subsequently on interior parameters of Mercury (see chapter 2). Additionally our study also aims at determining what regions of the planetary surface are better suited to contain these targets.

To get a feeling for the observability of the libration of Mercury, we have evaluated the surface displacement by using the following relation: a libration amplitude of 10arcsec causes a landmark at the equator of Mercury ($R_{☿} \simeq 2440$km) to drift regularly to the East and to the West up to 118 m with respect to its *nominal* position (where nominal refers to a Mercury with a constant spin rate). Our choice of $\Phi_0 = 35.8$ arcsec creates an annual libration movement of ± 400m at the equator. This is to be compared with the pixel size of the BepiColombo High Resolution Imaging Camera (HRIC), which oscillates between 5 and 19 meters depending on the MPO altitude.

When one of the targets is inside the field of view (FOV) of the HRIC a photograph will be taken. Around the same time the star-tracker will have to determine the orientation of the spacecraft with respect to the stars and thus in inertial space, so as to establish a precise link between the planetary surface and an inertial reference frame. The spacecraft's orbit is determined through Earth-based Doppler tracking and ranging through either the NASA DSN (Deep Space Network) stations or the ESA ESTRACK stations. A range measurement is a precise measurement of the distance separating the Earth-based tracking station and the satellite, contrary to Doppler measurements which are high precision range-rate / velocity measurements of the spacecraft movement relative to the Earth based tracking station. Both types of measurement are needed to provide an accurate reconstructed spacecraft orbit. This technique has been successfully used for the last 40 years in order to precisely determine the orbits of space probes and information on the trajectory perturbations they are subjected to. A probe like the BepiColombo MPO in orbit around Mercury will be subject to many orbital perturbations due to the fact that the planet cannot be reduced to a point-mass. Through precise orbit determination it is possible to retrieve information on the planetary gravitational field the spacecraft evolves in. In section 3.6 the theory of spacecraft orbits around planetary bodies will be explained in detail. The precise position of each image (and thus the target) from the planetary surface can thus be reconstructed in an inertial frame (i.e. HME2000) through the information of *where* the spacecraft was and what direction it was oriented in at the time the picture was taken.

3.4 Construction of our observable

Here we define the way we construct our observable, translating the libration determination method into equations. We also determine the partial derivatives and construct the normal matrix needed in the least-squares approach used to estimate the rotation and orientation parameters.

We need to express the position of any given point on the planetary surface in an inertial frame in order to perform the simulation of this experiment, as each image that will be delivered from the spacecraft will not be positioned with respect to the planetary surface but inertial space. A point on the planetary surface can be expressed in the Mercury body-fixed frame as,

$$\begin{pmatrix} r \\ \phi \\ \lambda \end{pmatrix} \tag{3.5}$$

in spherical coordinates, where r is the planetary radius, ϕ is the latitude and λ is the longitude of the surface point. In this reasoning we approximate Mercury's shape to be spherical, which is good enough for the purpose of this study. We will identify all targets on the planetary surface as well as images taken by the MPO camera in these coordinates. Transforming the spherical coordinate expression in Cartesian coordinates we get:

$$\begin{pmatrix} x \\ y \\ z \end{pmatrix} = \begin{pmatrix} r\cos\phi\cos\lambda \\ r\cos\phi\sin\lambda \\ r\sin\phi \end{pmatrix}, \tag{3.6}$$

where $\vec{z}$ coincides with the spin axis of Mercury, $\vec{x}$ passes through the prime meridian and $\vec{y}$ completes the right handed frame. If we want to express this fixed point in the inertial Hermean Mean Ecliptic frame we need to perform a series of rotations. First a rotation from the fixed frame to the Mercury non-rotating frame is performed. The latter frame differs from the first through the fact that its x and y axes are not fixed to the planetary surface any more. This involves a rotation with respect to the z-axis to subtract the planetary rotation, yielding:

$$\begin{pmatrix} x \\ y \\ z \end{pmatrix}_{nonrot} = R_3(-\Theta)\begin{pmatrix} x \\ y \\ z \end{pmatrix}_{fixed}, \tag{3.7}$$

where R_3 represents the rotation matrix with respect to the z-axis, and Θ is the planetary rotation model defined in eq.(3.4). The target position does now depend on Mercury's rotation (rate), and through this also on its librations. We then apply a series of rotations in order to express this position in the Hermean Mean Ecliptic frame. This transition from an equator-based reference frame to an orbital-plane-based reference frame is performed through the application of 3 rotations with respect to the axes 3-1-3, in order to correct for the planetary obliquity η:

$$\begin{pmatrix} x \\ y \\ z \end{pmatrix}_{inertial} = R_3\left(\varphi_\eta\right) R_1\left(-\eta\right) R_3\left(-\varphi_\eta\right) \begin{pmatrix} x \\ y \\ z \end{pmatrix}_{nonrot} \tag{3.8}$$

$$= R_3\left(\varphi_\eta\right) R_1\left(-\eta\right) R_3\left(-\varphi_\eta\right) R_3(-\Theta) \begin{pmatrix} x \\ y \\ z \end{pmatrix}_{fixed} , \tag{3.9}$$

where φ_η represents the planetary longitude of Mercury's vernal point (intersection between Mercury's equatorial plane and Mercury's ecliptic plane) at the observation epoch. From this equation we can see that the expression of a point on Mercury's surface in the Hermean Mean Ecliptic frame depends on the planetary rotation and obliquity, which are our main parameters of interest. In the course of the future real experiment this information will arrive packaged in the form of spacecraft position and orientation data attached to each image, giving only the position of the image taken in inertial space.

In our simulation images are identified through their centre point expressed in the Mean Ecliptic frame. This makes the process of *generating* image pairs quite simple in that it only involves subtracting two different positions:

$$\Delta \begin{pmatrix} x \\ y \\ z \end{pmatrix} = \begin{pmatrix} x \\ y \\ z \end{pmatrix}_{t_1} - \begin{pmatrix} x \\ y \\ z \end{pmatrix}_{t_2} , \tag{3.10}$$

where the indices t_1 and t_2 correspond to the epochs of each image to be compared. Combining equations 3.7 with 3.10 we obtain:

$$\vec{\Delta x}_{t_1 t_2} = R_3\left(\varphi_\eta\right) R_1\left(-\eta\right) R_3\left(-\varphi_\eta\right) \left[R_3\left(-\Theta(t_1)\right) \vec{x}_{t_1} - R_3\left(-\Theta(t_2)\right) \vec{x}_{t_2}\right] . \tag{3.11}$$

This expression represents the observable quantity in our simulations. To correctly simulate the restitution of our parameters from these simulated observables we still need to apply observational errors on each measure (as described in section 3.7) in function of the observation epoch (Earth observability, spacecraft altitude, ...). This is included in the fact that we do not consider $\vec{x}_{t_1}$ to be equal to $\vec{x}_{t_2}$, as different errors apply at each epoch. Another crucial element missing is the knowledge of what part of the surface can be seen through the high resolution camera at any time, so as to build a database of potential image matching candidates. This will be the object of the following sections of this chapter.

3.5 Least Squares approach

The goal of any least squares analysis is to solve the following system:

$$\mathbf{A}p = b, \tag{3.12}$$

where $\mathbf{A}$ is a $(m \times n)$ matrix (with n the number of parameters and m the number of observations), b is a $(m \times 1)$ vector containing the residuals of the observations, and p $(n \times 1)$ is the common value taken by the parameters throughout all observations which is to be determined by our least squares approach.

$\mathbf{A}$ is usually not a square matrix and as such no inverse can be calculated. To solve this problem, we have to rewrite the previous equation the following way:

$$(\mathbf{A}^T \mathbf{C}_b^{-1} \mathbf{A})p = \mathbf{A}^T \mathbf{C}_b^{-1} b, \tag{3.13}$$

where $\mathbf{A}^T$ is the transpose of $\mathbf{A}$ and $\mathbf{C}_b$ is a $(m \times m)$ weight matrix applied to the observations. Generally a diagonal matrix composed of the inverse a priori uncertainties on the observations (b) is used. In our case $\mathbf{C}_b$ is equal to the identity matrix as we do not give more weight to certain observations relative to others.

$\mathbf{A}^T \mathbf{C}_b^{-1} \mathbf{A}$ is thus a square $(n \times n)$ matrix, and is called the normal matrix. In our particular case, $\mathbf{A}$ is the matrix of partial derivatives of our observable with respect to the different parameters:

$$\mathbf{A}_{il} = \frac{\partial \Delta \vec{x}_i}{\partial p_l}, \qquad for \quad i = 1..3 \quad \text{and} \quad l = \eta, \gamma_0, \gamma_{♃}, \gamma_{♀}, \tag{3.14}$$

where l represents the four parameters we study.

The partial derivatives of our observable with respect to our parameters of interest have the following form:

$$\frac{\partial}{\partial \eta} \Delta \vec{x}_{t_1\, t_2} = R_3\left(\varphi_\eta\right)(-1)\frac{\partial R_1(-\eta)}{\partial \eta} R_3\left(-\varphi_\eta\right)\left[R_3\left(-\Theta(t_1)\right)\vec{x}_{t_1} - R_3\left(-\Theta(t_2)\right)\vec{x}_{t_2}\right], \tag{3.15}$$

for the derivative with respect to the obliquity η,

$$\begin{aligned}\frac{\partial}{\partial \gamma_0} \Delta \vec{x}_{t_1\, t_2} = R_3\left(\varphi_\eta\right) R_1(-\eta) R_3\left(-\varphi_\eta\right) \Bigg\{ & \frac{\partial}{\partial \gamma_0}\left[-\Theta(t_1)\right] \frac{\partial}{\partial \Theta} R_3\left(-\Theta(t_1)\right)\vec{x}_{t_1} \\ & + \frac{\partial}{\partial \gamma_0}\left[\Theta(t_2)\right] \frac{\partial}{\partial \Theta} R_3\left(-\Theta(t_2)\right)\vec{x}_{t_2} \Bigg\}\end{aligned} \tag{3.16}$$

for the derivative with respect to the annual libration amplitude γ_0,

$$\frac{\partial}{\partial \text{♃}} \Delta\vec{x}_{t_1\,t_2} = R_3\left(\varphi_\eta\right) R_1\left(-\eta\right) R_3\left(-\varphi_\eta\right) \left\{ \frac{\partial}{\partial \gamma_{\text{♃}}} \left[-\Theta(t_1)\right] \frac{\partial}{\partial \Theta} R_3\left(-\Theta(t_1)\right) \vec{x}_{t_1} + \frac{\partial}{\partial \gamma_{\text{♃}}} \left[\Theta(t_2)\right] \frac{\partial}{\partial \Theta} R_3\left(-\Theta(t_2)\right) \vec{x}_{t_2} \right\} \tag{3.17}$$

for the derivative with respect to the main Jupiter induced libration amplitude $\gamma_{\text{♃}}$,

$$\frac{\partial}{\partial \text{♀}} \Delta\vec{x}_{t_1\,t_2} = R_3\left(\varphi_\eta\right) R_1\left(-\eta\right) R_3\left(-\varphi_\eta\right) \left\{ \frac{\partial}{\partial \gamma_{\text{♀}}} \left[-\Theta(t_1)\right] \frac{\partial}{\partial \Theta} R_3\left(-\Theta(t_1)\right) \vec{x}_{t_1} + \frac{\partial}{\partial \gamma_{\text{♀}}} \left[\Theta(t_2)\right] \frac{\partial}{\partial \Theta} R_3\left(-\Theta(t_2)\right) \vec{x}_{t_2} \right\} \tag{3.18}$$

for the derivative with respect to the main Venus induced libration amplitude $\gamma_{\text{♀}}$. Given all these partial derivatives we can construct the matrix $\mathbf{A}$ for our system:

$$A = \begin{pmatrix} \frac{\partial}{\partial \eta} \Delta\vec{x}_{orbital} & \frac{\partial}{\partial \gamma_0} \Delta\vec{x}_{orbital} & \frac{\partial}{\partial \gamma_{\text{♃}}} \Delta\vec{x}_{orbital} & \frac{\partial}{\partial \gamma_{\text{♀}}} \Delta\vec{x}_{orbital} \end{pmatrix}. \tag{3.19}$$

Replacing the definition of the rotation model as defined in eq. (3.4) into the observable from eq. (3.11) and into the matrix above we obtain the partial derivative matrix of this system[2]. Adding more observations just means adding three additional lines per observation to the matrix $\mathbf{A}$. We now have all ingredients necessary to solve for our parameters p, so that starting from eq.(3.13) we get:

$$p^* = p_0 + (\mathbf{A}^T\mathbf{A})^{-1}\mathbf{A}^T(b_0 - \mathbf{A}p_0), \tag{3.20}$$

where p^* represents the solution for the parameters based on the initial value of p_0 for them. From all previous equations we can also construct the expression of the formal error afflicting the least squares estimate p^*

$$\sigma^* = \left(\mathbf{A}^T\mathbf{A}\right)^{-1} \frac{R^T R}{m - n}, \tag{3.21}$$

with n the number of parameters and m the number of observations, and R the vector of residuals defined as follows:

$$R = \text{Observation} - \text{Calculated} = \Delta\vec{x}(p^t) - \Delta\vec{x}(p^*)\,. \tag{3.22}$$

In order to simulate this observable and perform a full simulation of the

[2]The complete partial derivatives are very long and will not be presented here as they do not give more information than already available.

rotation experiment we need to set up some more models for the:

- spacecraft trajectory / orbit ,
- errors affecting the image position determination.

These issues are the subject of the following sections.

3.6 Spacecraft orbit model

In order to precisely model the trajectory of the BepiColombo MPO spacecraft around the planet we have to take into account several deviations from the perfect Keplerian motion. Indeed the planet cannot be considered as a spherically symmetric body because of i.e. the equatorial bulge is not perfectly spherical and various perturbations arise. Therefore we will adopt the following strategy in modelling the orbit of the satellite in a complex gravitational field.

The trajectory of an artificial satellite is in a first approximation resulting from the Keplerian motion corresponding to the point mass or spherically symmetric body potential $\frac{GM}{r} = \frac{\mu}{r}$, where G is the universal gravitational constant, M is the mass of the planet orbited by the artificial satellite, and $\mu \equiv GM$ is the product of the gravitational constant and the mass of Mercury and is known as the standard gravitational parameter. This is of course only valid as long as the satellites mass remains negligible with respect to the central body's. A more precise approach supplements the ideal Keplerian motion with the perturbations created by a certain number of perturbative forces, small with respect to the forces generated by the point mass potential. These perturbative forces create either periodic or secular effects. In general most problems encountered in the solar system possess the characteristic of having a quasi concentric shell type central body, where the point mass potential greatly outweighs the other forces. The Keplerian trajectory can thus only be used as a very gross approximation of the real trajectory. Lagrange sought to represent the solution to this problem in the same way as the solution of the two-body problem. This method brings us to the definition of osculating elements:

a	semi-major axis
e	eccentricity
i	inclination [3]
Ω	longitude of the ascending node
ω	argument of the periapsis
M	mean anomaly

[3] An orbital inclination of 0° corresponds to a prograde equatorial orbit. Positive inclinations correspond to prograde orbits.

The modelisation of the satellite motion is done by considering the simplified Lagrange equations which govern the variation of the osculating elements:

$$\begin{aligned}
\frac{da}{dt} &= \frac{2}{na}\frac{\partial F}{\partial M} \\
\frac{de}{dt} &= \frac{1-e^2}{na^2 e}\frac{\partial F}{\partial M} - \frac{\sqrt{1-e^2}}{na^2 e}\frac{\partial F}{\partial \omega} \\
\frac{di}{dt} &= \frac{\cos i}{na^2\sqrt{1-e^2}\sin i}\frac{\partial F}{\partial \omega} - \frac{1}{na^2\sqrt{1-e^2}\sin i}\frac{\partial F}{\partial \Omega} \\
\frac{d\omega}{dt} &= \frac{\cos i}{na^2\sqrt{1-e^2}\sin i}\frac{\partial F}{\partial i} - \frac{\sqrt{1-e^2}}{na^2 e}\frac{\partial F}{\partial e} \\
\frac{d\Omega}{dt} &= \frac{1}{na^2\sqrt{1-e^2}\sin i}\frac{\partial F}{\partial i} \\
\frac{dM}{dt} &= -\frac{1-e^2}{na^2 e}\frac{\partial F}{\partial e} - \frac{2}{na}\frac{\partial F}{\partial a}
\end{aligned} \tag{3.23}$$

where F is the function representing the force acting on the spacecraft. The position of the satellite is expressed in a frame centred on the centre of mass of the planet as a function of six orbital elements :

- the semi-major axis a,
- the eccentricity e,
- the orbital inclination (angular separation with respect to the equator for a prograde orbit) i,
- the longitude of the ascending node Ω,
- the argument of the periapsis ω,
- and finally the eccentric anomaly E .

In order to convert the eccentric anomaly E into the mean anomaly used in the Lagrange equations we will have to solve the Kepler equation relating both quantities (see § 3.6.4).

3.6.1 Gravitational potential

The gravitational potential of any extended body in a point external to the body can be expressed in the base of spherical harmonics, resulting in the following series:

$$U = \frac{GM}{r} + \frac{GM}{r}\sum_{n=1}^{\infty}\sum_{m=0}^{n}\left(\frac{R_{☿}}{r}\right)^n P_{nm}\left(\sin\phi_{lat}\right)\left[C_{nm}\cos(m\lambda) + S_{nm}\sin(m\lambda)\right] , \tag{3.24}$$

where all the terms in the sum represent the perturbations to the Keplerian point-mass potential. In the equation above:

- ϕ_{lat} represents the latitude of the body at which we consider the potential,
- λ represents the longitude of the body at which we consider the potential,
- R_e represents the equatorial radius of the body,
- r is the distance of the satellite from the centre of mass,
- the P_{nm} are the associated Lagrange polynomials,
- and the C_{nm}, S_{nm} the coefficients of the gravitational field.

The gravitational field of a point mass (or perfectly spherically symmetric body) only consists of the first term (degree zero potential) in this representation. Any deviation from this ideal situation gives rise to non-zero C_{nm} or S_{nm} coefficients. As these deviations from the ideal case are very small in the case of planets and large moons, we can apply the following scheme very confidently. The description of a spacecraft state in orbital elements has many advantages, mostly because certain elements can be constant in time (all except the mean anomaly M in the case of a Keplerian orbit), thus simplifying our work through a reduction in the number of varying orbital parameters.

If the chosen reference frame in which our trajectory/position is expressed is centred on the centre of mass of the central body (in this case Mercury's centre of mass) the first order ($n = 1$) spherical harmonic coefficients representing the offset between the frame origin and the body's centre of mass are equal to zero.

In the following paragraphs we will consider the effects caused by the main second and third order terms of the potential. As the gravitational field of Mercury is still very much unknown[4], we currently only have access to the second order gravitational field through C_{20} and C_{22}, at a very limited level of precision, dating from the Mariner 10 mission (*Anderson et al.* 1987). Unknown coefficients can be approximated through the use of a simple power rule developed by Kaula (*Kaula* 1966), or through the scaling of a known gravitational field (like Earth's) to Mercury. This has not been done in this work because the main orbital perturbations are caused by C_{20}, C_{22} and C_{30}, not justifying the use of high order gravitational fields. Higher degrees of the field will create perturbations that will have very short periods and very small amplitudes

[4]This is to change in the nearby future with the first results of the MESSENGER mission to Mercury scheduled to appear rapidly after orbit insertion in March 2011. The three Mercury flyby's of January 2008, October 2008 and September 2009 have not yielded conclusive values for the low level gravity field coefficients. This is due to a variety of factors, but mainly because of unfavourable flyby geometries. The absence of a good agreement between the low level gravitational field coefficient resulting from both flyby's independently has forced the MESSENGER mission team to wait for data from the third flyby in order to be able to provide a sound estimate to replace the Mariner 10 values.

with respect to the three main. As we do not consider the complete orbital restitution in this work, but approximate it to a fixed position error level depending on whether the spacecraft is seen from Earth or not, we do not need to concentrate on small periodic gravitational effects that won't alter the surface observability significantly.

The value of C_{30} we will use in our simulations is the same as currently used by ESA in all BepiColombo orbital studies, and is fixed at $0.1 \times C_{20}$ (see *Garcia et al.* 2007).

3.6.2 Lagrange Equations

At each given epoch, the satellite's position and velocity can be expressed in terms of the orbital elements of an elliptical trajectory that the spacecraft would follow if all perturbations would cease at that time, the osculating ellipse described with the osculating elements. The goal of the Lagrange equation formalism is to express the time dependent deviations of the osculating elements from the unperturbed Keplerian scenario (where all are constant except M).

It is customary to express the force function F as:

$$F = \frac{\mu}{2a} + R, \tag{3.25}$$

i.e. *Kaula* (1966, p29). The function R, comprising all terms of the potential V except the central term, is known as the disturbing function. Replacing F with R the Lagrange equations defined in eq.(3.23) yields the following form for them:

$$\begin{aligned}
\frac{da}{dt} &= \frac{2}{na}\frac{\partial R}{\partial M} \\
\frac{de}{dt} &= \frac{1-e^2}{na^2e}\frac{\partial R}{\partial M} - \frac{\sqrt{1-e^2}}{na^2e}\frac{\partial R}{\partial \omega} \\
\frac{di}{dt} &= \frac{\cos i}{na^2\sqrt{1-e^2}\sin i}\frac{\partial R}{\partial \omega} - \frac{1}{na^2\sqrt{1-e^2}\sin i}\frac{\partial R}{\partial \Omega} \\
\frac{d\omega}{dt} &= \frac{\cos i}{na^2\sqrt{1-e^2}\sin i}\frac{\partial R}{\partial i} - \frac{\sqrt{1-e^2}}{na^2e}\frac{\partial R}{\partial e} \\
\frac{d\Omega}{dt} &= \frac{1}{na^2\sqrt{1-e^2}\sin i}\frac{\partial R}{\partial i} \\
\frac{dM}{dt} &= n - \frac{1-e^2}{na^2e}\frac{\partial R}{\partial e} - \frac{2}{na}\frac{\partial R}{\partial a},
\end{aligned} \tag{3.26}$$

where we used our knowledge that $n = \sqrt{\frac{\mu}{a^3}}$ to determine the form of the last equation.

3.6.3 The perturbative term, R

In our case we only take into account the effects induced by the order two zonal coefficient C_{20}, by the equatorial bulge C_{22} coefficient, and by C_{30} the most important uneven zonal coefficient representing the pear shape of the planet. Therefore a perturbation function up to order and degree three is sufficient in our case, as any further order would be pure speculation[5]. We may consider a scaled Earth or Mars gravitational field to complement this low level field to a higher degree and order, but as we will show later on this won't have a significant effect on the results of our simulations as the high order and degree gravitational field creates periodic effects with small amplitudes. The main motivation to include J_3/C_{30} in our simulations is to anticipate possible long period effects caused by it on our orbit, as this coefficient is the dominant cause of long period variations of the orbital elements. The perturbing function R can be expressed in terms of the perturbing potential V itself expressed in terms of the orbital coordinates (see *Kaula* (1966, p37)) in the following way:

$$R = \mu \sum_{l=2}^{n} \frac{R_{☿}^{2}}{a^{l+1}} \sum_{m=0}^{m=l} \sum_{p=0}^{p=l} \sum_{q=-\infty}^{\infty} F_{lmp}(i) G_{lpq}(e) S_{lmpq}(\omega, \Omega, M, \theta)\,, \tag{3.27}$$

where θ is the planet's rotation, F_{lmp} are the inclination functions and G_{lpq} the eccentricity functions (both are time independent, if the satellite's inclination and eccentricity can be considered constant) and can be tabulated (see tab.(3.2) for the form taken by both functions in the cases needed hereafter). The S_{lmpq} are time dependent and of the following form:

$$S_{lmpq} = \begin{bmatrix} C_{lm} & l-m & even \\ -S_{lm} & l-m & odd \end{bmatrix} \cos(\Psi_{lmpq}) + \begin{bmatrix} S_{lm} & l-m & even \\ C_{lm} & l-m & odd \end{bmatrix} \sin(\Psi_{lmpq})\,, \tag{3.28}$$

with:

$$\Psi_{lmpq} = (l-2p)\omega + (l-2p+q)M + m(\Omega - \theta)\,. \tag{3.29}$$

Secular effects

When $\Psi_{lmpq} = 0$ there will be no periodic oscillations of the orbital elements the only effects being secular. To satisfy this case we get the following constraints on l, m, p and q:

$$m = 0, l = 2p, q = 0\,.$$

[5]As said previously, C_{30} has never been measured and the value used in this work is based on an estimation through other methods. It is already speculative, but highly interesting to be studied because of its important impact on long period variations in the orbital elements. The ESA chosen value of $0.1C_{20}$ represents a middle ground between a very high C_{30} of the order of C_{20} and a very small C_{30}.

This leads to the conclusion that only the even order zonal coefficients can create secular effects. Notice that R now only depends on a, e and i:

$$R_{C_{l0}} = \mu \sum_{even\, l} \frac{R_{☿}^{l}}{a^{l+1}} F_{l0\frac{l}{2}}(i) G_{l\frac{l}{2}0}(e) C_{l0}. \tag{3.30}$$

The perturbation induced by any higher order even zonal coefficient can not be distinguished from a perturbation induced by a slightly different value of C_{20}. This is what we call *lumping*. When solving for the gravitational field it is impossible to know if a secular drift was caused by a combination of $C_{l_{even}0}$'s or by a different value of C_{20} alone. Of course it is highly improbable to be in the presence of a solar system body where all $C_{l_{even}0}$ except C_{20} are exactly equal to zero. As we expect the $C_{l_{even}0}$'s value to rapidly decrease with rising l value, we can confidently restrict ourselves to C_{20} alone, obtaining:

$$R_{C_{20}} = \mu \frac{R_{☿}^{2}}{a^{3}} F_{201}(i) G_{210}(e) C_{20}. \tag{3.31}$$

Long period variations

After having considered the secular effects we will try to find out what gravitational field coefficients cause long period variations of the orbital elements. Those will arise for non-zero values of Ψ_{lmpq} in the absence of the short period terms in M and θ. The following conditions must apply:

$$m = 0, l - 2p + q = 0, l - 2p \neq 0\,, \quad or \quad m = 0, q = 2p - l, l \neq 2p\,, \tag{3.32}$$

implying that l cannot be an even number. Ψ will be of the following form:

$$\Psi_{l\,0\,p\,(2p-l)} = (l - 2p)\omega. \tag{3.33}$$

The longest periods for a given l are those minimising the absolute value of l-$2p$:

$$R_{C_{l0}} = \mu \sum_{l_{odd}} \sum_{p}^{l} \frac{R_{☿}^{l}}{a^{l+1}} F_{l0p}(i) G_{lp(2p-l)}(e) C_{l0}. \tag{3.34}$$

In our case $l = 3$ implying that ω will have the shortest frequency and thus the longest period for $p = 1$ and $p = 2$. It is these two frequencies that we will use in the following calculations. When talking about long periods in the following paragraphs we mean the *longest* periods of this system. As we have seen above, only odd zonal coefficients generate these long periods. Keeping only the longest periods we get the following combinations:

$$
\begin{aligned}
R_{C_{30}} &= \mu \sum_{p=1,2} \frac{R_{☿}^3}{a^4} F_{30p}(i) G_{3p(2p-l)}(e) C_{30} \qquad (3.35)\\
&= \mu \frac{R_{☿}^3}{a^4} \left[F_{301}(i) G_{31-1}(e) \sin(\omega) + F_{302}(i) G_{321} \sin(-\omega)(e)\right] C_{30}.
\end{aligned}
$$

As we can see from table (3.2), $F_{301} = -F_{302}$ and $G_{31-1} = G_{321}$ simplifying the above equation to:

$$
R_{C_{30}} = -2\mu \frac{R_{☿}^3}{a^4} F_{302}(i) G_{321}(e) \sin(\omega) C_{30}\,, \qquad (3.36)
$$

giving the final expression of the perturbation function due to C_{30}.

Main short period variations

If we want to consider the effects caused by the tesseral deformations of second order of the planet we have to constrain l, m, p and q as follows:

$$
l = 2,\; m = \{1, 2\},\; p = 1,\; q = 0\,,
$$

yielding the following perturbation function:

$$
R = \mu \frac{R_{☿}^2}{a^3} \left[F_{211} S_{2110} + F_{221} S_{2210}\right] G_{210}\,.
$$

As for Mercury we only have knowledge of C_{22}, and because we can consider our knowledge of the planetary rotation axis as reliable we can consider $C_{21} = 0$ and $S_{21} = 0$, finally obtaining:

$$
R_{C_{22}} = \mu \frac{R_{☿}^2}{a^3} F_{211} G_{210} C_{22} \cos(2(\Omega - \theta))\,. \qquad (3.37)
$$

The values of the functions of eccentricity (G) and inclination (F) are tabulated in various works, including *Kaula* (1966). We extract from table (3.2) the expressions of those functions used in our perturbation function.

Complete perturbing function R

Combining all three perturbation functions exposed above (eqs. (3.31), (3.36) and (3.37)) we obtain the total perturbation function we will use to model

l	p	q	$G_{lpq}(e)$
2	1	0	$(1-e^2)^{-3/2}$
3	1	-1	$e(1-e^2)^{-5/2}$
3	2	1	$e(1-e^2)^{-5/2}$

l	m	p	$F_{lmp}(i)$
2	0	1	$\frac{3}{4}\sin^2 i - \frac{1}{2}$
2	1	1	$\frac{-3}{2}\sin i \cos i$
2	2	1	$\frac{3}{2}\sin^2 i$
3	0	1	$-\frac{15}{16}\sin^3 i - \frac{3}{4}\sin i$
3	0	2	$\frac{15}{16}\sin^3 i + \frac{3}{4}\sin i$

Table 3.2: Values of eccentricity function G and inclination function F needed for the expression of the perturbing function R in our case.

BepiColombo's MPO orbit around Mercury:

$$\begin{aligned} R_{combined} =& \mu\frac{R_{☿}^2}{a^3}F_{201}G_{210}C_{20} + \\ & \mu\frac{R_{☿}^2}{a^3}F_{211}G_{210}C_{22}\cos[2(\Omega-\theta)] \\ & - 2\mu\frac{R_{☿}^3}{a^4}F_{302}(i)G_{321}(e)\sin\omega C_{30} \,. \end{aligned} \tag{3.38}$$

If we replace all inclination and eccentricity functions by their expressions in terms of orbital elements we get:

$$\begin{aligned} R =& \mu\frac{R_{☿}^2}{a^3}\left[\frac{1}{(1-e^2)^{3/2}}\left(\frac{3}{4}\sin^2 i - \frac{1}{2}\right)C_{20}\right. \\ & \left. + \frac{1}{(1-e^2)^{3/2}}\frac{3}{2}\sin^2 i\cos(2(\Omega-\theta))C_{22}\right] \\ & + \mu\frac{R_{☿}^3}{a^4}\frac{1}{(1-e^2)^{5/2}}\left(\frac{15}{16}\sin^3 i - \frac{3}{4}\sin i\right)\sin\omega C_{30} \,. \end{aligned} \tag{3.39}$$

This permits us to determine the partial derivatives of this disturbing function relative to the orbital elements, necessary for the evaluation of the Lagrange equations given in eq.(3.26).

$$
\begin{aligned}
\frac{\partial R}{\partial a} =& -\frac{1}{a}(3R_{C_{20}} + 3R_{C_{22}} + 4R_{C_{30}}) \\
\frac{\partial R}{\partial e} =& \mu \frac{3R_{☿}^2}{a^3(1-e^2)^{5/2}} \left[e\left(\frac{3}{4}\sin^2 i - \frac{1}{2}\right) C_{20} \right. \\
& + \frac{3e}{2}\sin^2 i \cos(2(\Omega - \theta)) C_{22} \\
& \left. \frac{R_{☿}}{16a\,(1-e^2)} \left(4e^2 + 1\right)(5\cos 2i + 3)\sin i \sin\omega\, C_{30} \right] \\
\frac{\partial R}{\partial i} =& \mu \frac{3R_{☿}^2}{a^3(1-e^2)^{3/2}} \cos i \left[\frac{1}{2}\sin i C_{20} \right. \\
& + \sin i \cos[2(\Omega - \theta)] C_{22} \\
& \left. - \frac{R_{☿}}{a\,(1-e^2)} e \left(\frac{1}{2} - \frac{15}{8}\sin^2 i\right) \sin\omega\, C_{30} \right] \\
\frac{\partial R}{\partial \omega} =& -\mu \frac{R_{☿}^3 e}{a^4\,(1-e^2)^{5/2}} \left(\frac{3}{2}\sin i - \frac{15}{8}\sin^3 i\right) \cos\omega\, C_{30} \\
\frac{\partial R}{\partial \Omega} =& -\mu \frac{3R_{☿}^2}{a^3(1-e^2)^{3/2}} \sin^2 i\, C_{22} \sin[2(\Omega - \theta)] \\
\frac{\partial R}{\partial M} =& 0
\end{aligned}
\tag{3.40}
$$

Replacing these partial derivatives in the Lagrange equation system eq.(3.26) we get the Lagrange equations for our particular approximation[6]:

[6]The orbital frequency n is defined as follows, $n = \sqrt{\frac{\mu}{a^3}}$

$$
\begin{aligned}
\frac{da}{dt} =&0\\
\frac{de}{dt} =&-\frac{3nR_{☿}^3}{a^3(1-e^2)^2}\left(\frac{5}{16}\sin^3 i-\frac{1}{4}\sin i\right)\cos\omega\, C_{30}\\
\frac{di}{dt} =&\frac{3nR_{☿}^2}{a^2(1-e^2)^2}\left[\sin i\, C_{22}\sin[2(\Omega-\theta)]\right.\\
&\left.+2\frac{R_{☿}}{a}\frac{e}{(1-e^2)}\left(\frac{5}{16}\sin^2 i-\frac{1}{4}\right)\cos i\cos\omega\, C_{30}\right]\\
\frac{d\omega}{dt} =&\frac{3nR_{☿}^2}{a^2(1-e^2)^2}\left[\left(\frac{5}{4}\sin^2 i-1\right)C_{20}+\left(\frac{5}{2}\sin^2 i-1\right)\cos[2(\Omega-\theta)]C_{22}\right.\\
&\left.-\frac{R_{☿}}{64ae\,(1-e^2)}\left(-3e^2-4\cos 2i+5\left(7e^2+1\right)\cos 4i-1\right)\csc i\sin\omega\, C_{30}\right]\\
\frac{d\Omega}{dt} =&\frac{3nR_{☿}^2}{a^2(1-e^2)^2}\cos i\left[\frac{C_{20}}{2}+\cos[2(\Omega-\theta)]C_{22}+\right.\\
&\left.+\frac{R_{☿}e}{2a\,(1-e^2)}(1-\frac{15}{8}\cos 2i)\csc i\sin\omega\, C_{30}\right]\\
\frac{dM}{dt} =&n-\frac{3nR_{☿}^2}{a^2(1-e^2)^{3/2}}\left[\left(\frac{3}{4}\sin^2 i-\frac{1}{2}\right)C_{20}+\frac{3}{2}\sin^2 i\cos[2(\Omega-\theta)]C_{22}\right.\\
&\left.+\frac{R_{☿}}{8ae\,(1-e^2)}\left(e^2-\frac{1}{4}\right)(\sin i+5\sin 3i)\sin\omega\, C_{30}\right]
\end{aligned}
\tag{3.41}
$$

First note that the semi-major axis of the orbit is not affected by any of the perturbations we consider, and will thus remain constant in time. We can clearly see three distinct classes of perturbations in this equation array. The first is due to C_{20} and causes only secular effects on the orbital elements, the second is due to C_{22} and creates short period variations of the elements. All terms in C_{22} are also multiplied by $\cos[2(\Omega-\theta)]$, where θ represents the planetary rotation angle. In the case of the BepiColombo MPO the frequency of $(\Omega-\theta)$ is almost equal to the planetary rotation frequency because the longitude of the ascending node Ω only varies minimally with time. Indeed the polar orbit of the MPO cancels the secular and periodic variations of Ω as they are multiplied by $\cos i$. The periodic variation of the inclination i around its equilibrium value is not going to change a lot to this fact. The periodicity of $\cos[2(\Omega-\theta)]$ is thus of the order of the half period of the planetary rotation, which equals to approximately 29 days. It is also interesting to notice that precisely a polar orbit is going to guarantee a maximal oscillation of the orbital inclination, because this term is proportional to $\sin i$. The third family of perturbations is due to C_{30} and represents long period variations. The orbital eccentricity is only affected by C_{30}. The C_{30} perturbations are always multiplied by $\sin\omega$ or $\cos\omega$. An orbit with an equatorial periapsis ($\omega = 0$, $\omega = \pi$) will tend to have a maximal perturbation on the eccentricity while the perturbation on ω, Ω and M will disappear. A polar periapsis will have the opposite effect. Intuitively this can be explained through the symmetry of the C_{30} spherical harmonic which represents a hemispheric dichotomy in mass distribution, or more intuitively a *pear shaped* planet.

This theory enables us to get the orbital parameters as a function of time and of their initial value through the integration of the derivatives in eq.(3.41):

$$\begin{aligned}
a &= a_0 \\
e &= e_0 - \frac{3nR_{☿}^3}{a^3(1-e^2)^2}\left(\frac{5}{16}\sin^3(i) - \frac{1}{4}\sin(i)\right)\frac{1}{\dot{\omega}}\cos[\omega_0 + \dot{\omega}t]C_{30} \\
i &= i_0 + \frac{3nR_{☿}^2}{a^2(1-e^2)^2}\Bigg[\sin i_0 C_{22}\frac{1}{2}\left(\cos[2(\Omega_0 - \theta(t))] - \cos[2(\Omega_0 - \theta(t_0))]\right) \\
&\quad -2\frac{R_{☿}}{a}\frac{e}{(1-e^2)}\left(\frac{5}{16}\sin^2 i - \frac{1}{4}\right)\cos i\frac{1}{\dot{\omega}}\sin[\omega_0 + \dot{\omega}t]C_{30}\Bigg] \\
\omega &= \omega_0 + \frac{3nR_{☿}^2}{a^2(1-e^2)^2}\Bigg[\left(\frac{5}{4}\sin^2 i_0 - 1\right)C_{20}t \\
&\quad -\frac{1}{2}\left(\frac{5}{2}\sin^2 i_0 - 1\right)C_{22}\left(\sin[2(\Omega_0 - \theta(t_0))] + \sin[2(\Omega_0 - \theta(t))]\right) \\
&\quad -\frac{R_{☿}}{64ae(1-e^2)}\left(-3e^2 - 4\cos 2i + 5\left(7e^2+1\right)\cos 4i - 1\right)\csc i\frac{1}{\dot{\omega}}\cos[\omega_0 + \dot{\omega}t]C_{30}\Bigg] \\
\Omega &= \Omega_0 + \frac{3nR_{☿}^2}{a^2(1-e^2)^2}\cos i_0\Bigg[\frac{C_{20}}{2}t - \frac{1}{2}C_{22}(\sin[2(\Omega_0 - \theta(t_0))] + \sin[2(\Omega_0 - \theta(t))]) \\
&\quad +\frac{R_{☿}e}{2a(1-e^2)}(1 - \frac{15}{8}\cos 2i)\csc i\frac{1}{\dot{\omega}}\cos[\omega_0 + \dot{\omega}t]C_{30}\Bigg] \\
M &= M_0 + nt - \frac{3nR_{☿}^2}{a^2(1-e^2)^{3/2}}\Bigg[\left(\frac{3}{4}\sin^2 i_0 - \frac{1}{2}\right)C_{20}t \\
&\quad -\frac{3}{4}\sin^2 i_0 C_{22}(\sin[2(\Omega_0 - \theta(t_0))] + \sin[2(\Omega_0 - \theta(t))]) \\
&\quad +\frac{R_{☿}}{8ae(1-e^2)}\left(e^2 - \frac{1}{4}\right)(\sin i + 5\sin 3i)\frac{1}{\dot{\omega}}\cos[\omega_0 + \dot{\omega}t]C_{30}\Bigg] \quad , \qquad (3.42)
\end{aligned}$$

where $\theta(t_0)$ represents the rotation phase of the planet at the start time of our simulations and $\dot{\omega}$ represents the secular trend of ω (i.e. only the perturbation due to C_{20}). All quantities indexed with 0 correspond to the initial values of the orbital parameters. The equation system above represents the model we use to extrapolate the spacecraft state (position and velocity) in time starting from an initial condition at time t_0 in our simulations.

3.6.4 Resolution of Kepler's equation

The passage from mean anomaly M, given by the Lagrange equations, and the eccentric anomaly E used in the osculating elements, is done through the Kepler equation. A unique solution to this problem exists, but as this equation is transcendental it cannot be solved in a direct manner. Luckily a lot of algorithms were developed to reach an approximate solution in a short time of this abundantly used equation:

$$M = E - e\sin(E), \tag{3.43}$$

with e the eccentricity of the considered orbit. Two solutions exist. Either a series development in eccentricity e is used or a series of Bessel functions of eccentricity. The first option converges only for $e < 0.66274$ while the second converges for all $0 < e < 1$. The Bessel series are considerably slower to manipulate than the geometric series. An intelligent choice would be to create a dynamic approach wherein the procedure applied depends on the eccentricity and precision needed, so as to always use the fastest method without sacrificing accuracy. In our case the BepiColombo orbits we study have an eccentricity lower than 0.4 for every scenario, allowing us to use the first approach:

$$\begin{aligned} E &= M + \sum_{n=1}^{\infty} a_n e^n \\ &= M + \sum_{n=1}^{\infty} \frac{e^n}{2^{n-1} n!} \sum_{k=0}^{[n/2]} (-1)^k \begin{pmatrix} n \\ k \end{pmatrix} (n-2k)^{n-1} \sin[(n-2k)M]\,. \end{aligned} \tag{3.44}$$

This series converges like a geometric series of ratio:

$$R_{☿} = \frac{e}{1+\sqrt{1+e^2}} \exp\sqrt{1+e^2}\,. \tag{3.45}$$

3.7 Error Models

In our simulation of the BepiColombo rotation experiment the following error sources are considered:

- Satellite attitude error,
- Satellite positioning error (including the star-tracker pointing error),
- Image time tagging error,
- Image correlation error.

The first three errors refer to the inaccuracy in the determination of the spacecraft's absolute position, the fourth is due to the image correlation process, mainly because of the difference in altitude and orientation between two photographs to be correlated.

3.7.1 Attitude error

The attitude error represents the misalignment of the camera with respect to the nadir pointing position due to an error in the attitude determination or control. This kind of error creates a shifting of the surface image captured from the camera with respect to the centre of the nominal nadir image. This error has been simulated with a model characterised by a randomly generated shifting vector that computes the direction and the modulus of the misalignment of the pointing direction with respect to the expected/nominal nadir position. The attitude error amplitude σ_x has been set to a value of 2.5 arcsec in this study, as given by the SIMBIO-SYS camera team (*private comm.*). This value corresponds to a minimum mission requirement. For the purposes of our simulations we use a uniform random distribution $U[0, 2\pi]$ for the direction of the attitude error, and a normal random distribution $N[0, \sigma_x]$ to model its amplitude. This creates a cone of uncertainty centred on the nominal nadir (ground track) surface in which we will randomly position the observed image centre.

3.7.2 Position error

The position error is due to the shift of the satellite centre of mass, with respect to the expected position, expressed through a random error vector with a Gaussian distribution and applied to the actual position of the spacecraft centre of mass. The orbiter position error corresponds to a surface image shift that contributes to the error on the estimation of the planetary orientation and rotation rate. The variance of this error corresponds to the precision of the satellite position estimation process, which varies according to the availability of Earth-based tracking.

Two types of error magnitudes exist depending on the tracking possibilities. The first case corresponding to a very small error of the order of 20cm (rms), applies whenever the BepiColombo MPO spacecraft is in view of and tracked by an Earth based DSN station. The second case corresponds to an error larger by 2 orders of magnitude ($\approx$ 10m) and represents the error whenever the spacecraft is not tracked from Earth. For our purposes we affect the position of simulated observations/images with an added position uncertainty in space equal to that of the satellite at the epoch of observation. The ensuing error on the Mercury surface can be estimated through the following line of thought. As the presence of a laser altimeter imposes a very high radial precision on the satellite position we can conveniently divide the error in terms of along-track, cross-track and radial components. The radial component of the spacecraft position will be a lot better constrained than the components inside the plane perpendicular to it (by about one order of magnitude typically for other space missions that include a laser altimeter). Additionally a small error on the spacecraft altitude will be of limited impact to our purposes. It will not significantly alter the surface area observed by the camera, resulting in a very small pixel size variation only. A radial error of 10 meters made from an altitude of around 1500km[7] results in a MPO HRIC pixel size variation of $\sim 0.1mm$ and is thus negligible for our purposes[8]. By contrast an along-track or cross-track error will shift the camera field of view by the same amount on the planetary surface independently of the spacecraft altitude. Thus a 10m error in the along-track/cross-track plane will result in the same shift on the surface position of the target observed. We can further simplify our reasoning because we are in the presence of a quasi polar orbit meaning that the spacecraft track is almost equivalent to meridians. The along-track error corresponds almost exclusively to a shift of the image in latitude and cross-track error to a longitudinal shift. We can confidently apply the position error in terms of an additional error on the image centre position in latitude and longitude. This is also true to a first approximation for the *less polar orbits* used in the comparisons of the two following chapters. A first correction could be to project the along-track and cross-track errors on the latitude / longitude grid. These two error components are expected to be distributed normally, to be of the same order of magnitude and be independent of each other. Following this reasoning we will apply a longitudinal and a latitudinal shift to each image centre simulated with a magnitude corresponding to the Earth-visibility conditions of the spacecraft. As the main BepiColombo tracking station is expected to be the ESA Cebreros station, only the visibility of the BepiColombo MPO from this station has been considered. This poses a worst case constraint for the Earth-based visibility of the MPO.

---

[7]The altitude of 1500km coincides with the nominal apoherm altitude of the BepiColombo MPO of 1508km. (see table (3.3))

[8]The BepiColombo HRIC has a physical sensors with 2048 × 2048 pixels, and a total field of view (FOV) of 1.47°.

3.7.3 Time tagging error

Each image is tagged with its capture time/epoch. The BepiColombo MPO on board clock has a limited precision.

The time tagging error indicates a discrete error due to the wrong time clock reference on board, it is possible that this clock precedes or delays the correct time by a second at a time, giving rise to an error of +1, 1 or zero, if the clock is synchronised with the real time. This error step is random and to its value is associated an error vector defined as the product between the velocity vector of the spacecraft per the step time; this means that the shifting is directed along track. The result is an error that can be neglected if the on-board clock can be synchronised to better than 1 millisecond. When the spacecraft is at its lowest altitude around periherm it will also be at its highest velocity and have the highest displacement rate with respect to the planetary surface. If a time tagging error is negligible at periherm, it will always be negligible.

3.7.4 Image correlation error

The image correlation error is bound to the process of correlation needed to match images. This error depends on the difference between the altitudes and camera orientations of the observations of the same bright spot and on the software code used for the correlation itself. The basic idea how to observe the libration is to take images of the same landmarks at different true anomalies of Mercury. Two pictures of the same landmark are overlaid and, with pattern matching techniques, the displacement of the surface of one image with respect to the other image is determined. *Jorda and Thomas* (2000) simulated the pattern matching of albedo features and craters for a Mercury orbiter and concluded that sub-pixel accuracy can be achieved, if images obtained at phase angles $< 5°$ and $> 55°$ are excluded (for albedo spots) and if the difference between the phase angles of the images compared/matched are smaller than 35° (for craters). In our work we use their surface illumination criteria to select favourable targets and associated images, while guaranteeing pixel-size image matching errors at most. *Tiscareno et al.* (2009) have measured the longitudinal librations of Janus and Epimetheus, two small satellites of Saturn, using images from the Cassini spacecraft currently in orbit around Saturn. In their study they show that it is possible to reach image matching error levels around 0.4 pixels.

3.8 The software tool

The approach followed in the implementation of the simulation software used in this thesis stands on the following pillars:

- **Modularity**: a clear separation of the software functions as well as the needed tasks and algorithm allowed a very structured modular solution.
- **Robustness**: the software was developed such that the user shall always obtain a clear execution output, with warning messages and defined interfaces in cases some inconsistencies are found.

A further aspect worth of mention is the scope of this software tool. It is meant to be used in the frame of preliminary estimation assessment studies, due to the limitations of the orbit estimation models used. Therefore in its current form it cannot be used for assessments in the final phases of mission developments, nor in real space operations.

As a general approach to solve the estimation problem of rotational parameters by means of a set of measurements taken by a spacecraft, the following functions can be defined:

- **Trajectory Propagation Function** (named OrbitGen) which allows propagating the spacecraft dynamics under a number of conditions that define the planetary environment and the probe features. In our case, special attention was devoted to the rotational features of Mercury and other planetary bodies, with a spin-orbit resonance motion, and the static, time-variable and tide gravitational models.
- **Measurements generation function** (named Trantor) which performs the computation of the observables necessary for the final parameter estimation process with the possibility to consider some general observational constraints.
- **Parameter determination function** (named Atlas and K2) which carries out the determination process itself. The estimation process is based on the use of certain information filtering techniques that also need the capability to compute partial derivatives of the measurements with respect to the parameters to determine. It is in this last part that constraints specific to the imaging approach are applied.

Throughout all softwares extensive use of the NASA NAIF[9] provided SPICE framework is made. SPICE is focused on simplifying calculations involving Solar system geometry. The SPICE system includes a large suite of software, mostly in the form of subroutines that customers incorporate in their own

[9]The Navigation and Ancillary Information Facility (NAIF) provides NASA planetary flight projects and NASA funded professional planetary researchers an information system named "SPICE" to assist scientists in planning and interpreting scientific observations from space-based instruments. NAIF serves as the "Navigation Node" of NASA's Planetary Data System, archiving, and providing the science community access to, SPICE data from NASA's planetary exploration missions. In addition to providing SPICE technology to NASA planetary missions the NAIF Group serves as the so-called "Navigation Node" of NASA's Planetary Data System. In this role NAIF provides a permanent archive, data distribution, and limited consultation functions for NASA planetary project SPICE data sets. More information can be found at : http://naif.jpl.nasa.gov/ .

application programs to read SPICE files and to compute derived observation geometry, such as altitude, latitude/longitude, and lighting angles. The primary SPICE data sets are often called "kernels" or "kernel files". They are composed of structured and formatted navigation and other ancillary information so that it is easily accessible and comprehensible. The SPICE kernel file contents are summarized below:

- **S**- Spacecraft ephemeris, given as a function of time.
- **P**- Planet, satellite, comet, or asteroid ephemerides, or more generally, location of any target body, given as a function of time. They can also include certain physical, dynamical and cartographic constants for target bodies, such as size and shape specifications, and orientation of the spin axis and prime meridian.
- **I** - Instrument description kernel, containing descriptive data peculiar to a particular scientific instrument, such as field-of-view size, shape and orientation parameters.
- **C**- Pointing kernel, containing a transformation, traditionally called the C-matrix, which provides time-tagged pointing (orientation) angles for a spacecraft structure upon which science instruments are mounted. May also include angular rate data.
- **E**- Events kernel, summarizing mission activities - both planned and unanticipated. Events data are contained in the SPICE EK file set, which consists of three components: Science Plans, Sequences, and Notes.

Some additional data products are also important components of the SPICE system, even if not contained in the "SPICE" acronym.

A "frames kernel" (FK file) contains specifications for the assortment of reference frames that are typically used by flight projects. This file also includes mounting alignment information for instruments, antennas and perhaps other structures of interest.

Spacecraft clock (SCLK) and leap-seconds (LSK) files are also part of SPICE; these are used in converting time tags between various time measurement systems.

The SPICE system also includes the SPICE Toolkit, a large collection of allied software. The principal component of this Toolkit is a library of portable subroutines needed to read the kernel files and to then calculate observation geometry parameters of interest. Users integrate these SPICE "Toolkit" subroutines into their own application programs to compute observation geometry parameters and related information as needed. The SPICE Toolkit was originally implemented in ANSI FORTRAN 77, but is now available in C, IDL and MATLAB as well. All this information on SPICE and more can be found at: *http://naif.jpl.nasa.gov/*.

Finally the execution of our software is controlled through a system of scripts and input files inspired from the SPICE metakernel system. All of the software code developed for this thesis has been written in Fortran 90, while all SPICE routines used are in Fortran 77. The scripts are all written in *bash*.

3.8.1 Nominal World, Real World, Estimated World

In order to understand how our software was implemented, it is necessary to always keep in mind the different modelling possibilities involved in the estimation process. These different models which we will call *worlds*, each represent a set of assumptions in terms of the system environment and computation of observables. The following environments can be defined:

- **Nominal World**: This is the perfect deterministic world, where the parameters defining the environment are perfectly known. Thus the propagation process and the measurement computations processes have deterministic formulations. In short: All the parameter values are known, no error sources exist, and the evolution of the dynamic is completely defined. This is the case when spacecraft orbits and observations are simulated.
- **Real World**: This definition corresponds to an environment that approximates the real world behaviour to our best knowledge by using a set of nominal values for its parameters and the effect of random disturbances. Thus the measurement computation process also contains stochastic components. This world is used when simulating the observables from the BepiColombo rotation experiment.
- **Estimated World**: This is the world resulting from the parameter estimation process, where departing from the nominal world parameters a least squares approach tries to adapt those parameters to the real world through a set of observables and under certain information filtering assumptions. The estimated world represents the best a posteriori knowledge of the real world which can be gained through the observations.

In the real world case, effects closer to the real behaviour of the system are included in the process in terms of mis-modelling which can be either deterministic or stochastic. That is to say, bias and/or random noises can be added to the parameters defining the proposed models, in order to approximate the real more accurately.

3.8.2 The software functions

The functions developed (already mentioned in the previous paragraph) allow carrying out several processes associated with the estimation of rotation and orientation parameters in conjunction with a spacecraft orbiting a planetary body of the Solar system. In our case this means simulating the Mercury surface observations through the BepiColombo MPO, and with this creating image-pairs used to estimate the libration amplitudes and obliquity of Mercury.

The present trajectory propagation module allows the propagation of the trajectory of the studied probe around the planetary body of interest taking into account a number of interactions. These interactions represent forces such as gravity, solar radiation pressure, albedo radiation pressure, etc. Currently only gravitational interactions are modelled and used but more can be added if needed in future studies. The trajectory propagation module computes the forward evolution of a spacecraft's position and velocity between two moments in time, starting from an initial state. The following assumptions were made in the development of this module:

- The main forces acting on the spacecraft are based on the effects of the static gravity field from the central body (as discussed in section 3.6, in our case this is limited to the effects of C_{20}, C_{22} and C_{30}).
- Solar system planets and main moons can be selected as central body in the propagation.
- The rotational state of Mercury (spin rate and orientation) is obtained from the experimental values provided through IAU 2000 values (*Seidelmann et al.* 2002).
- Several reference systems are possible for input and output of the spacecraft state (through extensive use of the NAIF SPICE framework).
- The trajectory propagation is carried out in the Mean Central Body Equator of J2000 reference system (in our case the Hermean Mean Equator of J2000).
- Planetary ephemerides from the JPL are used.
- Initial propagation conditions can be given in terms of state vector (position and velocity) or osculating orbital elements at the start epoch.

3.9 Creating/Simulating the observations

As we have defined all the models and software that we use to simulate the BepiColombo rotation experiment we now explain *how* the experiment will be performed in practice and how we simulate this.

The planned BepiColombo libration experiment has the following layout: *targets* at the hermean surface are pictured repeatedly and positioned in an inertial frame, enabling us to retrieve the planetary libration movement. The *targets* to be observed will have to be identified beforehand through the available imagery (either from MESSENGER mission data, or early MPO science operation). Two families of such *targets* exist. The first consist of fine-rimmed craters, which have a good border definition through step/abrupt crater walls for example, while the second family consists of bright albedo spots on the surface, possessing a high contrast ratio with the adhering region. The distribution at the surface of the planet of suitable targets is as of today still unknown. As such our study aims to determine regions of predilection, which will be observable in good observing conditions such as to bring in a lot of information. A good observation condition minimises image matching defects and situations where the observables will be the most affected by noise, while at the same time maximising the signal of our parameters of interest on the observables. Starting from the simulation of trajectory of the BepiColombo MPO about Mercury (as defined in section 3.6) in the HME2000 equatorial frame we construct the groundtrack[10] of the MPO on Mercury's surface (in the rotating frame) using only the uniform rotation of the planet as the libration will only have a very limited impact on the surface seen by the on-board camera, to rotate one frame towards the other. The approach we use for our simulations is to use physically based initial values of the parameters (the annual libration amplitude, the free libration amplitude, the obliquity) and then simulate the observable with the appropriate noise level. In a later step we solve for all parameters, hoping to retrieve the same initial value with an error and bias as low as possible.

Each time a chosen *target* is flown over while satisfying observability conditions, a picture of it is taken. Through regular star-tracker measurements, the orientation of the MPO in space can be precisely determined. This in turn combined with an accurate reconstructed orbit (determined through radio-tracking), will enable to precisely position the picture taken, more accurately the *target*, in inertial space enabling a comparison with past and future measurements of the same *target*.

One of the goals of our study is to determine how many targets have to be observed how many times in order to guarantee a certain accuracy on the parameters to be determined. It is possible that certain mission configurations will not be able to attain the minimum libration experiment requirements. We will try to identify them.

No target is created equal, as their position on the planetary surface will greatly influence the information on the parameters they will be bearing. It is easily conceived that as the annual libration is a longitudinal motion, a target at higher latitudes (closer to either of the poles) will be subject to a smaller absolute displacement, and as such bear less precise information. For the libration amplitude the ideal candidate is a point on the equator where the libration displacement is the greatest. In the case of the obliquity determination, the contrary is true, because the obliquity displacement is perpendicular to an axis

[10]The *groundtrack* is literally the time varying intersection of the nadir pointing vector from the satellite and the planetary surface. It represents the projection of the orbit onto the surface.

in the equatorial plane, high latitude images will contain more signal than low latitudes. Additionally the preferred timing of observations for the obliquity is different as the planet has to be observed under different orientations/viewing angles in order to create image pairs containing an obliquity signal. The obliquity signal contained in image-pairs depends on the solar longitude at the time of the observations. For the libration amplitude it is preferable to observe the planetary surface when the libration displacement is at its maximum. As the longitudes flown over at *observable* epochs depend on the initial orbital plane inclination and ascending node, some orbital configurations will be better adapted to obtain information on the obliquity. This indicates that a (complex) mix of high latitude and low latitude positions will be needed to extract both types/families of parameters from the dataset. Due to the polar orbital configuration of the BepiColombo MPO spacecraft, we can intuitively predict that the higher latitudes will be flown over a great deal more than the lower latitudes increasing the number of observation candidates at high latitudes. The observation pattern in longitude is more evenly distributed, suffering only of uneven solar illumination conditions throughout the mission timeline. All these aspects will be discussed at depth in this and the following chapter.

3.9.1 Steps of the observation simulation

We proceed in a set of distinct steps.

1. We generate BepiColombo MPO ephemerides files for each orbital configuration studied spanning 1000 days [11] starting on the planned orbit insertion date of 21st May 2020[12] with the initial orbital elements as defined in table (3.3). This is done using the spacecraft orbit generator described earlier (see section 3.8.2).

2. Second a set of all possible pictures that the spacecraft is able to take under the mission observability criteria is created. It is as if the spacecraft would only work for this experiment doing picture after picture along the whole groundtrack over which it flies in nadir pointing position. In a later stage more severe observation condition filters will be overlaid on this dataset and their individual and or combined effect on residual observation numbers compared / studied.

3. Third we generate a list of 10000 random target positions[13] on the surface, and cross it with the previously created *picture database*. This in turn gives us the maximum number of observations of the chosen targets.

[11] The planned mission duration period is of 365 Earth days, and will start approximately 1 month after the final MPO orbit is reached. We consider a longer timespan to study the potential of the spacecraft to observe long period effects.

[12] Currently ESA plans to start the commissioning of the spacecraft on July 21st 2020 and start science operations one month later.

[13] The targets are randomly distributed on a sphere. Through this *trick* we avoid having a higher target density at higher latitudes.

Here we also link the *pictures* to the chosen analysis frame, in our case the hermean mean ecliptic of date J2000 centred on the planetary centre of mass. These observations are then passed on to the next step. Using this set we extract the possible observations for each orbit type and set of observational constraints.

4. We restrain all the possible observations to limited number of targets, for which we generate image pairs. In the process of matching images we ensure that we do not compare images taken on two subsequent orbits.

5. Finally, using this filtered dataset we determine the value of the observables, calculate the partial derivatives with respect to our parameters and add noise to the observations. This is followed by the estimation of our parameters through a least squares approach.

In order to get a feeling for the minimum number of targets / observations needed to achieve the minimum requirements of the BC rotation experiment we want to visualise the solution in function of the number of targets observed at least twice (one image pair).

Orbit	altitude (km)		Initial Orbital Parameters					Secular drifts		Period
Name	periherm	apoherm	a (km)	e	i (°)	ω (°)	Ω (°)	$\dot{\omega}$ (°/y)	$\dot{\Omega}$ (°/y)	(h m s)
ESAS	400	1508	3393.7	0.1632	90.0	16	67.7	-33.949	-	2 19 m 29s
ESBS	400	2349	4111.2	0.3092	90.0	16	67.7	-24.380	-	2 47 m 40s
ESS2	400	1508	3393.7	0.1632	90.0	16	47.7	-33.949	-	2 19 m 29s
ESM2	400	1508	3393.7	0.1632	90.0	16	87.7	-33.949	-	2 19 m 29s
ESS9	400	1508	3393.7	0.1632	90.0	16	337.7	-33.949	-	2 19 m 29s
ES88	400	1508	3393.7	0.1632	88.0	16	67.7	-33.741	-2.373	2 19 m 29s
ES80	400	1508	3393.7	0.1632	80.0	16	67.7	-28.829	-11.806	2 19 m 29s
ESAN	400	1508	3393.7	0.1632	90.0	196	247.7	-33.949	-	2 19 m 29s
NKEP	400	1508	3393.7	0.1632	90.0	196	247.7	-	-	2 19 m 29s
MESS	200	15193	10136.2	0.7395	80.0	16	67.7	-4.360	-4.350	11 59 m 58s

Table 3.3: Initial BepiColombo MPO nominal orbital elements in the Mercury equatorial system on July 1st 2020, 0:00 UT and their secular drifts. The ESA baseline approach is called ESAS in this document (ESA + South). The only difference between ESAS and ESAN is the orbital insertion over the south pole or over the north pole of Mercury, resulting in a geometrically identical orbit but with the satellite direction exchanged.

Chapter 4

Results: Distribution of surface observations

Contents

Throughout the previous chapters we have laid down the base hypotheses and built the framework of our work. This naturally leads us to question ourselves as to what we will do with this tool to correctly represent the challenges lying ahead on the road to the successful realisation of the BepiColombo MPO rotation experiment. In the following sections we will identify the different mission scenarios that will be retained for the full simulation of the experiment. Given a certain number of constraints on the mission configurations that have been defined as final candidates by the European Space Agency (more precisely its operation centre ESOC), the remaining space of possible mission scenarios will be discussed. We will discuss the influence of orbital parameters /configurations on our experiment in terms of surface coverage and will then (in the next chapter) explore the influence on the retrieval of the libration amplitudes and obliquity of a mission parameter space as wide as possible. These initial constraints are listed in table (3.3).

4.1 ESA Mission Scenarios

The ESAS orbit corresponds to the nominal MPO orbit as currently proposed by ESA and its characteristics are presented in detail in table (4.1). It is a polar orbit with low eccentricity, and an orbital period of two and a half hours. The polar configuration coupled with the low altitude is optimised for planetary *cartography*. This is of course an advantage for the libration determination through a photographic method. The nominal orbit is optimised to maximise the photographic coverage of the planetary surface reducing the number of repeated overflights of identical regions, which could be a disadvantage as the libration and obliquity determination method used here needs repeated observations of surface targets. It must not be a disadvantage per se, because as we shall see in the following discussion the temporal separation of repeated observations is vital to guarantee that the image-pairs generated contain the signal of the libration and obliquity.

Parameter	Symbol	Value
semimajor axis	a	3393.7 km
periherm altitude		400 km
apoherm altitude		1508 km
eccentricity	e	0.163244
inclination	i	90.0°
argument of periherm	ω_N	196°
	ω_S	16°
longitude of ascending node	Ω_N	247.7°
	Ω_S	67.7°

Table 4.1: Initial BepiColombo MPO nominal orbital elements in the Mercury equatorial system on 14 Sep 2019, 9:29 UT. The subscript 'N' refers to a North pole orbit insertion approach whereas the subscript 'S' refers to a South pole approach. The difference between both insertions is that the spacecraft will be orbiting the planet either in a prograde or retrograde way (but in the same orbit).

The orbital elements described in table (4.1) are those defined by the European Space Agency's Space Operation Centre (ESOC) as the BepiColombo baseline orbit. This mission scenario proposes a mission launch date around July 21st 2014 resulting in an initial orbit insertion around Mercury on May 21st 2020 and reaching the final MPO orbit described above on July 21st 2020. Science operations are expected to begin after a one month commissioning phase around Aug 21st 2020. In this study we start the simulation of the orbit on the 21st of July but start the surface observations only on the 21st of August, to account for the effect of the small orbital evolution over the month of the commissioning phase. The two possible scenarios presented in tab.(4.1) describe the same orbit shape, but flown in opposite direction by the satellite. At the time of writing the South orbit insertion is the preferred ESA nominal orbit scenario. For this reason we choose to study the South insertion orbit (ESAS) case in detail, as it is not expected that the results from

ESAS and ESAN will differ significantly. Recently ESA started considering third orbit option in case the mission reaches its maximum allowable mass (called ESBS, see tab.(3.3)), differing only in the altitude of apocentre from the ESAS baseline proposal. In this scenario the orbit apoherm is not lowered as much as previously planned because of the increased quantity of fuel needed due to the higher spacecraft mass. This orbit will be studied in detail in section 4.2.5. Due to the proximity of Mercury to the Sun the BepiColombo MPO will be subjected to intense solar radiation. This poses a certain number of thermal issues, one of which in particular heavily impacts the spacecraft operations. During certain periods of Mercury's orbit around the Sun the solar radiation on the solar panels will cause them to overheat. At the basis of this lies the maximum allowable temperature of the solar panels, which cannot be crossed under penalty of permanent solar panel degradation. To limit the temperature of the panels they have to be inclined with respect to the incoming solar radiation. Ironically it is when Mercury and the spacecraft will be closest to the Sun, when the most energy is available for potential harvest, that the situation will be critical. The additional solar radiation available at perihelion will not be enough to offset the loss of power due to the additional solar panel inclination. This will reduce the power available to the MPO to the bare minimum needed to keep it alive (thermal management, attitude control, minimal communications), and science operations will not be possible. ESA has been forced to consider different science blackout periods for the MPO, which we have implemented as additional constraints in our simulations.

The primary *exclusion windows* during which no science can be performed is situated between 20° to 50° and 310° to 340° of Mercury true anomaly. These windows are always symmetrically disposed in terms of true anomaly around the Mercury perihelion, due to the fact that the nominal ESAS orbit has its orbital plane aligned with the planet-Sun direction at Mercury perihelion. In the rest of this document whenever we talk about the $20° - 50°$ Mercury true anomaly window we mean both the $20° - 50°$ and $310° - 340°$ exclusion zones. As the definitive design of the MPO is not frozen we will study the impact of two other exclusion window families. They are situated at 10° to 40° and 0° to 60° of Mercury true anomaly (each also with a *sister-window* symmetrical with respect to the Mercury perihelion (true anomaly 0°). We will study the impact of all these exclusion zones in this and the following chapter so as to predict general rules on their impact on the quality of the rotation and orientation estimation (librations & obliquity) in the frame of the BepiColombo rotation experiment.

Some preliminary mission planning has already been done by ESA in order to maximise the scientific return and guarantee the achievement of most mission goals in a minimal time frame, taking into account the limited data volume that can be transmitted from the spacecraft back to Earth. The volume of data is constrained by the characteristics of both the MPO and Earth-based antennae, the distance travelled by the signal, the quantity of solar plasma on the path of the signal and the visibility of the MPO from the Earth-based station. In the current ESA outline for the MPO science operations it is not planned to make use of the SIMBIO-SYS[1] high resolution camera (HRIC) in the first 180 mission days. The HRIC is crucial to the rotation experiment, as it is the only on-board camera with a pixel size smaller than the libration and obliquity signals we strive to estimate. The HRIC camera consists of a 2048x2048 pixels detector with a field of view (FOV) of 1.47°, implying a pixel size of 5 meters at an altitude of 400 km and 19 meters from 1500 km. In order to evaluate the impact of a 180 day delay in HRIC operations on the feasibility of the Rotation Experiment we will also study short mission durations of only 180 days (the nominal mission being 360 days).

4.2 Studied mission scenarios

Now that we have presented the orbital scenarios and mission constraints provided to us by ESA, we can try to play with the orbital parameters to see if *reasonable* changes in them lead to major improvements for our purposes. By reasonable we mean types of orbital changes that are *cheap* in terms of needed velocity change ΔV, and thus propellant consumption. Using the values provided in *Garcia et al.* (2007) we can reach the following conclusions. Changing the apoherm altitude by 100km requires about 16m/s, while the same changes for the periherm will need close to 24m/s. A change in orbital inclination by 1° needs almost 40m/s, implying that such a change is much less probable than changes in apoaltitude or perialtitude.

A lower altitude will result in higher resolution pictures and thus more accurate measurements but it will also lower the number of possible overflights of targets, reducing the number of available image-pairs. Would the rotation experiment gain from a lower periherm? Would a circular orbit increase the scientific output for our purposes? Or is the raising of the orbit going to increase the number of measurements so vastly that it will outweigh their lowered information content? In the following paragraphs we will try to answer these questions and relate these extreme cases to the nominal cases defined by ESA, so that we can judge of their pertinence for the rotation experiment.

4.2.1 Nominal orbit

Here we compare the consequences of the various observation constraints imposed by the rotation experiment on the maximum number of image-pairs obtainable over the whole planetary surface after the nominal mission duration of 360 days. We want to see what regions of the planetary surface are flown over more than once (two overflights are needed at least for an image pair) and what the impact of each observational constraint is. Figure (4.1) shows the surface distribution of all image-pairs which can be generated after 360

[1]Spectrometer and Imagers for MPO BepiColombo Integrated Observatory System

mission days (nominal) for the nominal ESAS orbit. Each dot on the latitude versus longitude map represents one target on the surface, and is coloured in function of the number of image-pairs that can be created containing this target over the nominal mission. The only constraint on imaging is that the Sun has to be over the observed target's horizon (Solar elevation must be positive). We see that more image-pairs are possible at high latitudes, which is due to the polar orbit configuration which leads the spacecraft to image high latitude regions a lot more than equatorial regions. A pattern in function of the longitude can be discerned too. The increased number of image pairs centred around the longitudes of ±90° is most probably due to the fact that the nominal mission duration of 360 days is not an exact multiple of the 176 day hermean day. Therefore a certain part of the surface has already been overflown more than the rest. The fact that the pattern seen is aligned with the North-South orbital movement and exactly 90° apart gives more weight to this hypothesis. The equatorial regions allow on average 5 image pairs to be generated for each target.

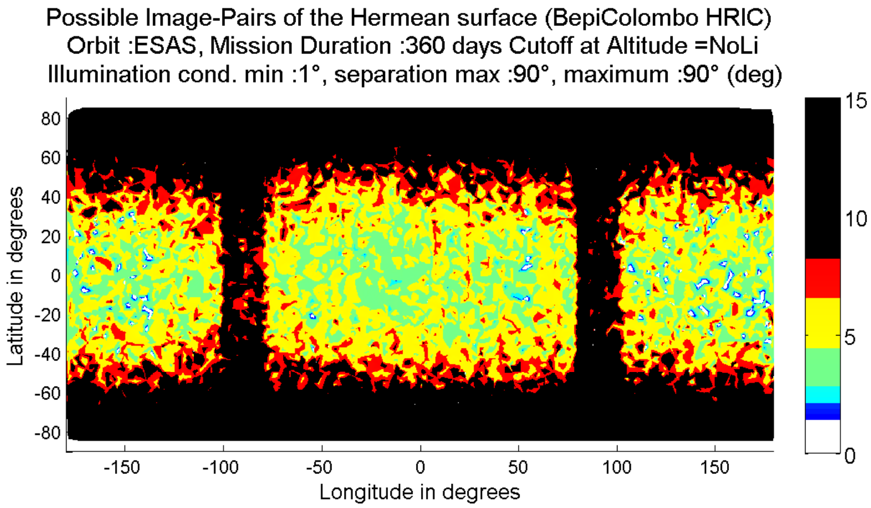

Figure 4.1: This figure represents a longitude vs. latitude map of Mercury's surface on which the number possible of image pairs for 10000 targets evenly distributed over the whole surface is represented. Each dot on the map represents one target on the surface, and is coloured in function of the number of image-pairs that can be created containing this target over 360 mission days. High latitude observations are overrepresented due to the polar ESAS orbit. The longitudinal pattern corresponds to an initial condition artefact.

An illustration of the scarcity of observation windows available enabling repeated observations of the planetary surface due to Mercury's 3:2 spin-orbit resonance and the choice of a (quasi) polar MPO orbit is shown in fig.4.2. The slanted lines represent Mercury's rotation angle Θ in an inertial frame (dotted) and the mean anomaly of the orbital motion of Mercury M (solid). The two are in resonance, that is why they are both back to the same value after exactly one Mercury solar day (176 days), corresponding to two Mercury years and three full rotations of the planet. The illumination conditions on the surface are controlled by the obliquity and the true anomaly of Mercury. As the value of the former is close to zero (2.11 arcmin, (*Margot et al.* 2007b)) the latter will be the dominant factor. The mean and true anomaly are quite different because of the large eccentricity ($\simeq 0.206$) of the orbit. In particular the illumination conditions are controlled by the difference between the planetary rotation angle and the true anomaly. The curved lines in the figure indicate the illumination phase (for a given longitude). They show the surprising property that the Sun goes back for several days in its path as seen from the surface of the planet, when the planet is near perihelion. Around perihelion Mercury travels on its orbit faster than its own rotation causing the Sun to go *backwards* for an observer on Mercury's day-side. Taking into account that the plane of the (quasi) polar orbit of BepiColombo's MPO will hardly precess (because it is on a polar orbit), the minimal visibility conditions from the MPO spacecraft are represented in the figure by two horizontal lines 180° apart; one of the two corresponds to passages closer to periherm, the other to passages closer to apoherm, thus at a larger MPO altitude (with imaging at a lower resolution). The opportunities to image a patch located on a given meridian are represented by the intersections of the horizontal lines (``the orbit ground-track'') with the dotted diagonal lines representing the rotation of the planet (see fig.4.2). There are 12 intersections in the nominal mission duration of one terrestrial year (~ 2 Mercury days). This corresponds to one target overflight every half Mercury rotation or 29 days. Additionally the polar orbit plane of the MPO will not drift and to a first approximation the planet revolves under the spacecraft. However, at the times corresponding to these intersections, we need to check the illumination conditions: there will be (on average over a range of longitudes) 6 opportunities when the surface patch will be on the day-side and be illuminated (the 6 others happening at night). Because of the resonance, the figure repeats exactly every Mercury day (176 days), thus for each patch on the surface there are two ``identical''groups of (on average) 3 images. By identical we mean: identically illuminated and observed at the *same* Mercury true/mean anomaly. The libration in longitude has the mean anomaly as an argument, thus by correlating images taken one Mercury day apart we would obtain no information on the annual libration amplitude γ. The image pair maps made here do not contain this information, hence most of the planetary surface is observed 6 times yielding 5 image-pairs, while some regions (mainly polar) contain overflights with less than 29 days between them, up to subsequent orbits. As already explained earlier certain longitudes will be *oversampled* with respect to others because most mission durations considered are not integer multiples of one Mercury day. The above reasoning is made for the case of a Keplerian orbit without any secular or periodic variations. As we have seen in earlier chapters of this work this is not a good approximation as the perturbative effects of the low-order gravity field harmonics will be *quite large* relative to the signal of our parameters. Taking these effects into account changes figure (4.2) slightly, so that only on average after 176 days the MPO will fly over the same surface regions and the whole set of possible observations will take 176 days or longer to fill (in steps of half Mercury rotations, corresponding to $\sim$ 29 days, because the orbit plane does not precess and the planetary rotation unfolds *under* the satellite), especially if we limit the spacecraft altitude below which imaging of targets is allowed.

Because of the planets 3:2 spin-orbit resonance, and the fact that the spacecraft's orbital plane will stay fixed in space [2] a maximum of three overflights will be possible. If more are registered on the map above, they account for observations happening on subsequent orbits. This is made possible by the fact that the camera's field of view will be sufficiently wide when flying at high altitude over the surface, to re-observe part of the previously overflown surface on the following orbit.

4.2.2 Illumination constraints

The nominal observation constraints used in this study are as follows:

- Minimum solar elevation angle on the observed surface region: 35° ,
- Maximum solar elevation angle on the observed surface region: 85° ,
- Maximum difference in illumination angle between two images, to be able to compare them successfully: 35° .

Jorda and Thomas (2000) simulated the pattern matching of albedo features and craters for a Mercury orbiter and concluded that sub-pixel accuracy can be achieved, if images obtained at phase angles below 5° and above 55 ° are excluded (for albedo spots) and if the difference between the phase angles are smaller than 35° (for craters). All these illumination constraints are to our knowledge not fixed precisely in a definitive way, but are to be understood as worst cases.

The main consequence of restrictions on the solar incidence is to exclude observations at latitudes higher than 55° where the Sun *never* rises above 35° in the sky. Small patches of surface where the Sun is close to a zenithal position on overflight will also be excluded due to the lack of contrast arising from this situation. An important part of Mercury's surface is covered with *albedo spots*, small features with a very different albedo than their surroundings. As the albedo contrast tends to disappear for a very high solar incidence angle / Sun close to the zenith, the loss of albedo features and overall contrast, renders the image matching techniques all but useless. The same can be said of the usual topographic image matching. When correlating images of the planetary surface of Mercury we only have two main characteristics of the surface to

[2] As we have seen previously (see chapter 2) because of the polar configuration of the nominal orbit the ascending node Ω will not be affected by a secular drift. This causes the spacecraft to fly over the same longitude a maximum of 6 times over the course of one Mercury day. Three of those passages will occur during night, leaving only three possible overflights during daytime.

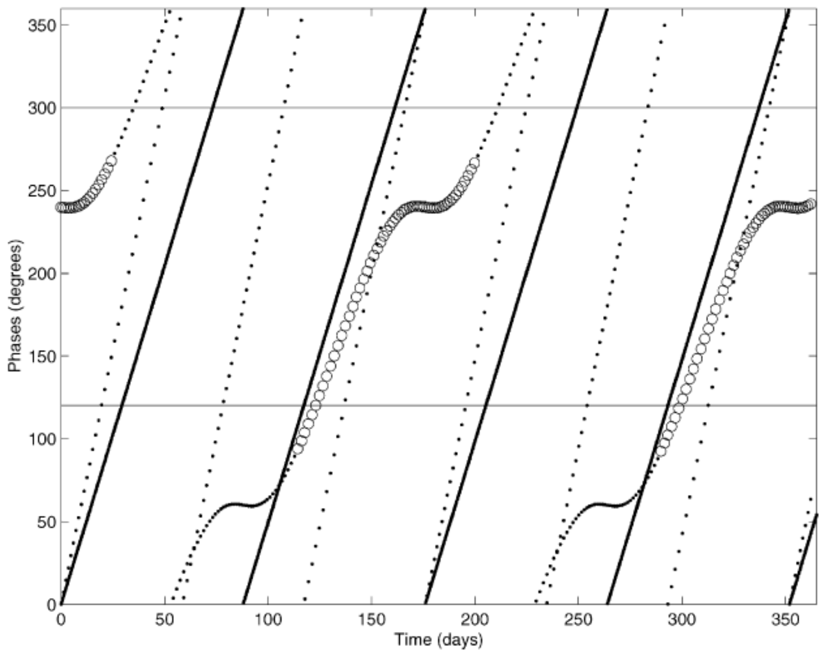

Figure 4.2: Visibility conditions for the rotation experiment. The slanted dotted line is the *rotational* angle Θ of Mercury (as defined in section 3.2.1), the slanted solid line is the *mean anomaly* M of Mercury. The curved line is the true anomaly f of Mercury minus the rotation angle Θ, which defines the minimal illumination conditions: the Sun must be over the local horizon. The line is drawn with small dots when the Sun is above the local horizon and with circles when below (at some reference longitude). The horizontal lines indicate the location of the sub-satellite points in the orbital plane at some target longitude (where the planetary rotation unfolds under the orbital plane). (credit: *Milani et al.* (2001)).

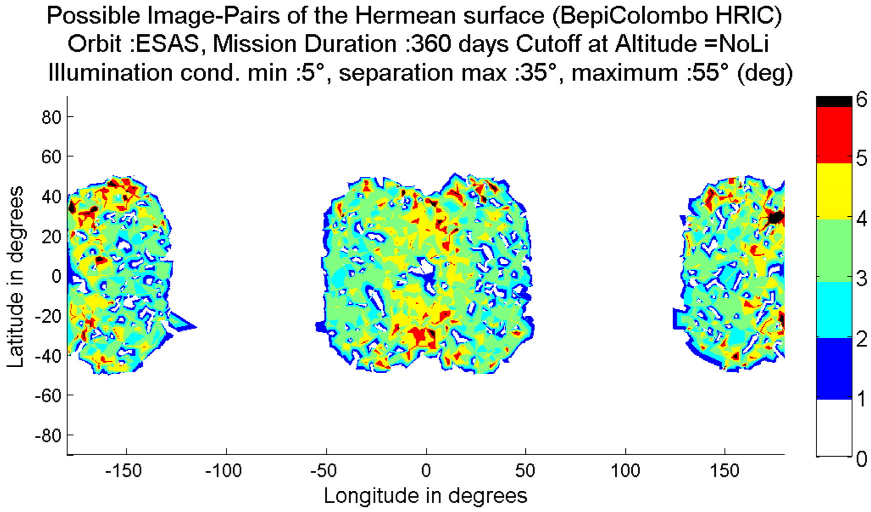

Figure 4.3: Distribution of surface regions which are observable at least twice and from which at least one image comparison can be constructed. The colour scale represents the number of such image comparisons which are possible. The observations have been filtered according to an illumination constraint excluding all low solar elevations (below 35°), very high solar elevations (above 85°) and imposing that inside an image-pair the illumination angle difference cannot be greater than 35°.

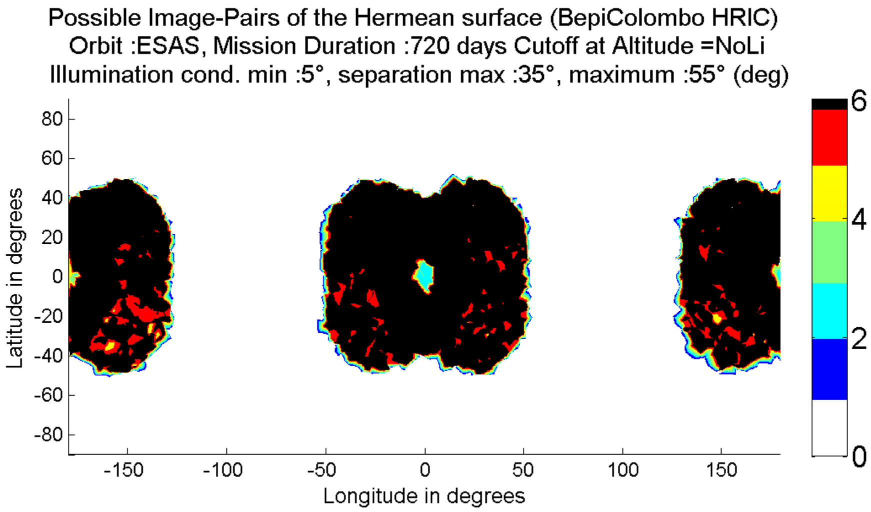

Figure 4.4: Distribution of surface regions which are observable at least twice and from which at least one image comparison can be constructed over 720 mission days. The colour scale represents the number of such image comparisons which are possible. The observations have been filtered according to an illumination constraint excluding all low solar elevations (below 35°), very high solar elevations (above 85°) and imposing that inside an image-pair the illumination angle difference cannot be greater than 35°.

turn to; craters, and albedo spots. The rims of craters are very useful to precisely align overlapping images with each other, given that they are finely resolved enough. The main limiting factor for this is the crater morphology itself, over which we do not have any control, and the crater illumination. If it is too grazing (low incidence angle) or too zenithal (high incidence angle) we will either have very long shadows or completely absent shadows. If no shadow is present it is impossible to correctly position the features on the surface, in addition to the fact that for very high solar incidences the contrast of images is heavily reduced, depriving us of potential albedo spots to perform the matching.

The effects of applying these nominal illumination constraints to the dataset used for figure (4.1) can be seen in figure (4.3). All possible image-pairs are confined to two spatially separated regions in longitude and between $-50°$ and $50°$ in latitude. As no solar incidence above $55°$ is allowed, this automatically excludes all latitudes above $55°$ North and South because the Sun never rises above this limit at these latitudes. Due to Mercury's very small obliquity the solar illumination angles are symmetrical with respect to the equator. The latitudinal symmetry is due to the fact that the initial orbital configuration is optimised to compensate for the secular drift of the periherm over the nominal mission duration period. In the ESAS case the periherm will advance[3] by about $33°$ per year, and starting at $196°$ will reach $164°$ after one year and $131°$ after 720 days of mission. Because of this in the second year of mission we fly at higher altitudes South of the equator than North of the equator where the periherm is located. Observing the surface from a higher altitude multiplies the potential imaging overlaps of a certain region, which is what we are looking for, though as we shall see in the restitution analysis more observation pairs do not necessarily mean a better estimation of our parameters, because the measurement errors are very sensitive to the altitude. The comparison of both figures (4.1) and (4.3) shows the enormous impact in terms of available image-pair opportunities that the illumination conditions have. All regions that were previously most abundant in image-pairs are now completely empty. This should be seen as a warning signal not to jump to early conclusions that regions on the planetary surface that are observed more are also *rich* in high-quality observations.

Extending the mission duration to 720 days will not expand the surface regions contributing to the image pairs as can be seen from figure (4.4). The same surface regions contributing over the first 360 days will continue over the next 360 days causing a doubling of the number of image pairs.

4.2.3 Altitude constraints

If we consider a limitation of 1000km in the altitude allowed to take pictures of the surface (not changing any other parameter) we will significantly reduce

[3] By advance of the periherm we mean the fact that the periherm occurs earlier in the orbit path than it would have been expected.

the number of image pairs we can obtain as can be seen in fig. (4.5). As images taken at altitudes lower than 1000 km are exclusively taken on the periherm side of the spacecraft orbit, we eliminate all potential observations from the apoherm side of the orbit. Because images taken on the apoherm orbit half cover a wider part of the surface (but at a reduced spatial resolution), this means that we eliminate more than half of our image pairs.

If we double the mission duration from 360 days to 720 days we can clearly see an increase in the number of potential image pairs. As previously explained (see §4.2.1) the North/South symmetry that existed previously has now disappeared because of the longer mission duration and the fact that the periherm positions during the last 360 mission days are not distributed symmetrically about the equator (see fig. (4.6)). As we cannot know what corrective action the spacecraft operators will take in a potential extended mission we won't explore different time lines, or different orbital evolution scenarios. But in order to help them choose between all available options we will present the main orbit alterations possible and their consequences on the rotation experiment.[4]

In fig. (4.5) we can see that only two elliptic surface regions situated at 180° of longitude of each other are able to provide image pairs for the rotation experiment. They are about 45° in North-South direction and around 50° wide in longitude at the equator. A target situated inside one of those zones will provide at most 2 useful image pairs for our experiment. In the following chapter where we analyse the restitution of our parameters we will show how this impacts the precision and bias on the rotation / orientation parameters. If we reduce the mission duration even further to around one Mercury solar day (two Mercury revolutions / three Mercury rotations) we completely eliminate one of the observation zones and only moderately affect the other one (see fig. (4.7)). We have previously shown that on average the MPO can only fly over a given target 6 times over 360 days. This must be reduced to 3 times over 180 days. From these three observations either one, two or all three are made at night with the other two, one or zero day-side observations made during the following 180 days (to reach 6 observations from which 3 on the day-side).

As discussed earlier low altitude observations of the surface are made exclusively on the periherm side of the orbit. Due to the polar orbit configuration, the MPO orbit's ascending node will not exhibit a (significant) secular drift. Its spatial orientation can thus be considered fixed once and for all. This has led us to define the β-angle as the angle between the orbit plane and Mercury's line of periapsis (see figure (4.13)). In the ESAS orbital configuration the periherm side of the MPO orbit is over the sunlit surface when Mercury is at its aphelion. The spacecraft will be flying over the day-side of the planet at higher altitudes than the night-side. This is done on purpose to reduce the

[4]Spacecraft orbits are routinely altered in order to adapt to evolving mission requirements especially during extended mission phases, as is currently the case for both ESA spacecraft Mars Express (MEX) and Venus Express (VEX). The orbit of MEX is periodically altered in order to cover certain surface regions preferentially, or to increase the number of close encounters with the martian moon Phobos. The periapsis of VEX's orbit has been lowered and raised several times in order to perform atmospheric drag experiments.

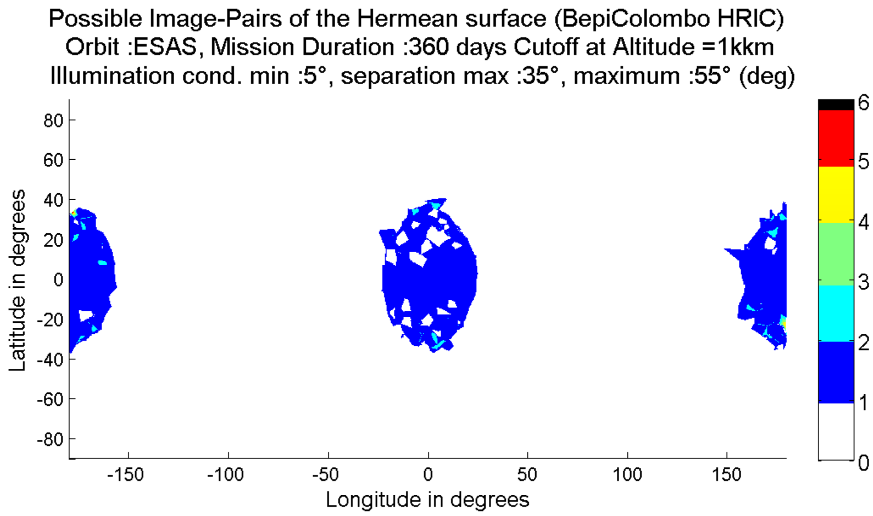

Figure 4.5: Distribution of surface regions which are observable at least twice and from which at least one image comparison can be constructed over the nominal mission duration of 360 days. The colour scale represents the number of such image comparisons which are possible. The observations have been filtered according to an altitude constraint excluding all observations made above 1000 km in altitude and an illumination constraint excluding all low solar elevations (below 35°), very high solar elevations (above 85°) and imposing that inside an image-pair the illumination angle difference cannot be greater than 35°.

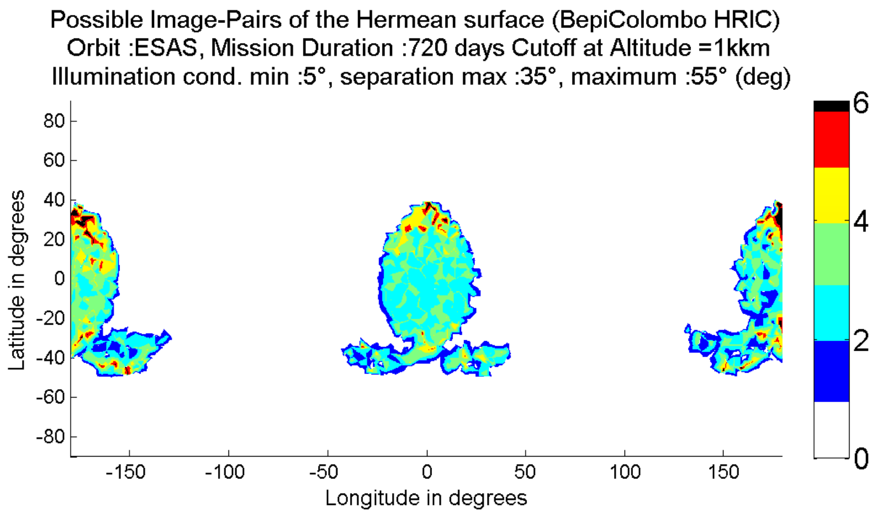

Figure 4.6: Distribution of surface regions which are observable at least twice and from which at least one image comparison can be constructed over **a mission duration of 720 days**. The colour scale represents the number of such image comparisons which are possible. The observations have been filtered according to an altitude constraint excluding all observations made above 1000 km in altitude and an illumination constraint excluding all low solar elevations (below 35°), very high solar elevations (above 85°) and imposing that inside an image-pair the illumination angle difference cannot be greater than 35°.

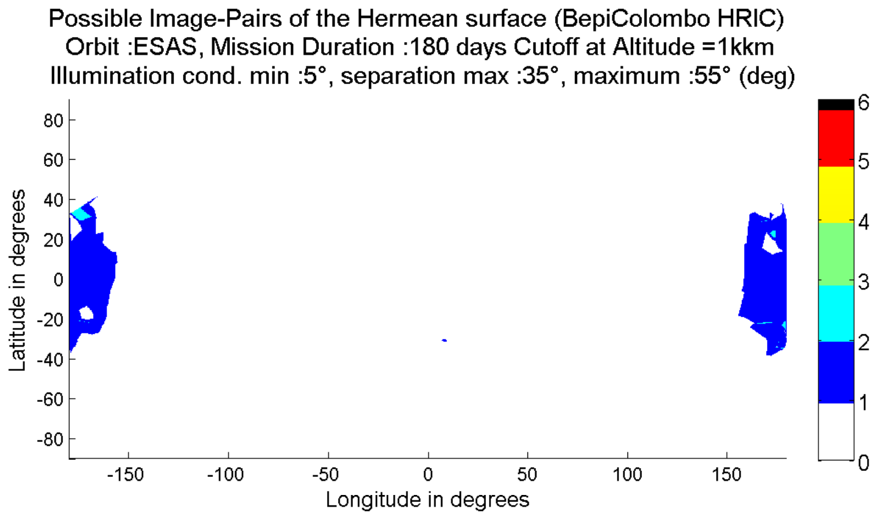

Figure 4.7: Distribution of surface regions which are observable at least twice and from which at least one image comparison can be constructed over a mission duration of **only 180 days**. The colour scale represents the number of such image comparisons which are possible. The observations have been filtered according to an altitude constraint **excluding all observations made above 1000 km in altitude** and an illumination constraint excluding all low solar elevations (below 35°), very high solar elevations (above 85°) and imposing that inside an image-pair the illumination angle difference cannot be greater than 35°.

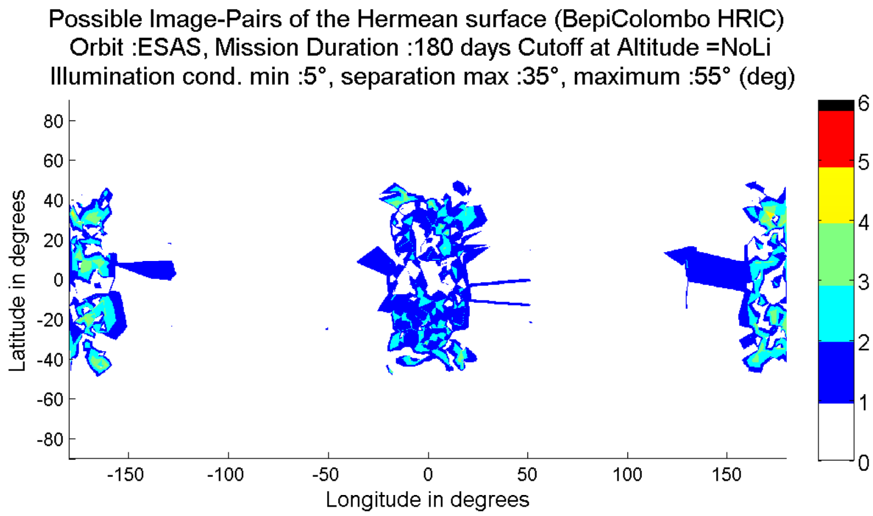

Figure 4.8: Distribution of surface regions which are observable at least twice and from which at least one image comparison can be constructed over a mission duration of **360 days**. The colour scale represents the number of such image comparisons which are possible. The observations have not been filtered according to an illumination constraint excluding all low solar elevations (below 35°), very high solar elevations (above 85°) and imposing that inside an image-pair the illumination angle difference cannot be greater than 35°.

power of the planetary infrared radiation hitting the spacecraft which could overheat the nadir pointing instruments. This orbital orientation also ensures that at the Mercury periherm the MPO apoherm side will be situated over the sunlit-side of the planet.

4.2.4 True Anomaly limitations

After having considered the illumination and altitude constraints we now turn to the true anomaly exclusion zones imposed by the thermal management of the solar panels (as explained earlier). Comparing figures (4.9) and (4.5) no difference in observation numbers and distribution can be seen. The nominal true anomaly exclusion zone does not impact the observations that can be made under nominal altitude and illumination conditions. It is only when we look at fig. (4.10) and compare it with fig. (4.3) that we see the effect of the true anomaly exclusion zone, as two longitudinal blackout bands situated between 20° and 50° of East and West longitude. Similarly when considering different true anomaly exclusion zones the same pattern will arise. The excluded true anomalies are related to the planetary longitudes affected. Therefore we can say that if an exclusion zone contains the true anomalies from 0° to 10° the surface region containing observations centred on the prime meridian (longitude 0°) will be reduced or even completely wiped out.

4.2.5 Higher altitude orbit based on the nominal case (ESBS)

In this paragraph we consider an ESA proposed alternative to the nominal (ESAS) orbit, which exhibits a higher apoaltitude but retains the same perialtitude and orbital orientation characteristics (ESBS). The raise of the apoaltitude to 2943km from 1508km in the *nominal* case could be imposed if all the MPO spacecraft components were to exploit their 20% mass margin. The increased spacecraft mass would make it more costly in terms of fuel to lower the apoherm to the planned altitude, and the requirement to stay in resonance with the Mercury Magnetospheric Orbiter (MMO)[5] sister-spacecraft imposes a discrete number of acceptable orbits. This particular change in orbit represents the passage from a 4:1 to a 3:1 resonance between MPO and MMO.

A comparison between figures (4.11) and (4.3) shows no significant difference in the surface regions useful to our experiment, but a clear increase in the number of image pairs can be seen for the *new* high apoherm orbit. This can be attributed to the fact that images taken at a higher altitude will cover a wider surface swath, thus contributing to more potential image pairs.

[5]The BepiColombo mission is composed of two Mercury orbiters. The Mercury Planetary Orbiter (MPO) situated in a low altitude orbit optimised for planetary survey and the Mercury Magnetospheric Orbiter (MMO) situated in a highly eccentric orbit optimised for magnetospheric studies. Both spacecraft are planned to evolve in resonant orbit so as to make certain *tandem observations* possible at regular intervals.

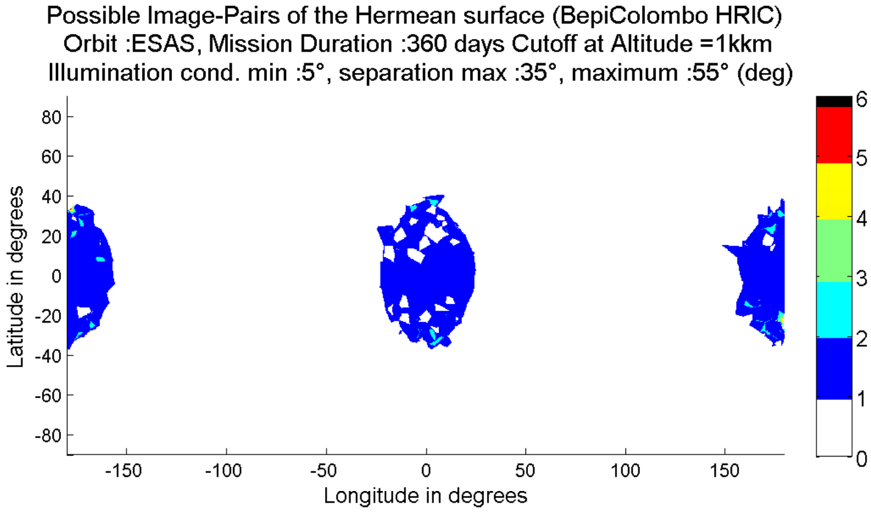

Figure 4.9: Distribution of surface regions which are observable at least twice and from which at least one image comparison can be constructed over a mission duration of 360 days. The colour scale represents the number of such image comparisons which are possible. The observations have been filtered according to an altitude constraint excluding all observations made above 1000 km in altitude and a science exclusion zone between 20° to 50° and 310° to 340° of Mercury true anomaly, and an illumination constraint excluding all low solar elevations (below 35°), very high solar elevations (above 85°) and imposing that inside an image-pair the illumination angle difference cannot be greater than 35°.

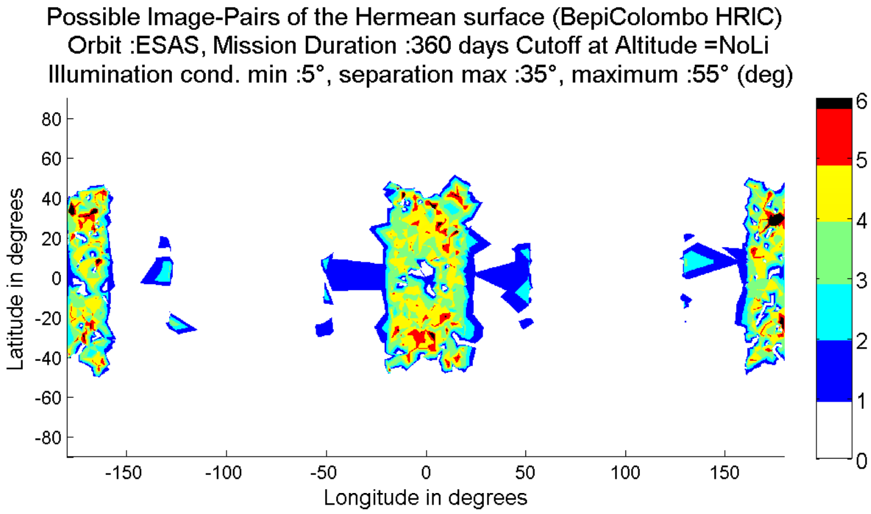

Figure 4.10: Distribution of surface regions which are observable at least twice and from which at least one image comparison can be constructed over a mission duration of 360 days. The colour scale represents the number of such image comparisons which are possible. The observations have **not** been filtered according to an altitude constraint but a science exclusion zone between 20° to 50° and 310° to 340° of Mercury true anomaly, and an illumination constraint excluding all low solar elevations (below 35°), very high solar elevations (above 85°) and imposing that inside an image-pair the illumination angle difference cannot be greater than 35°, have been implemented.

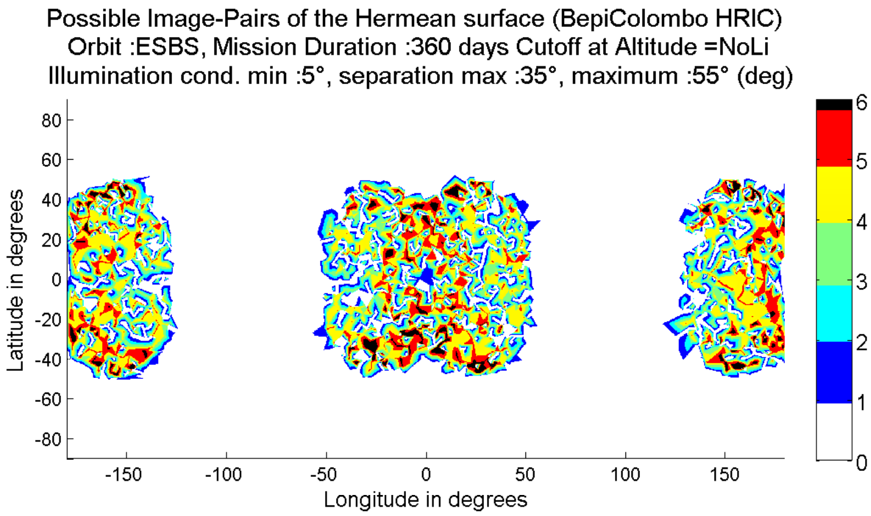

Figure 4.11: Distribution of surface regions which are observable at least twice and from which at least one image comparison can be constructed over a nominal mission of 360 days, **for the high apoherm ″ESBS″ scenario**. The colour scale represents the number of such image comparisons which are possible. The observations have only been filtered according to an illumination constraint excluding all low solar elevations (below 35°), very high solar elevations (above 85°) and imposing that inside an image-pair the illumination angle difference cannot be greater than 35°.

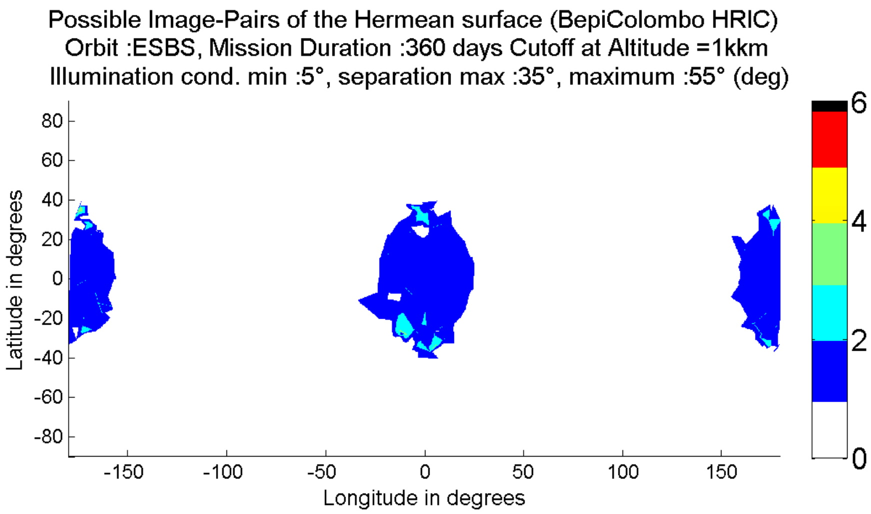

Figure 4.12: Distribution of surface regions which are observable at least twice and from which at least one image comparison can be constructed over a mission duration of 360 days, for the high apoherm ″ESBS″ scenario. The colour scale represents the number of such image comparisons which are possible. The observations have been filtered according to an altitude constraint **excluding all observations made above 1000 km in altitude** and an illumination constraint excluding all low solar elevations (below 35°), very high solar elevations (above 85°) and imposing that inside an image-pair the illumination angle difference cannot be greater than 35°.

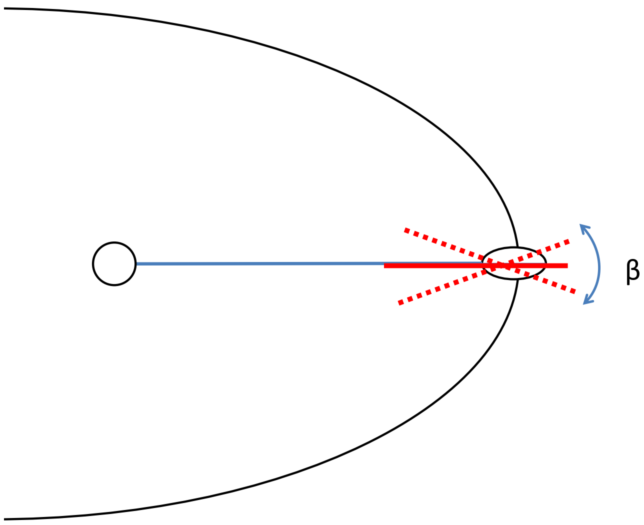

Figure 4.13: The β angle of an orbit is the angle between the direction of the apoapsis side of the orbital plane and the Mercury-Sun axis. The nominal BepiColombo configuration has $\beta = 0°$. For polar orbits we have shown that the orbital plane does not precess and thus β remains constant for them.

If we restrain the observations to altitudes below 1000 km we can see that all apoherm side images are excluded causing a significant reduction in size of both observable regions (fig. (4.12)) and less useful image pairs than for the nominal orbit in the same conditions (see fig. (4.5)).

At this point of the study it is impossible to conclude if this orbit allows a parameter estimation quality similar to the ESAS orbit just by looking at image-pair distribution maps. This will have to be determined at a later stage of our study (see chapter 5). Nevertheless we can already conclude that the ESBS orbital scenario delivers similar number of image-pairs located in essentially the same regions as the ESAS scenario.

4.2.6 Orbit based on the nominal case with an offset in the longitude of ascending node

We now study the effects of the previously defined β angle on the image pair number and distribution (see fig.4.13). To this aim we consider an orbit with a β-angle of 90° and compare the obtained image-pair maps to those of the nominal *ESAS* orbit.

In the altitude-unlimited case and for 360 mission days we note that the *ESS9* orbit with a β-angle of 90° would provide image-pairs over wider surface regions than the nominal case (fig. (4.14) compared to fig. (4.3)). Close to the equator we almost have a complete longitudinal coverage of the surface. A better coverage of the surface and more available image pairs are *not* indicative

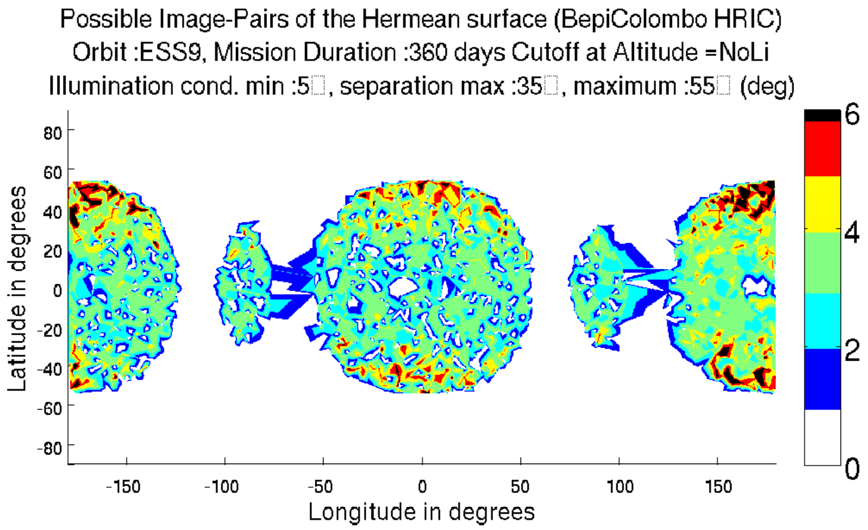

Figure 4.14: Distribution of surface regions which are observable at least twice and from which at least one image comparison can be constructed over a nominal mission of 360 days, **for the $\beta = 90°$ "ESS9" scenario**. The colour scale represents the number of such image comparisons which are possible. The observations have only been filtered according to an illumination constraint excluding all low solar elevations (below 35°), very high solar elevations (above 85°) and imposing that inside an image-pair the illumination angle difference cannot be greater than 35°.

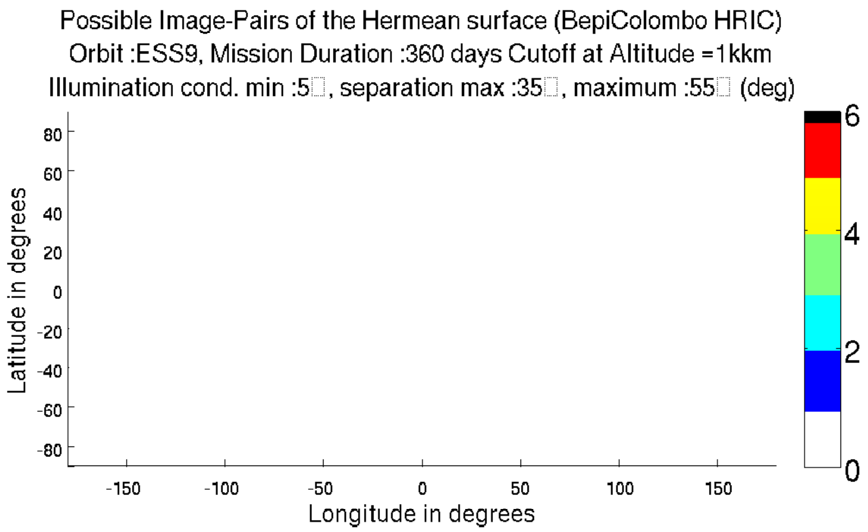

Figure 4.15: Distribution of surface regions which are observable at least twice and from which at least one image comparison can be constructed over a nominal mission of 360 days, for the $\beta = 90°$ "ESS9" scenario. The colour scale represents the number of such image comparisons which are possible. The observations have been filtered according to an altitude constraint **excluding all observations made above 1000 km in altitude** and an illumination constraint excluding all low solar elevations (below 35°), very high solar elevations (above 85°) and imposing that inside an image-pair the illumination angle difference cannot be greater than 35°.

of a better estimation of our parameters. This is due to the fact that the time interval between the individual images in one image pair, and the individual epoch, both have their importance too. The spatial distribution may be good, but we also have to look at the distribution in time. A simple example to illustrate this would be the restitution of a purely sinusoidal signal. If we have information/observations only at times where the signal is close to zero we won't be able to adjust the amplitude correctly. On the contrary if we have observations during the minimum and during the maximum the amplitude will be evaluated way better. In the following chapter we will show that this is the case for the annual libration amplitude and orbits with *high* β-angles. This type of graph has the disadvantage of not telling us at what altitude the images used in the image pairs have been taken. Limiting the maximum imaging altitude to 1000 km as we have done before we see that most images were actually obtained at altitudes higher than 1000 km, when comparing figure (4.15) to figure (4.14). Under nominal illumination and altitude conditions this orbital scenario cannot deliver a single image-pair, and is therefore to be abandoned. Studying smaller β-angle variations yields more information on the sensibility of the observation distribution to the β-angle.

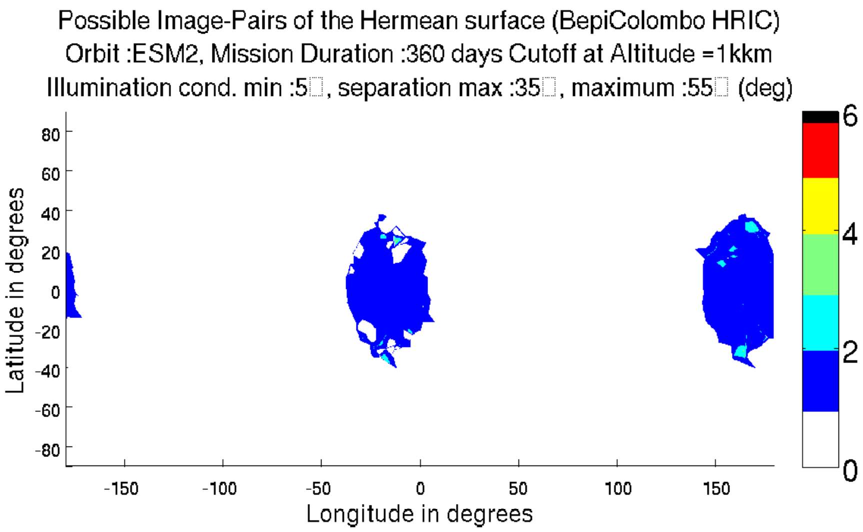

Figure 4.16: Distribution of surface regions which are observable at least twice and from which at least one image comparison can be constructed over a nominal mission of 360 days, **for the** $\beta = -20°$ **"ESM2" scenario**. The colour scale represents the number of such image comparisons which are possible. The observations have been filtered according to an altitude constraint **excluding all observations made above 1000 km in altitude** and an illumination constraint excluding all low solar elevations (below 35°), very high solar elevations (above 85°) and imposing that inside an image-pair the illumination angle difference cannot be greater than 35°.

If we reduce the observation duration to 360 days as done previously with the

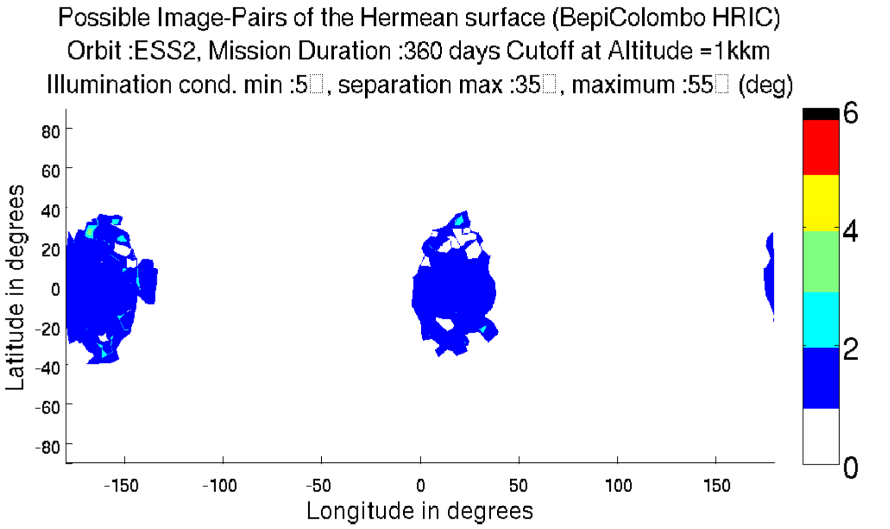

Figure 4.17: Distribution of surface regions which are observable at least twice and from which at least one image comparison can be constructed over a nominal mission of 360 days, **for the** $\beta = 20°$ **"ESS2" scenario**. The colour scale represents the number of such image comparisons which are possible. The observations have been filtered according to an altitude constraint **excluding all observations made above 1000 km in altitude** and an illumination constraint excluding all low solar elevations (below 35°), very high solar elevations (above 85°) and imposing that inside an image-pair the illumination angle difference cannot be greater than 35°.

other orbits, no image-pairs subsist. This orbit is clearly not optimal for the purposes of our experiment because suitable image-pairs will only arise (in significant numbers) after 360 mission days (the nominal mission).

This is also the case of two orbits with a very low β-angle deviation, ESS2 and ESM2 (presented in figures (4.17) and (4.16) respectively) with $\beta = 20°$ and $\beta = -20°$ respectively. For the nominal mission no image-pair will be generated if we constrain the maximum imaging altitude below 1000 km. This shows the restrictive character of the imaging conditions imposed by the rotation experiment. The $\beta = 0°$ case seems to be *well-suited* to provide a large number of image-pairs.

If β is 0°, then low-altitude images can be taken during a long time around aphelion. On the contrary if β is 180°, the part of Mercury's surface which can be imaged from low altitude is much smaller, because Mercury spends less time around perihelion. If on the other hand β is close to 90° or 270° we will get no useful observations at either aphelion or perihelion because the spacecraft will be flying over the terminator. It will be impossible because of our illumination constraints to image the surface for a long time around both perihelion and aphelion, until the solar incidence angle descends below 55°. In this case the only usable observation periods will be situated symmetrically between aphelion and perihelion, reducing the librational displacement of the surface observed.

4.2.7 *Less polar* orbit

The influence of one last orbital parameter has still to be discussed: orbital inclination. In the following we will consider a spacecraft orbit with 85° inclination (ES85) instead of the nominal 90° as our spacecraft orbit and compare its observation opportunities with the nominal orbit (ESAS).

Figure (4.18) is not significantly different from its nominal equivalent fig.4.3. Nevertheless the huge excess in image-pairs and complete longitude coverage of the less polar orbit has almost completely disappeared if we consider the 1000 km altitude limit for only 360 mission days (see fig. (4.19)). In this case the two orbits deliver image-pairs above the same restrained surface regions, but the diminished orbital inclination will favour more crossings of the spacecraft surface track at lower latitudes, slightly increasing the number of image-pairs inside the observable regions.

4.2.8 MESSENGER type orbit

To quickly visualise the advantages of a BepiColombo MPO orbit for the type of experiment foreseen a brief comparison with the orbit of the American MESSENGER mission follows.

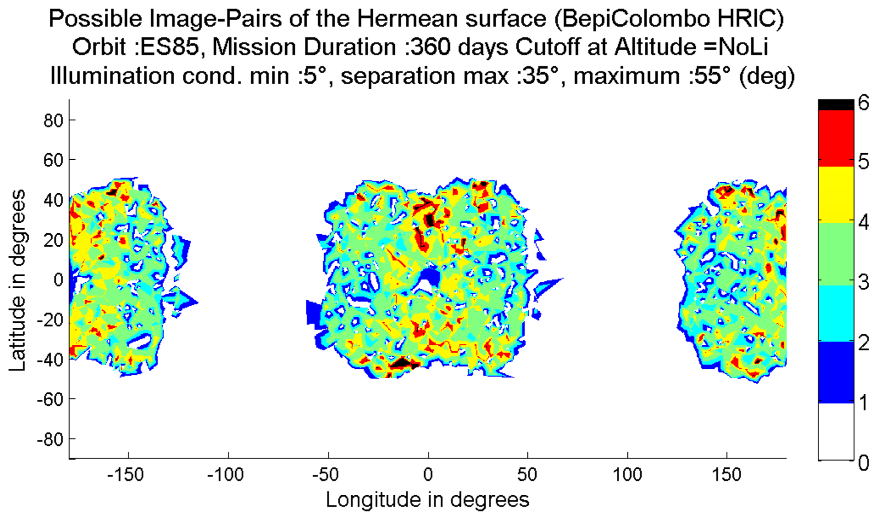

Figure 4.18: Distribution of surface regions which are observable at least twice and from which at least one image comparison can be constructed over a nominal mission of 360 days, **for the** $\beta = 20°$ **"ES85" scenario**. The colour scale represents the number of such image comparisons which are possible. The observations have been filtered according to an illumination constraint excluding all low solar elevations (below 35°), very high solar elevations (above 85°) and imposing that inside an image-pair the illumination angle difference cannot be greater than 35°.

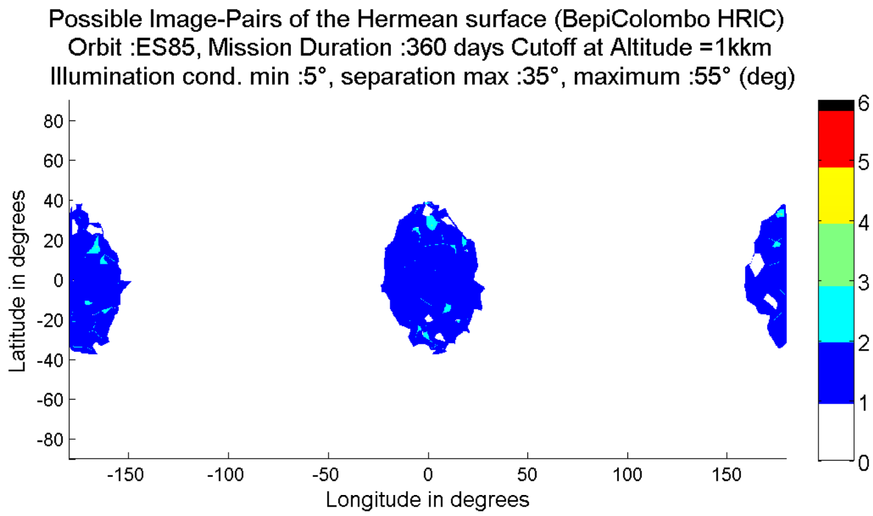

Figure 4.19: Distribution of surface regions which are observable at least twice and from which at least one image comparison can be constructed over a nominal mission of 360 days, for the $\beta = 20°$ "ES85" scenario. The colour scale represents the number of such image comparisons which are possible. The observations have been filtered according to an altitude constraint **excluding all observations made above 1000 km in altitude** and an illumination constraint excluding all low solar elevations (below 35°), very high solar elevations (above 85°) and imposing that inside an image-pair the illumination angle difference cannot be greater than 35°.

We construct an orbit closely resembling the final orbit the NASA MESSENGER mission will have upon arrival in Mercury orbit in 2011. Launched in 2005 towards Mercury the MESSENGER mission has made several Moon, Earth and Venus fly-by's in order to reach an orbit with characteristics presented in table (3.3) or (4.2) hereunder.

semi-major axis a	10136 km
periherm	450 km
apoherm	15193 km
eccentricity e	0.7158
inclination i	80°
argument of periherm ω_0	16°
longitude of ascending node Ω_0	67°

Table 4.2: MESSENGER type orbit

From fig. (4.21) it can be seen that a MESSENGER type orbit does not provide significant image-pair coverage below 1000 km over 720 days.

In the case where we do not restrain the observation altitude we observe a similar decrease of the image-pairs to two longitudinal zones than for the nominal BepiColombo orbit with the reduced altitude. We know from this that almost all image-pairs satisfying our observation criteria contain at least one image taken at altitudes higher than 1000 km. This is not surprising as MESSENGER spends most of its 12h orbit above 1000 km, with an apocenter at 15193km. At such altitudes the images cover an important part of the planetary surface and cannot qualify as *high resolution* images for our purposes.

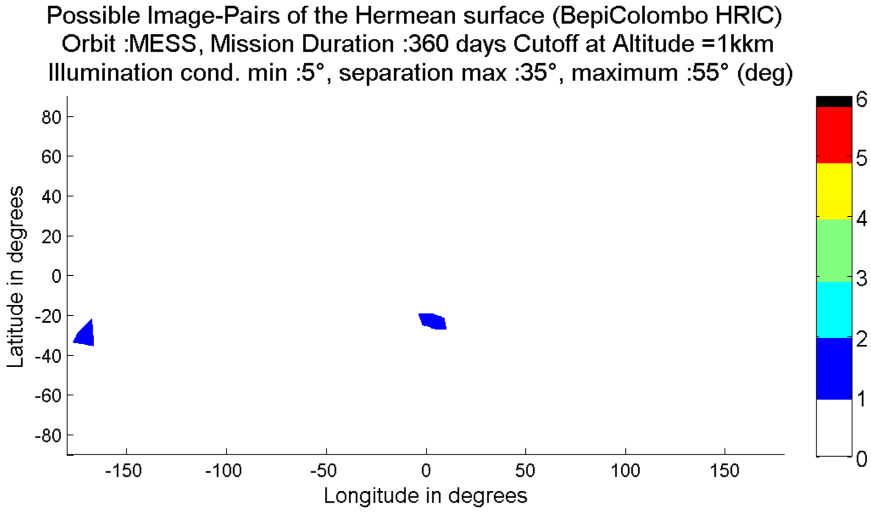

Figure 4.20: Distribution of surface regions which are observable at least twice and from which at least one image comparison can be constructed over a mission of 360 days, **for the MESSENGER type orbit scenario**. The colour scale represents the number of such image comparisons which are possible. The observations have been filtered according to an altitude constraint excluding all observations made above 1000 km in altitude and an illumination constraint excluding all low solar elevations (below 35°), very high solar elevations (above 85°) and imposing that inside an image-pair the illumination angle difference cannot be greater than 35°.

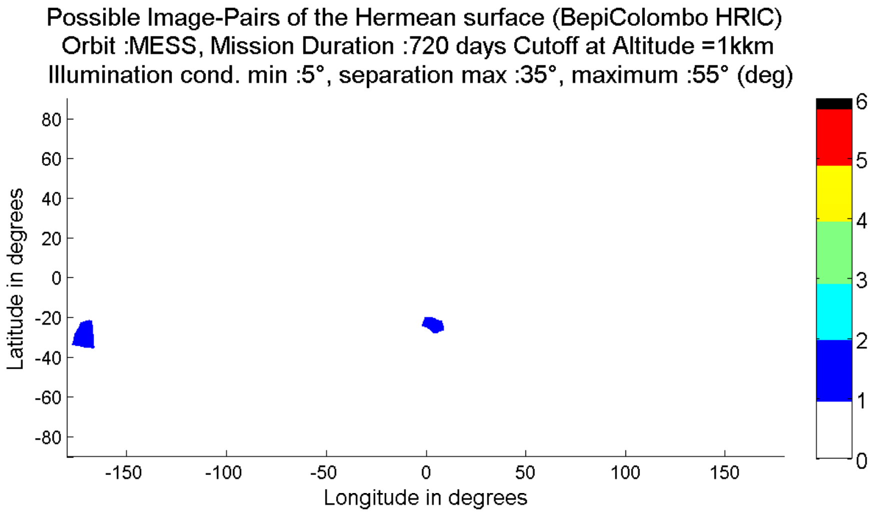

Figure 4.21: Distribution of surface regions which are observable at least twice and from which at least one image comparison can be constructed over a mission of 720 days, for the MESSENGER type orbit scenario. The colour scale represents the number of such image comparisons which are possible. The observations have been filtered according to an altitude constraint **excluding all observations made above 1000 km in altitude** and an illumination constraint excluding all low solar elevations (below 35°), very high solar elevations (above 85°) and imposing that inside an image-pair the illumination angle difference cannot be greater than 35°.

Chapter 5

Results: Parameter Estimation

Contents

In this chapter we investigate the quality of the estimation of the studied parameters (libration amplitudes and obliquity) for the nominal BepiColombo MPO orbit and its ESA studied alternates in order to establish the feasibility of the rotation experiment at the desired precision level. Additionally we will present the main results obtained for some interesting variations of the nominal orbit (introduced in chapter 4).

5.1 Required precision level

What level of error on the obliquity and libration amplitudes is acceptable if we are to reach the BepiColombo rotation experiment mission objectives? The targeted precision for the $\frac{C_m}{C}$ and $\frac{C}{MR^2}$ ratios stated in the BepiColombo mission goals (see *Milani et al.* 2001) is $\Delta(\frac{C_m}{C}) < 10\%$ and $\Delta(\frac{C}{MR^2}) < 1\%$ which corresponds to $\Delta(\frac{C_m}{C}) < 0.05$ and $\Delta(\frac{C}{MR^2}) < 0.003$ if we consider the expected values of $\frac{C_m}{C} \cong 0.5$ and $0.325 < \frac{C}{MR^2} < 0.37$ respectively. How does this translate into a limit on the parameters measured in this experiment? Using the following relations defined earlier (see eq.(2.44) and eq.(2.43)).

$$
\begin{aligned}
\frac{C}{MR^2} &= \frac{n\left[-C_{20}(1-e^2)^{-\frac{3}{2}} + 2C_{22}(\frac{7}{2}e - \frac{123}{16}e^3)\right]}{\mu(\frac{\sin I}{\eta} - \cos I)} && (5.1)\\
\frac{C_m}{C} &= \frac{C_m}{B-A}\frac{B-A}{MR^2}\frac{MR^2}{C} && (5.2)\\
\gamma &= \frac{3}{2}\frac{B-A}{C_m}\left(1 - 11e^2 + \frac{959}{48}e^4 + \ldots\right) && (5.3)
\end{aligned}
$$

we can not only relate the errors on the planetary parameters C_{20}, C_{22}, η, γ, to the resulting estimation of $\frac{C}{MR^2}$ and $\frac{C_m}{C}$ but also express upper precision limits on the estimation of the rotation and orientation parameters posed by the mission requirements. Considering the fact that the degree 2 coefficients of the gravitational field will be known with a very high precision of around 0.01% (*Milani et al.* 2001), the dominating factor limiting the precise determination of both quantities is the knowledge on the obliquity and libration amplitude value. Transforming the equations in (5.3) to isolate our parameters η and γ we get:

$$
\eta = \frac{\sin I}{\cos I + \frac{n}{\mu}\frac{MR^2}{C}\left[\frac{-C_{20}}{(1-e^2)^{\frac{3}{2}}} + 2C_{22}\left(\frac{7}{2}e - \frac{123}{16}e^3\right)\right]}\,, \tag{5.4}
$$

$$
\gamma = \frac{3}{2}\frac{C}{C_m}\left(1 - 11e^2 + \frac{959}{48}e^4 + \ldots\right)\frac{B-A}{MR^2}\frac{MR^2}{C}\,. \tag{5.5}
$$

Using the two equations above we can derive expressions for the upper error limits on both obliquity and annual libration amplitude that guarantee a successful experiment. We consider Mercury's orbital eccentricity e and Mercury's orbital plane inclination with respect to the Laplace plane I as error-free known quantities. Since the errors on the gravitational spherical harmonic coefficients C_{20} and C_{22} are expected to be negligible with respect to the errors on the obliquity and libration amplitudes (*Milani et al.* 2001), the latter can be expressed in terms of errors on C/MR^2 and C_m/C as:

$$
\Delta\eta = \eta\Delta\left(\frac{C}{MR^2}\right)\frac{MR^2}{C}\,, \tag{5.6}
$$

$$
\Delta\gamma = \gamma\left[\Delta(\frac{C_m}{C})\frac{C}{C_m} - \frac{\Delta\eta}{\eta}\right]. \tag{5.7}
$$

Rivoldini et al. (2009) have calculated interior structure models of Mercury for several plausible chemical compositions of the core and the mantle. For all models they have computed the associated C/MR^2 and C_m/C values and thereby constrained their plausible value to the following intervals:

$$
0.325 \leq \frac{C}{MR^2} \leq 0.37\,, \quad 0.3 \leq \frac{C_m}{C} \leq 0.6\,. \tag{5.8}
$$

Using these together with the current best estimates for γ and η by *Margot et al.* (2007b):

$$\eta = 2.11 \pm 0.1\text{arcmin}\,, \quad \gamma = 35.8 \pm 2\text{arcsec}, \tag{5.9}$$

yields the following worst case estimate:

$$\begin{aligned} \Delta\eta &\leq 1.0\text{as} \\ \Delta\gamma &\leq 3.1\text{as}. \end{aligned} \tag{5.10}$$

The current best estimate by *Margot et al.* (2007b) on both these parameters is $\sigma_\gamma = 2$as and $\sigma_\eta = 6$as, which is better than the minimum requirement for the libration amplitude and of the same order of magnitude for the obliquity value. It is to be expected that with the time series of radar observations by *Margot et al.* (2007b) growing longer every year the minimum level of precision on the obliquity will eventually be reached before the BepiColombo MPO arrives in orbit around Mercury. Fortunately for us, long period planetary induced librations will remain out of reach for Earth-based measurements, because they measure the planet's spin rate variations. Long period librations cause very small instantaneous spin variations whereas the spatial amplitude they generate may be big enough for a space based mission to observe. Increasing the precision requirement on $\frac{C_m}{C}$ to 5% instead of 10% increases the expected precision level on the libration amplitude to $\gamma \leq 1.4$ *arcsec* (keeping the maximum error constraint on the obliquity identical).

5.2 Parameter estimation: The nominal case

One of the aims of this work is to quantify the impact of the BepiColombo Mercury Planet Orbiter (MPO) mission configuration and planning on the outcome of the rotation experiment. To this aim we compare the restitution of the four parameters of interest[1] for different sets of mission *designs/scenarios* (as done for the surface observation maps in the previous chapter), however, one exception will be made: only the most restrictive observation constraints corresponding to the nominal ESA scenario previously discussed (see §4.2) will be studied. It makes no sense to study more than just slightly relaxed illumination conditions because we know that no effective image correlation can take place if the respective image illumination angles of the to-be-paired images are differing too much or if the individual images are taken when the Sun is low in the local sky. We do however study the impact of different mission durations, true anomaly exclusion zones and altitude limits.

In our analysis we will study the simultaneous restitution of parameters considered as independent. This means that we do not impose fixed relations between the different libration amplitudes, but allow each one to be solved

[1] obliquity, annual libration and two principal planetary librations

separately without any constraint. In chapter 2 we have shown how all librations are based on the same mechanism. We showed that all librations are caused by solar torques resulting from the interactions of the Sun with the planet, and that to a first approximation this can be reduced to torques acting on the equatorial bulge. Hence, all these librations exhibit fixed ratios between their respective amplitudes depending only on the value of α (which can itself be expressed as a function of the period of the free libration $(2\alpha G_{201})^{1/2}$, (see eq. (2.35)). The *closeness* between each libration frequency and the free libration frequency will determine the amplification of the associated libration amplitude.

In our simulations we do not consider the three libration amplitudes as fixed with respect to each other through fixed ratios (corresponding to fixing the free libration frequency to one particular value), not reducing the number of solved parameters to two (the obliquity and annual libration amplitude only). Doing so would enable us to study how critical it is to correctly model long period librations (especially the large amplitude Jupiter induced one) to guarantee an accurate determination of the annual libration amplitude.

The error bars on the low level gravity field coefficients of Mercury are currently very big (around 50%) causing the free libration period to be very badly constrained. As a consequence the Jupiter libration amplitude is very badly constrained as its period is expected to be very close to the free libration period (11.86 years vs. ~12 years). Due to the expected proximity of the free libration period (~12 years) to the the 11.86 years the amplitude of the *Jupiter libration*, $\gamma_{♃}$ will be heavily amplified (*Dufey et al.* 2009; *Peale et al.* 2009). Unfortunately the free libration frequency is currently not precisely constrained enough so that a small change in it will cause a big change in the Jupiter induced libration amplitude (highly non-linear, (see *Peale et al.* 2009; *Yseboodt et al.* 2009)). Therefore we can already conclude that we cannot consider a Mercury rotation model in which the Jupiter libration is added as a fixed ratio term to the annual libration without exposing ourselves to serious estimation errors.

To enable a good understanding of the quality or lack of quality of the parameter restitution process we will analyse the data in different forms. Both accuracy and formal error will be plotted as a function of time or number of observed image-pairs or number of observed targets for each parameter. The results will be presented for different mission parameter values, such as different altitude limits, different mission duration, different true anomaly exclusion windows or different observed target numbers. As a lot of different quantities have the potential to impact our experiments outcome significantly many different combinations of the above cited graphic representations will be explored to better visualise and separate their individual effect. We will not include the graphs representing the accuracy / true error in every case, because in none of the cases presented they add significant information. Simply put, the value of the true error on the estimated parameters[2] never significantly

[2]The absolute value of the shift between the parameter value used for the simulation and the value retrieved.

exceeds twice the value of the formal error associated with it. We can say that the *estimated parameter* stays inside a 2-σ region around the *a-priori* parameter value used. This means that the estimated parameter is not affected by an experimental bias. As the least squares method is a *biased estimator* this cannot be guaranteed upfront and has to be verified through simulations, which is what has been done in this work.

5.2.1 Nominal mission

We start with the nominal mission parameters (ESAS) as defined in table (3.3) and consider nominal illumination conditions as described in §4.2.2. In fig.5.1 we present the formal error on each parameter as a function of the number of targets observed over a 360 day mission. Up to four coloured curves can be seen on every graph, each representing a different value of maximum altitude restriction on the observations used. The black line represents the previously defined maximum allowable error level to fulfil the minimal mission requirements. The altitude restriction and its rationale have been discussed in the previous chapter (see §4.2.3). Only if no altitude limit is imposed on the images used in the least squares inversion does the experiment reach *low* formal errors for the restituted obliquity and planetary induced libration amplitude value after 360 mission days (see fig.5.1). The causes of this will be discussed in the next paragraph. First let us discuss other characteristics of these results. Since the formal error depends on the number of observations, adding more observations (=image-pairs) will reduce the formal error on each parameter. Beyond a certain number of image-pairs the gain in formal error is entirely attributable to the very important data volume ($\sigma \sim \frac{1}{\sqrt{N}}$) and not to additional information, resulting in a linear decrease of σ values in a log-log plot. This is only true if the error on the data is Gaussian, which we consider it to be. In figure (5.2), where the true error is represented for the same studied scenario, it can be seen that the accuracy levels or true error levels on the retrieved parameters oscillate around a constant level after images pairs from around 100 different targets have been observed repeatedly. This information can be used to determine the sweet spot in observations and target numbers needed to achieve a good result while keeping the data volume to a minimum (because dedicated imaging opportunities will be limited), and can serve as a measure of the cost of additional observation in contrast to the gains obtained. From figures (5.1) and (5.2) we can conclude that our solution is not affected by experimental bias, as the least squares approach used delivers true errors on the parameters that are smaller or equal to the formal error (except for some very low data volume configurations). If we concentrate on the libration amplitudes we see that when data is restricted to altitudes lower than 1000km there is almost no difference in the results for the three different altitude limits. To investigate this we considered the number of image-pairs used for the solution limited to 100 observed targets. It appears that the *same* number of observations (119 image-pairs) is used for all three altitude limited scenarios, while 384 image-pairs contribute to the *unlimited* case. This is because all images

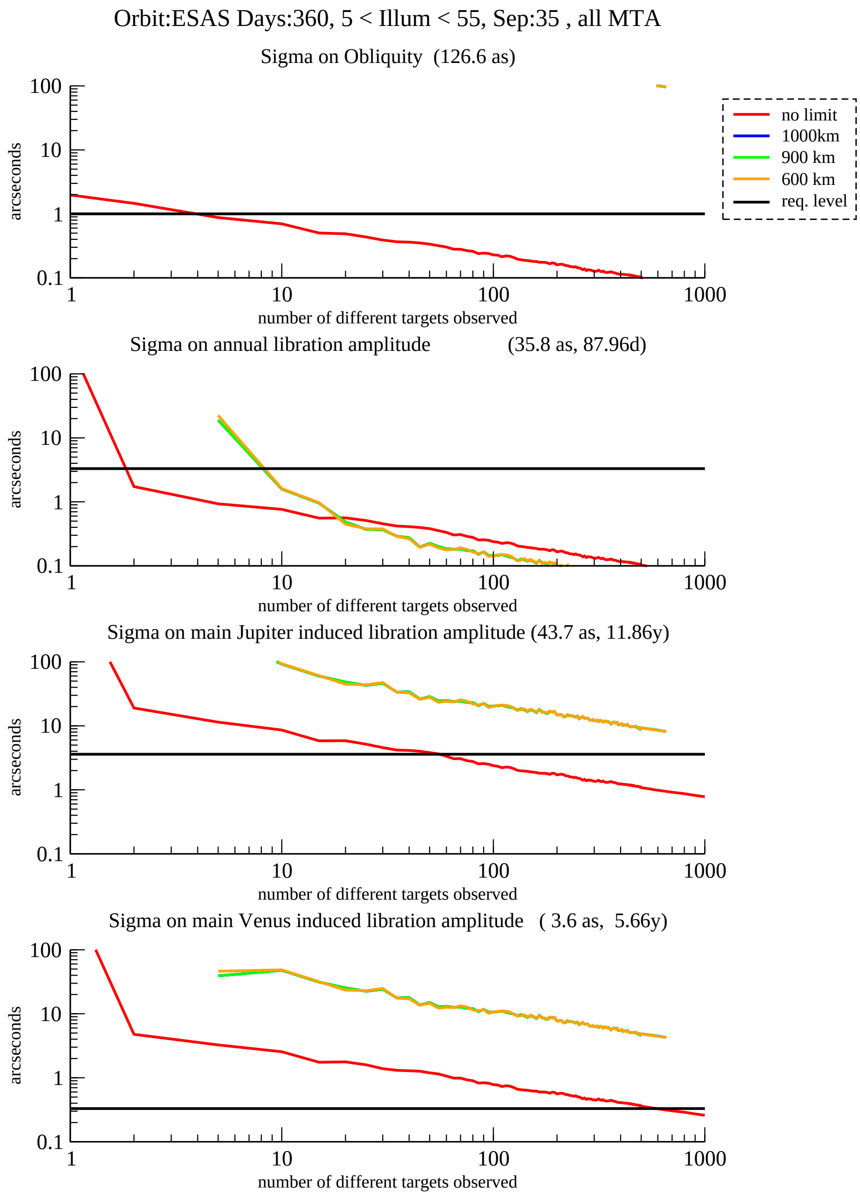

Figure 5.1: From top to bottom the **formal error (**1σ**)** on the four parameters we solve for a 360 day mission: obliquity, annual libration amplitude, Jupiter induced libration amplitude and Venus induced libration amplitude. The black curve represents the error level required for a successful experiment. The red curve represents the *unlimited* scenario where images are not filtered based on the altitude from which they were taken. The maximum altitude reached by the BC MPO for the ESAS orbit is 1508 km. The blue, green and orange curves represent altitude limits of respectively 1000 km, 900 km and 600 km on the observations used.

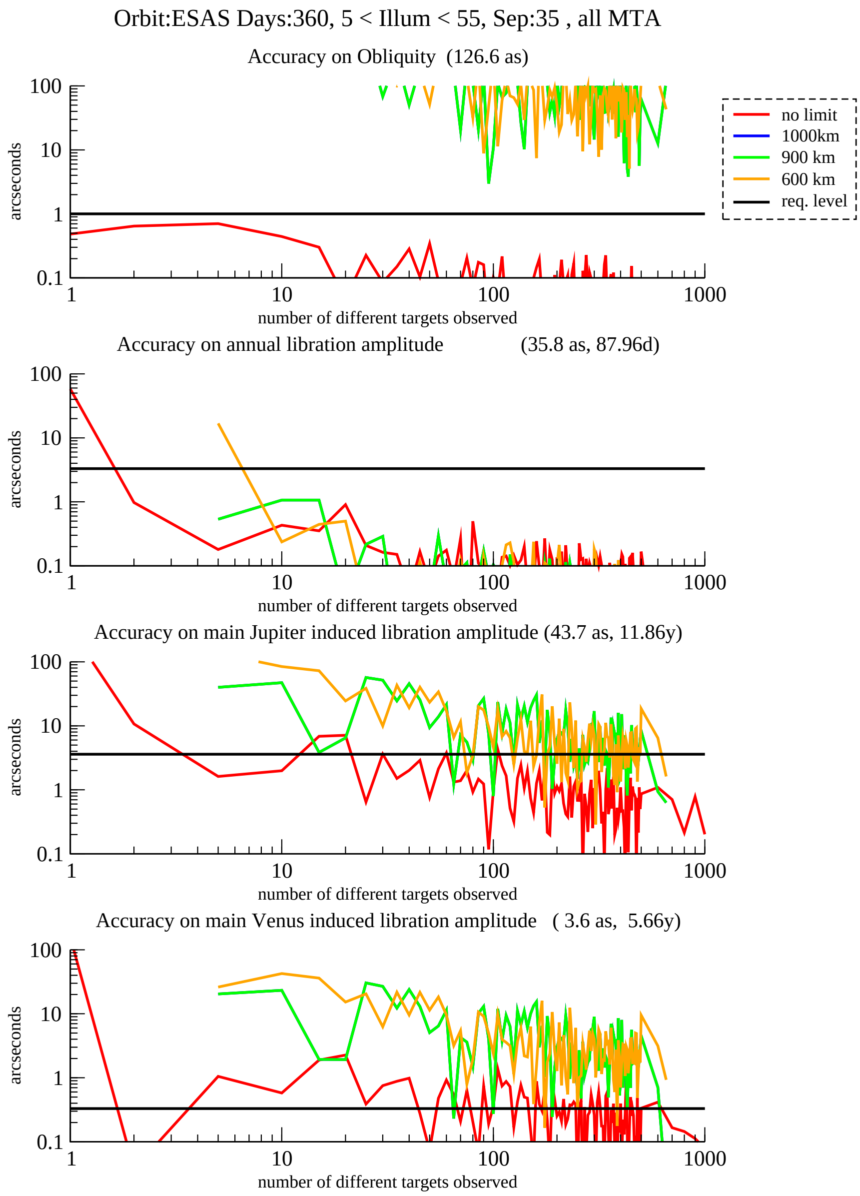

Figure 5.2: From top to bottom the **true error** on the four parameters we solve for a 360 day mission for the nominal ESAS orbit: obliquity, annual libration amplitude, Jupiter induced libration amplitude and Venus induced libration amplitude. The black curve represents the error level required for a successful experiment. The red curve represents the *unlimited* scenario where images are not filtered based on the altitude from which they were taken. The maximum altitude reached by the BC MPO for the ESAS orbit is 1508 km. The blue, green and orange curves represent altitude limits of respectively 1000 km, 900 km and 600 km on the observations used.

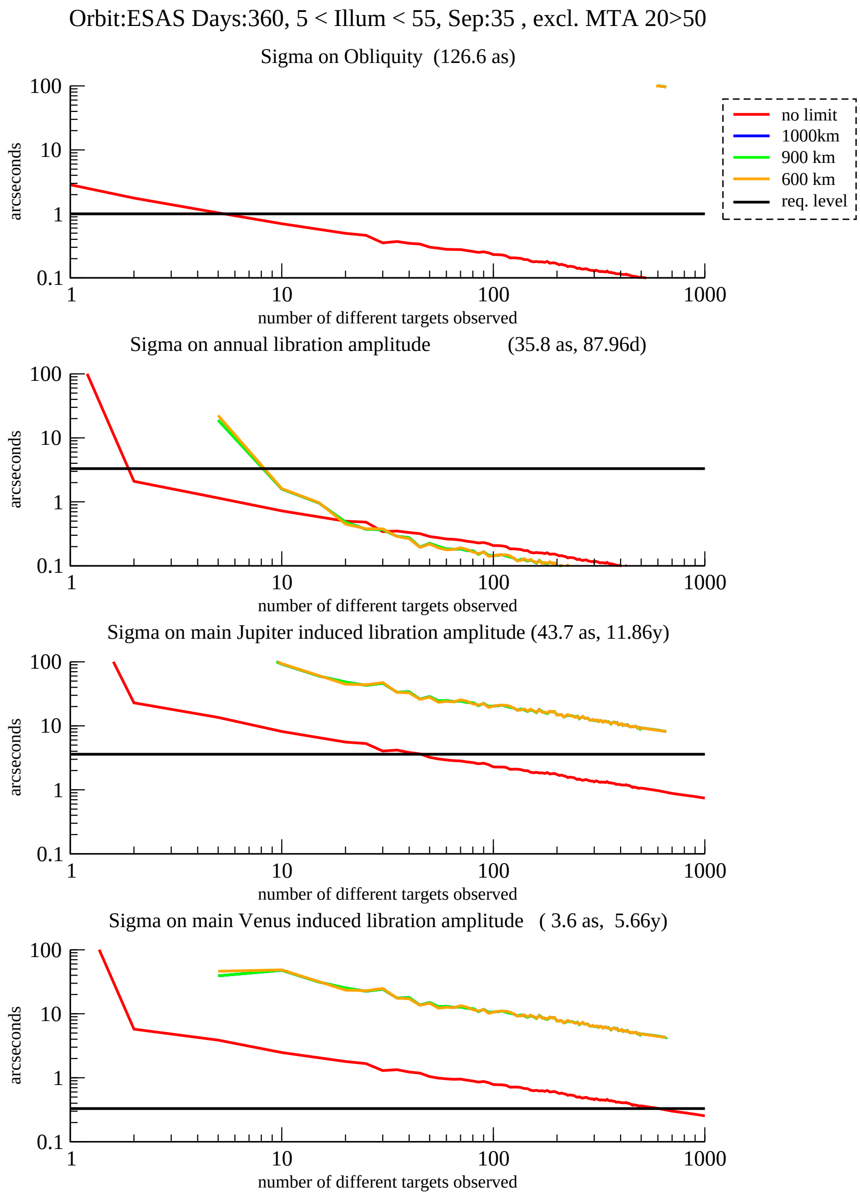

Figure 5.3: From top to bottom the **formal error (**1σ**)** on the four parameters we solve for a 360 day mission for the nominal ESAS orbit. Each plot contains four lines representing each a different upper altitude limit on the observations used in the results. The black curve represents the error level required for a successful experiment. The red curve represents the *unlimited* scenario where images are not filtered based on the altitude from which they were taken. The blue, green and orange curves represent altitude limits of respectively 1000 km, 900 km and 600 km on the observations used.

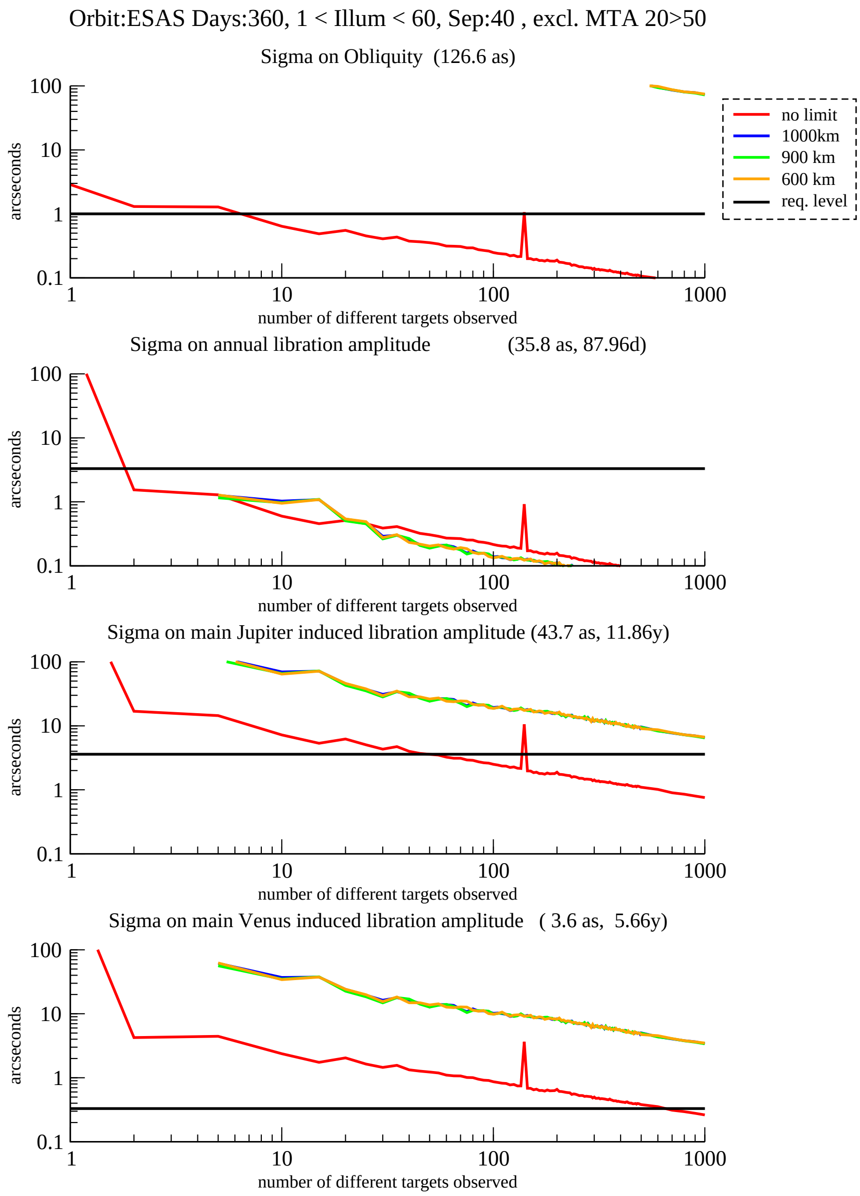

Figure 5.4: From top to bottom the **formal error** (1σ) on the four parameters we solve for a 360 day mission **for slightly relaxed illumination conditions**. Each plot contains four lines representing each a different upper altitude limit on the observations used in the results. The black curve represents the error level required for a successful experiment. The red curve represents the *unlimited* scenario where images are not filtered based on the altitude from which they were taken. The blue, green and orange curves represent altitude limits of respectively 1000 km, 900 km and 600 km on the observations used.

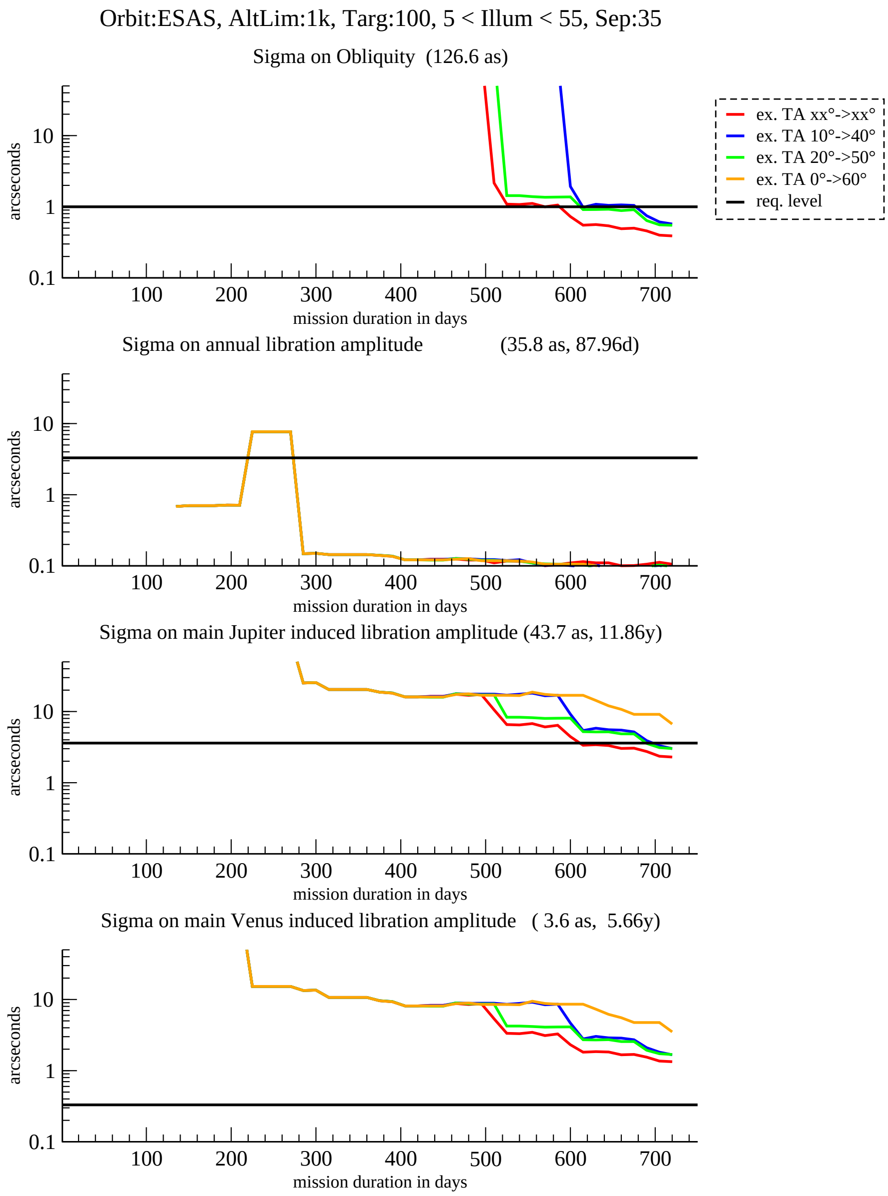

Figure 5.5: From top to bottom the **formal error (1σ)** on the four parameters we solve for a 360 day mission Each plot contains four lines representing each a **different Mercury true anomaly exclusion zone** on the observations used in the results. The black curve represents the error level required for a successful experiment. The red curve represents the *unlimited* scenario where images are not filtered based on the altitude from which they were taken. The blue, green and orange curves represent altitude limits of respectively 1000 km, 900 km and 600 km on the observations used.

taken below 1000km of altitude respecting all nominal mission constraints are also taken below 600km of altitude for a 360 day mission limited to 100 targets on the planetary surface. A comparison can be drawn between this situation and the situation for the distribution of surface observations seen in fig. (4.5) where the surface patches repeatedly observed are located at latitudes, longitudes and observation times that are corresponding to flyovers at low altitudes. These results show that the very low altitude measurements (below 600km) made at quasi-equatorial latitudes bear the most signal and weight in the final solution for the annual libration determination. Adding data taken above 1000km in altitude does not improve the error on the annual libration amplitude.

The formal error values on the two planetary induced libration amplitudes and the obliquity decrease with increasing altitude limit[3] (see fig. (5.3)) but stay well above the minimum mission requirement. The more the measurements are restricted in altitude (reducing the data volume) the less well they are resolved. This can be seen in the same figure (5.3) except for the libration amplitude, which is best determined if observations are restricted to lower altitudes. This difference is due to the following two facts: The annual libration signal is strongest in the equatorial regions as it is a longitudinal signal, and the periherm of the MPO orbit is located close to the equator creating the possibility of very strong-signal image pairs. If we allow images taken at higher altitudes we add image-pairs of lower resolution spread over a wider latitude domain. We have not weighted the observations as a function of the latitude or altitude or any other characteristic (because this would have skewed the results of the other three parameters while favouring this one). This degrades the total solution by adding more observations with lower signal to noise ratio, thereby diluting the signal coming from high signal to noise image-pairs taken at low altitudes. The solution therefore gets *noisier*. We don't see this for the other three parameters, partly because of their smaller signal in the observable and the long period for the two librations or to the Mercury solar longitude dependence in the case of the obliquity. For a small amplitude long period signal such as the long period planetary librations, the observation time series has to be long enough to cover a significant part of the cycle so that the cycle can be determined accurately. The two *minor* librations and obliquity are very badly estimated in all three altitude limited cases as the associated true errors reach levels close to 100% error for the obliquity and the Venus libration amplitude and around 30% for the Jupiter libration, as can be seen in fig. (5.1).

In figure (5.3) we represent the exact same situation as for figure (5.1) except for the addition of the nominal Mercury true anomaly (MTA) window[4]. The results are extremely similar hinting that the addition of this exclusion zone does not degrade the parameter estimation process in conjunction with the other nominal mission constraints. In the most part of this chapter we will systematically apply the nominal MTA window as this adds an additional constraint

[3] By increasing altitude limit I mean higher altitude limits.

[4] Between 20 to 50 and 310 to 340 degrees of true anomaly.

to the successful estimation of the rotation and orientation parameters. The main idea is that if it works with this additional constraint it will work without, because all observations constrained by a MTA window are automatically part of the wider group of observations without a MTA window.

In this ESAS nominal mission case the minimum precision levels are reached for 10 image-pairs after 360 days for the libration amplitude, but not for the obliquity as can be seen in the previously discussed fig. (5.3)[5] . The required precision level on the obliquity is only reached after $\sim$ 600 mission days for the nominal 1000km altitude limit (see fig. (5.8(a))).

Comparing simulations over a longer time than the nominal 360 days of 720 days we can see in fig. (5.6) and fig. (5.3) the significant difference a longer mission duration has on the restitution of almost all the parameters can be seen. The largest difference is observed in the case of the altitude limited restitution for the obliquity and to a lesser extent for the low altitude limited restitution for the libration amplitudes. All parameters except the Venus induced libration amplitude can be solved for with a formal error smaller than the minimum mission requirement (as defined above) with about 50 image-pairs after 720 mission days. Mission durations longer than the nominal 360 days studied here do not take into account possible orbital manoeuvres due to evolving mission goals for a potential extended mission. We simply allow the orbit to evolve purely due to the secular and periodic effects due to the low degree harmonics of the gravitational field of Mercury without any intervention to change the spacecraft orbital elements. As a consequence, the spacecraft periherm will drift by about 33° per year in the direction of the South Pole of the planet. After 720 mission days it will be located at a latitude of around $-50°$ in the southern hemisphere. A quick glance at table (3.3) shows that the initial periherm for this orbit was situated at a latitude of 16° North [6].

For an identical number of image pairs of about 30 (see fig.5.6) we have comparable errors for the altitude unlimited dataset and 1000km limited set after 720 mission days, all below the minimum mission requirements. This is not the case for a nominal mission duration of 360 days (fig.5.3), where none of the altitude restricted scenarios reach the minimum precision requirement. The logical conclusion from this is that a longer mission duration yields image-pairs with more signal from the parameters, as we get better results with the **same** number of observations! This can be understood in the following way: the orbital evolution of the spacecraft allows it to observe higher *latitudes* at lower a*altitudes*. Therefore longitudes previously flown over at high altitudes can then be imaged from altitudes lower than 1000 km due to the periherm drift [7]. If we look closely at figure (5.6) we can see a large difference in error on the obliquity for a seemingly small difference in upper altitude limitation of 100km, between 1000km and 900km. Does this fact confirm that high latitude

[5] The nominal mission case limits all observations to altitudes lower than 1000km.

[6] The periherm latitude of 16° corresponds to a description of the periherm on the part of the orbit opposite the ascending node. The spacecraft thus reaches its periherm close to the point where it will cross the equator from North to South (descending) at a latitude of 16° North.

[7] The periherm drift rate for the ESAS nominal orbit is of $\sim -33°$ per year (see table (3.3)).

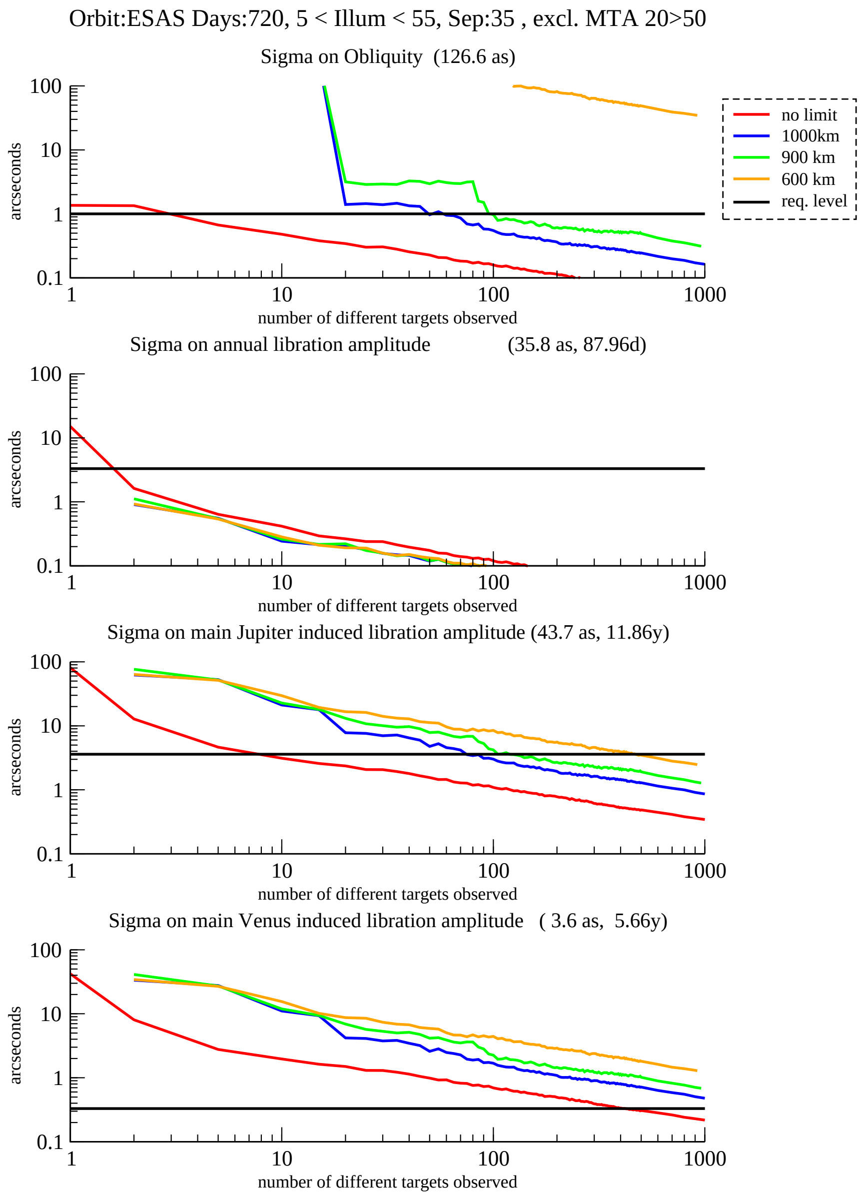

Figure 5.6: From top to bottom the **formal error (1σ)** on the four parameters we solve for a **720 day** mission with the **ESAS** orbit: obliquity, annual libration amplitude, Jupiter induced libration amplitude and Venus induced libration amplitude. The black curve represents the error level required for a successful experiment. The red curve represents the *unlimited* scenario where images are not filtered based on the altitude from which they were taken. The blue, green and orange curves represent altitude limits of respectively 1000 km, 900 km and 600 km on the observations used.

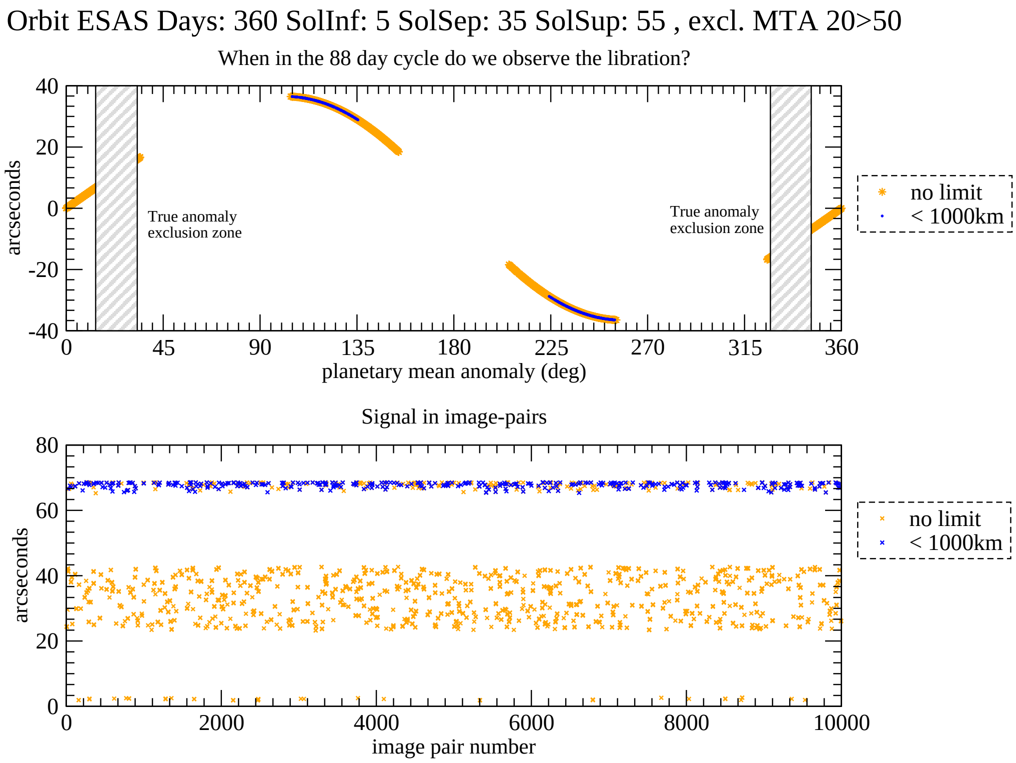

Figure 5.7: The upper graph shows the temporal distribution of observed image-pairs. The blue dots correspond to image-pairs involving images made below 1000km in latitude. The orange dots represent the image-pairs involving at least one image made with an altitude greater than 1000 km. The second graph shows the annual libration phase difference *inside* image-pairs as a function of the image-pair number. The maximum libration displacement difference that can be obtained is twice the libration amplitude (peak to peak measurement). Blue and orange have the same significance as before. All image-pairs limited to 1000km in altitude exhibit a close to maximal phase difference.

image-pairs are critical in the obliquity determination or that the observation of certain longitudes enables high signal to noise image-pairs for this parameter? In the following paragraph we will show that the latter is true and corresponds to observations made at *low* altitude on the spacecraft's orbit aposide. After around 500 mission days the first images of the orbit *aposide* taken at altitudes lower than 1000km start to appear for latitudes close to 40°.

The combined figure (5.8) shows the formal error as a function of the mission duration for a fixed number of 100 observed targets for the nominal illumination constraints (a) and slightly relaxed illumination constraints (b). We can clearly see that in both cases the formal errors decrease with mission duration for the constant number of 100 targets observed, as the volume of image-pairs increases with time. For all parameters except the libration amplitude, the altitude restricted scenarios deliver worse results than the *unlimited* case. The difference in error levels between the different altitude limits is smallest in the case of the annual libration amplitude, which can be attributed to the fact that its signal is the most important of all surveyed parameters and the fact that low altitude observations are made close to the equator where the libration signal is strongest. For the 1000km-limited case a satisfying precision level below 1 arcsecond for the obliquity and 3 arcsecond for the annual libration is reached after 520 to 540 mission days for both sets of illumination constraints. This is longer than the nominal mission of 360 days. Increasing the number of targets / image-pairs will have no impact on this timing at all, as can bee seen in fig. (5.9) which for the exact same constraints as fig. (5.8(a)) plots the formal error as a function of the mission duration for different fixed target numbers (and a fixed upper altitude limit of 1000 km). This result tends to confirm that the altitude limits combined with the fairly restrictive imaging conditions are the underlying causes limiting the parameter resolution potential of this experiment as they do not permit the imaging of certain planetary longitudes important to the obliquity determination.

From both figures in fig. (5.8) it can be concluded that the two planetary librations are heavily dependent on the ability to solve for the obliquity as they experience a big improvement both in accuracy and formal error following the successful determination of the obliquity (after about 520 days). This is typical of a weak signal situation, in which the inability to correctly resolve the obliquity completely drowns out the signal of both planetary induced librations. We can now understand why the altitude restricted mission scenarios need more than 500 days to reach a similar precision level of the unrestricted scenario reached after only 100 days. Limiting the observations in altitude below 1000 km divides the observations windows by two, because it effectively rules out surface observations made while the MPO is on its *aposide*. Only after a long time (500 days) does the periherm node evolution shift the orbit enough to have low altitude measurements made of what used to be regions overflown with high altitudes.

From the perspective of the annual libration amplitude enough information is available after a nominal mission duration of 360 days to reach a *good* level

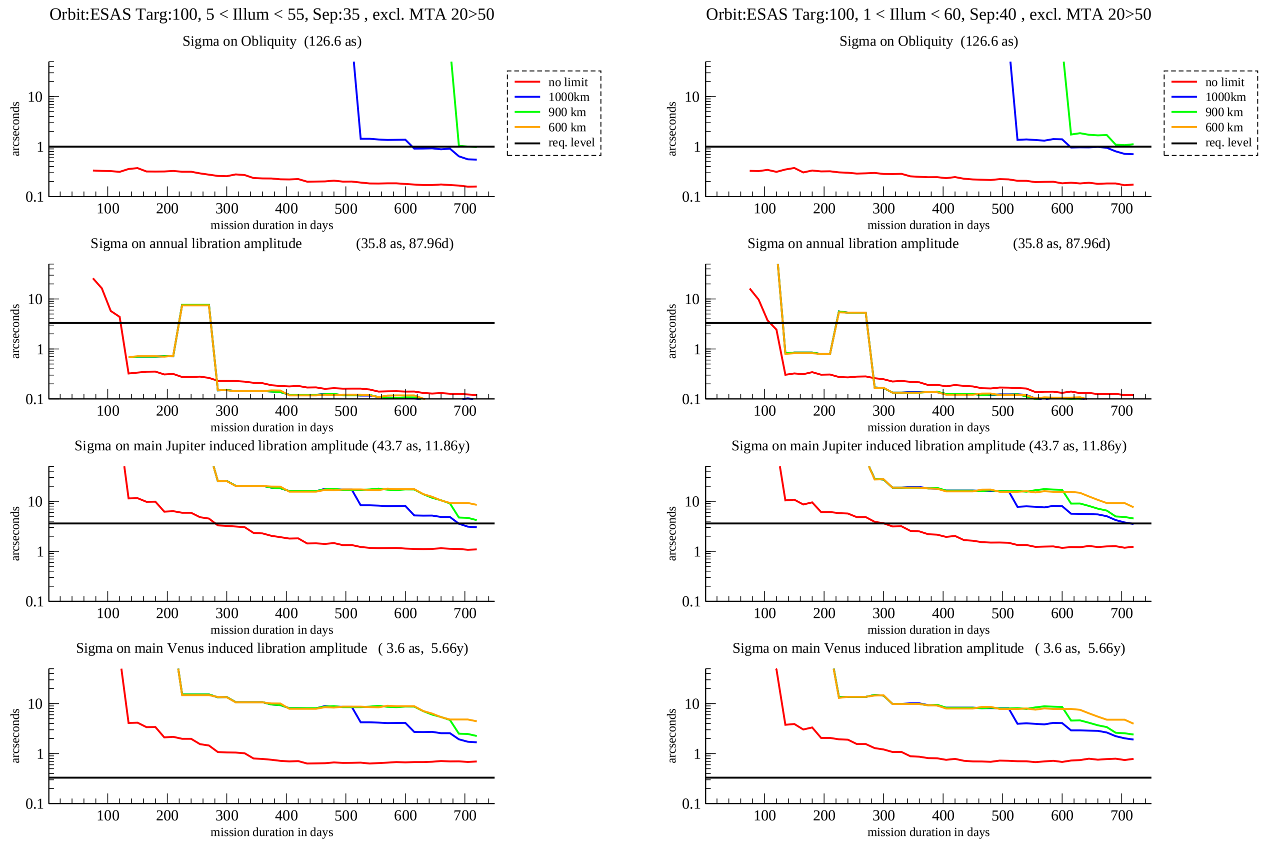

(a) Nominal illumination constraints

(b) Slightly relaxed illumination constraints

Figure 5.8: From top to bottom the **formal error (1σ)** on the four parameters we solve for a *fixed number of 100 targets as a function of the mission duration*. Each plot contains four lines representing each a different upper altitude limit on the observations used in the results. The black curve represents the error level required for a successful experiment. The blue, green and orange curve represent altitude limits of respectively 1000 km, 900 km and 600 km on the observations used.

of precision as defined by eq. (5.10), even for low altitude restricted mission scenarios (see fig. (5.3)). Looking at fig. (5.7) it can be seen that this is because a lot of *well distributed* observations are available in the nominal mission scenario. All of the image-pairs generated with images limited to 1000 km in altitude contribute close to the maximal libration signal of twice the libration amplitude. The images inside each image-pair correspond to epochs where the libration displacement is close to maximum and with opposite phases. For the other parameters two different requirements need to be fulfilled. In the case of the long period planetary librations a BepiColombo mission duration of 360 days represents only a small fraction of the whole 5.66year or 11.86year cycle for the studied Venus and Jupiter librations respectively. Clearly a longer observation period through a potentially extended mission will yield better estimates of their amplitudes. This means that for the purposes of the BepiColombo mission the longest possible mission survival will help for a better estimate. In the case of the obliquity estimation the problem is not so much mission duration as *mean anomaly coverage*, meaning that the obliquity signal is strongest for certain image comparisons made at certain planetary mean anomaly intervals (over one orbit of Mercury). As long as these observation *baselines* are not available no accurate obliquity determination seems to be possible through this experiment, as we have shown in the case of the low altitude restricted mission scenarios which cannot correctly estimate the obliquity before $\sim$ 540 mission days. We could say that analogously to what can be seen in fig. (5.7) for the distribution of the observations over the libration phase-space, in the case of the obliquity determination, altitude limited observations force the individual images to contain "'same phase"' obliquity signal data which cancels out inside all image pairs.

From figure (5.9) we can learn the importance of the number of targets surveyed in terms of gains on the formal error and accuracy on each of the four parameters. This figure presents the formal error on each of the four parameters solved and as a function of the mission duration, and each curve represents the solutions for a particular number of surveyed targets (25, 50, 100, 200). The absence of significant differences in the temporal evolution for any type of target number surveyed is a strong indication that the data volume is not the bottleneck of the experiment. The small decrease in formal errors when the target numbers increase is entirely due to the increase in data volume and the fact that the formal error is proportional to $\frac{1}{\sqrt{N}}$, where N is the number of image-pairs. A small number of targets can *do the job* as well as a large number. Nevertheless a big number of targets may be needed to reduce the error levels below the mission requirements. Unfortunately this increase in the number of surveyed targets will have to be quite extensive to gain only a small decrease in error.

To confirm that it is mission duration (and therefore the spatio-temporal distribution of the observations) that dominates the quality of the restitution we can plot the formal error as a function of the number of targets observed for a number of different mission durations for the nominal mission (altitude limited to 1000 km). This is done in figure (5.10) in which it can be seen that the formal

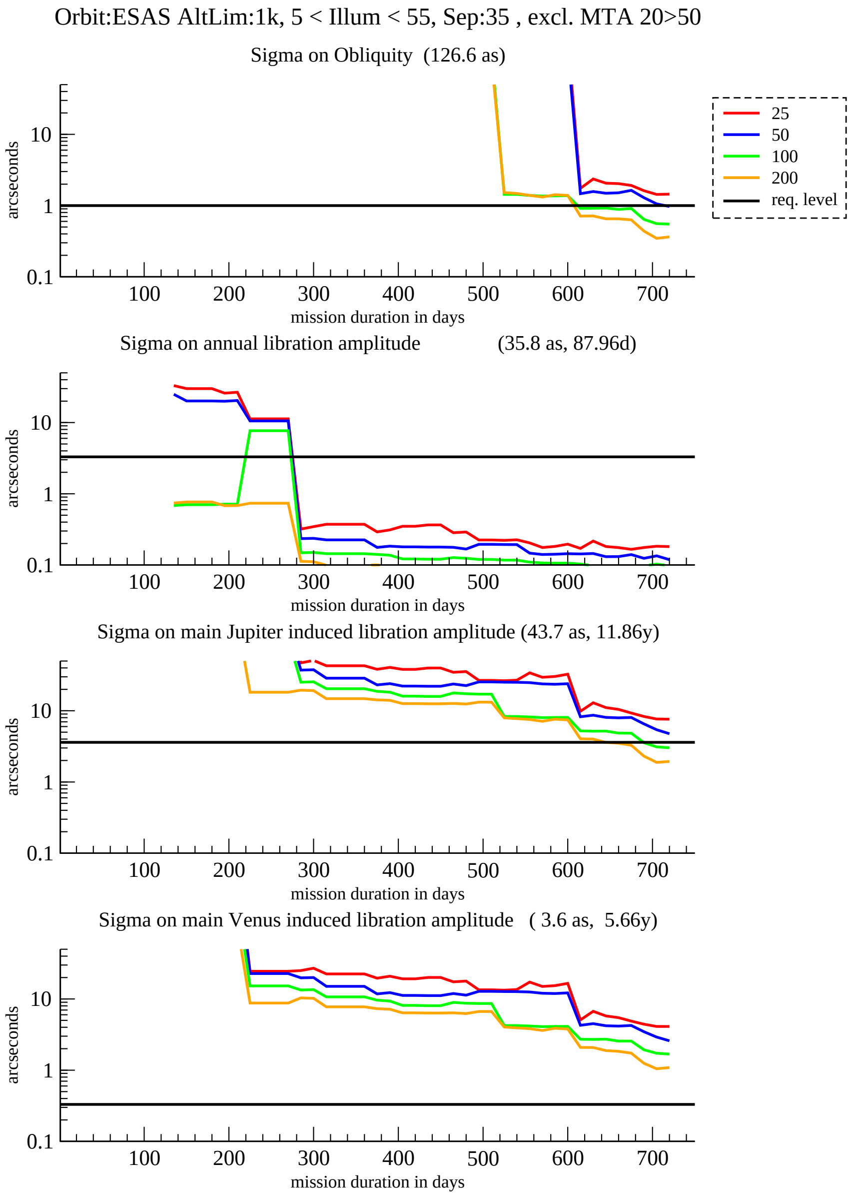

Figure 5.9: From top to bottom the **formal error (1σ)** on the four parameters we solve for a fixed altitude limit of 1000km as a function of the mission duration. Each plot contains four lines representing each a different number of targets used to obtain the solution. The black curve represents the error level required for a successful experiment. **The red, blue, green and orange curve represent 25,50,200 and 200 targets used respectively.**

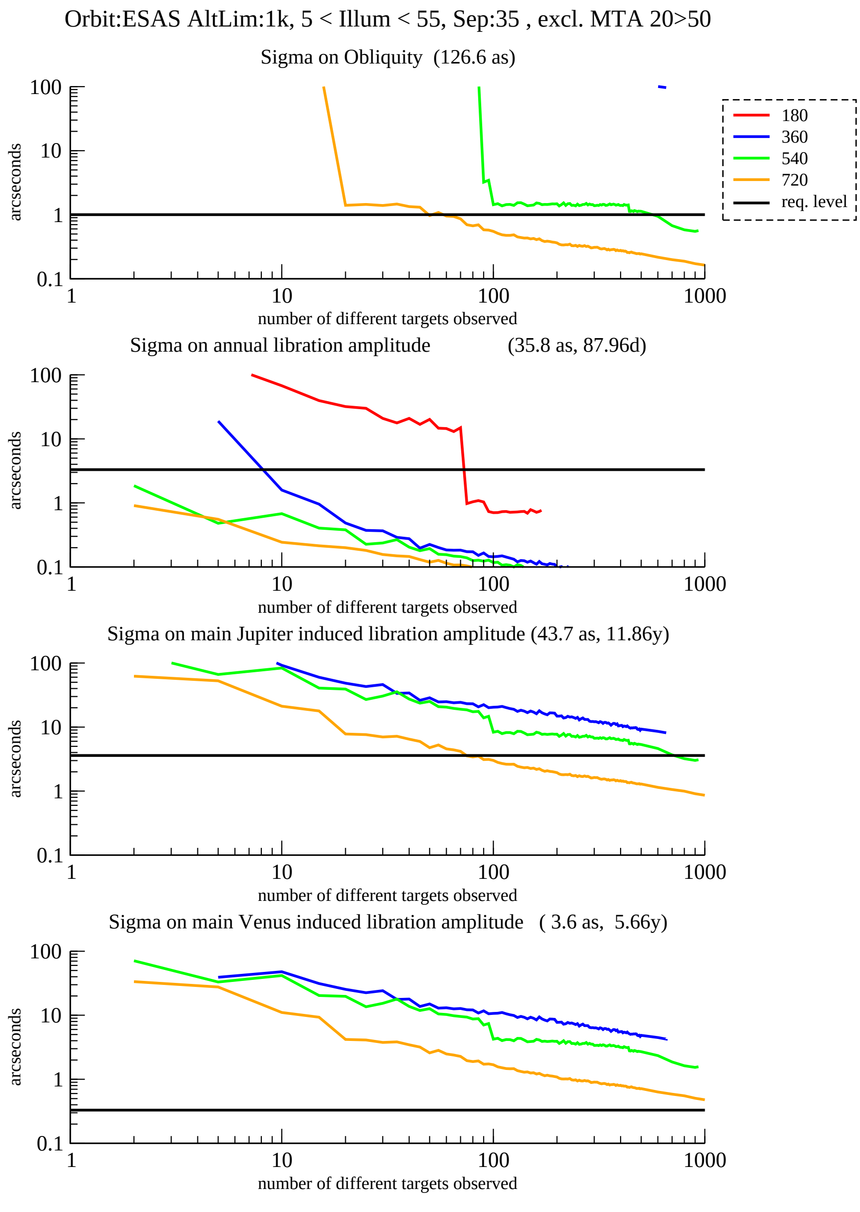

Figure 5.10: From top to bottom the **formal error** (1σ) on the four parameters we solve for a **fixed altitude limit of 1000km** as a function of the number of targets used to obtain the solution. Each plot contains four lines representing each a different mission duration. The black curve represents the error level required for a successful experiment. **The red, blue, green and orange curve represent mission durations of respectively 180,360,540 and 720 mission days.**

error levels are close to identical whatever the number of targets involved for any fixed mission duration (except for the very small target numbers below 10 or 15). The differences between the individual mission duration curves show how much this variable influences the outcome of the experiment. A big decrease in error can be seen between 180 and 360 mission days. It also appears impossible to obtain a solution for the obliquity under the nominal mission constraints under 540 days.

If we consider a scenario without altitude restrictions (see fig. (5.11)) we can see that the final result can be reached after 180 mission days already for the obliquity and annual libration amplitude, as all different observation windows will already have been *explored* after one Mercury day. The addition of longer time series will only benefit to the restitution of long period signals such as the Jupiter and Venus librations, and even in this case the only quality improvement to be seen is between 180 and 360 mission days.

Preliminary Conclusions

After having studied the nominal mission scenario a number of specific conclusions can already be reached:

- The main Jupiter and Venus induced libration amplitudes are best estimated for longer mission durations because of their long periods. As long as the obliquity is not well solved for, it is impossible to obtain accurate estimations of these two parameters.
- No accurate obliquity estimation is possible in 360 mission days if the observations are altitude limited below 1000 km.
- The annual libration amplitude is well solved for, in almost all circumstances reaching levels of around 1 arcsecond in true and formal error after less than 360 days and for data sets limited to 25 targets only.

The nominal mission scenario is not able to solve for the two *main* parameters during the nominal 360 day mission. This effect can be eliminated by including high altitude measurements (> 1000 km) of the surface made close to the Mercury perihelion passage, thereby *filling the gap* in the data hindering a good resolution of Mercury's obliquity.

5.2.2 High apoherm nominal orbit ESBS

This orbital scenario is in all points identical to the nominal ESA mission discussed above, except for the apoherm altitude which is elevated from 1508km to 2943km (see table (3.3) and §4.2.5). The change in orbital eccentricity will greatly reduce the number of observations made at low altitudes and the increase in orbital period (from 2.3h to 2.8h) will reduce the repeated surface

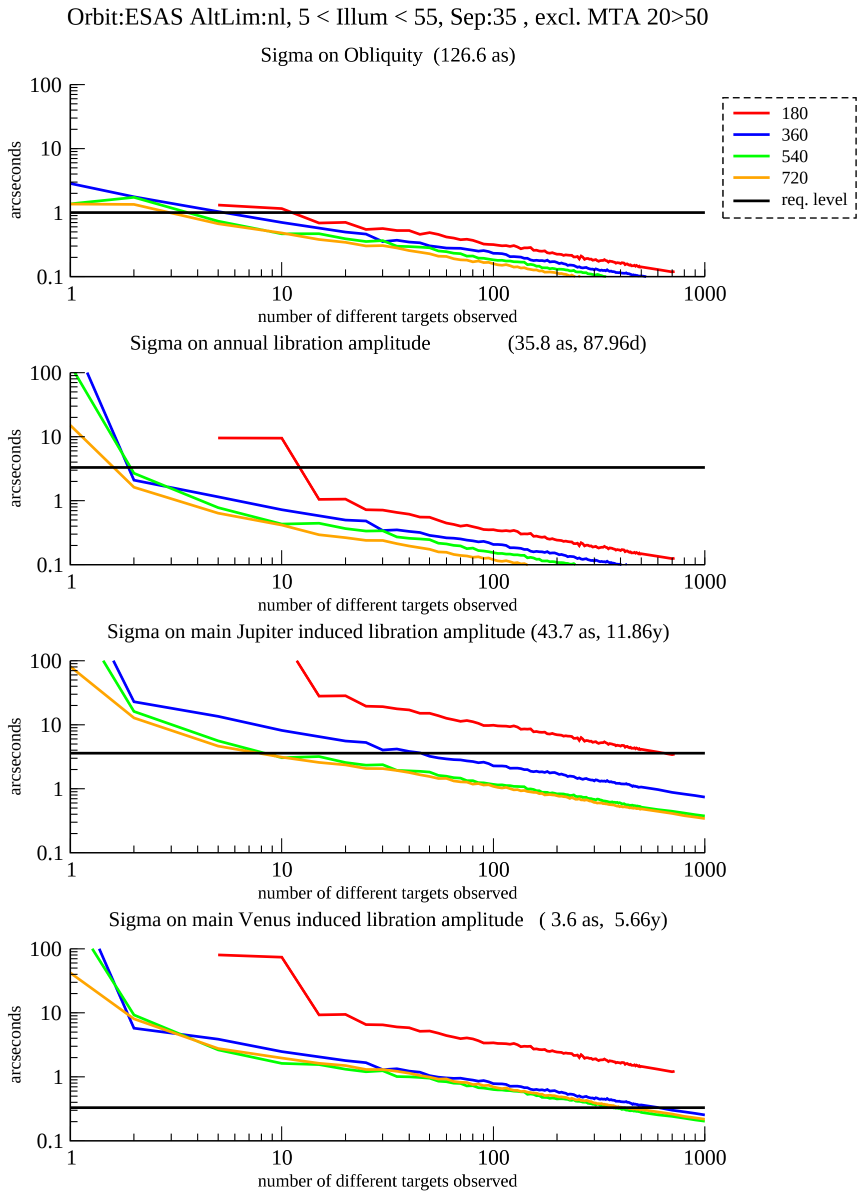

Figure 5.11: From top to bottom the **formal error** (1σ) on the four parameters we solve in an **unlimited altitude scenario** as a function of the number of targets used to obtain the solution. Each plot contains four lines representing each a different mission duration. The black curve represents the error level required for a successful experiment. The red, blue, green and orange curve represent mission durations of respectively 180,360,540 and 720 mission days.

coverage at low latitudes. The smaller number of orbits over a nominal mission due to this apoherm raise result in a reduction of the number of potential image-pairs. The main reason for this is that a longer orbital period leaves the planet more time to rotate under the non precessing polar MPO orbital plane. At equatorial latitudes this means that successive overflights of the same surface regions will be separated by ~ 30km instead of the ~ 23km for the ESAS nominal orbit. Low altitude images of the equatorial regions are made at around 400km of altitude, and are about 10km wide. High altitude images have a width of around 38km. The consequence is a coverage loss at low altitude, resulting in less image-pairs in general but especially if the mission is limited at low altitudes images only (for a complete discussion of the impact on the observation distribution and observation numbers see §4.2.5).

The apocenter rise has only a minimal impact on the altitude unlimited scenario (see figures (5.8(a)) and (5.12(a))). Even with the higher apocenter, all four parameters are estimated with an error of about 1 *arcsec* after one nominal mission duration in the altitude unlimited case. As seen for the ESAS orbit adding more observations through the inclusion of more targets into the dataset does not enhance our solution significantly (we can see a linear trend in the log-log plot in fig. (5.13)). The dominant factor limiting the resolving power of altitude restricted mission scenarios is the lack of observations around Mercury perihelion, which can be solved through either a longer mission (the secular periherm drift will slowly bring low altitudes to the apoherm side) or an orbit changing manoeuvre. In the case of the ESBS orbit no scenario limited to 1000km altitude or below can solve for the value of the obliquity even for mission durations reaching up to 720 days (twice the nominal mission duration). This is caused by the fact that no low altitude measurements of the orbital "*aposide*"[8] are possible even after a mission duration of 720 days because the secular periherm drift is about one third slower than for the nominal orbit[9]. The slower drift reduces the number of spatial configurations in which Mercury's surface is observed, leaving a big hole in the coverage of all 58 day periodic signals such as the signal of the obliquity on our measurements (for any obliquity orientation). The Jupiter and Venus librations cannot be solved for in an efficient way even for the altitude unlimited scenario unless the data volume reaches the highest target numbers studied here, even though the obliquity and annual libration are correctly solved for (and not limiting the solution of the long period librations which are weaker signals in comparison to the obliquity and annual libration amplitude). It seems highly impractical to plan around 5000 dedicated imaging opportunities distributed over around 3100 orbits to reach this goal. Lower altitude scenarios provide less image-pair opportunities and are therefore limited to error levels at least one order of magnitude greater. A forced change in orbital parameters should be applied to enable low-altitude observations on the orbital *aposide*. This suggests that the ESBS orbit considered as a mission backup orbit in case of mass budget

[8] Aposide: The part of the orbit of the spacecraft that is closer to its apocenter than pericenter.

[9] The secular periherm drift is a function of the semi-major axis, the orbital eccentricity and the orbital inclination. The change from the ESAS to the ESBS orbit correspond to a raise in semi-major axis and eccentricity resulting in a reduction of the secular drift.

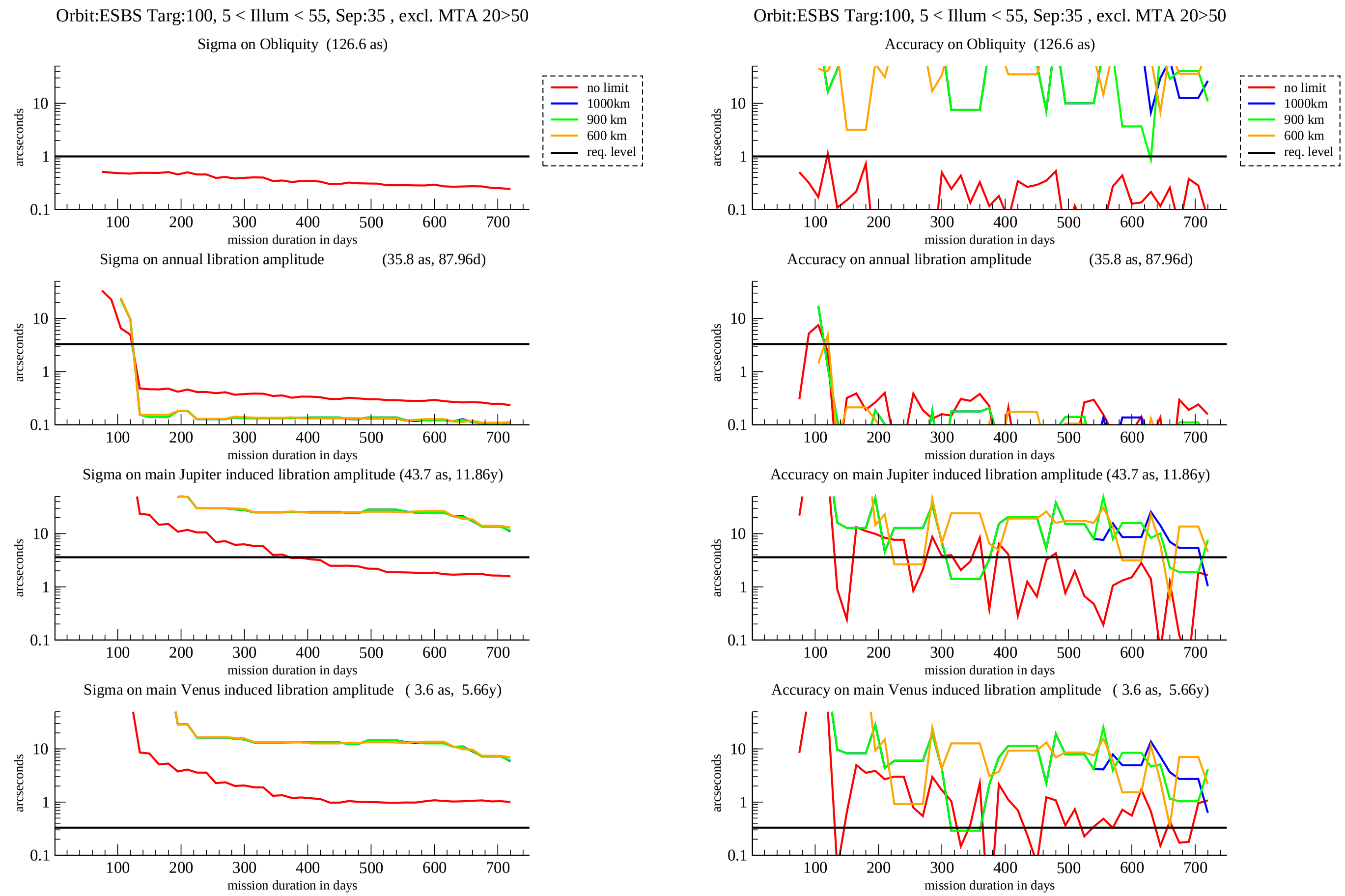

(a) Formal errors

(b) True errors

Figure 5.12: From top to bottom the four parameters we solve for: obliquity, annual libration amplitude, Jupiter induced libration amplitude and Venus induced libration amplitude, as a function of the mission duration for a **fixed number of 100 targets**. The black curve represents the error level required for a successful experiment. The maximum altitude reached by the BC MPO for the ESBS orbit is 2349 km. The blue, green and orange curves represent altitude limits of respectively 1000 km, 900 km and 600 km on the observations used. The red curve represents the *unlimited* scenario.

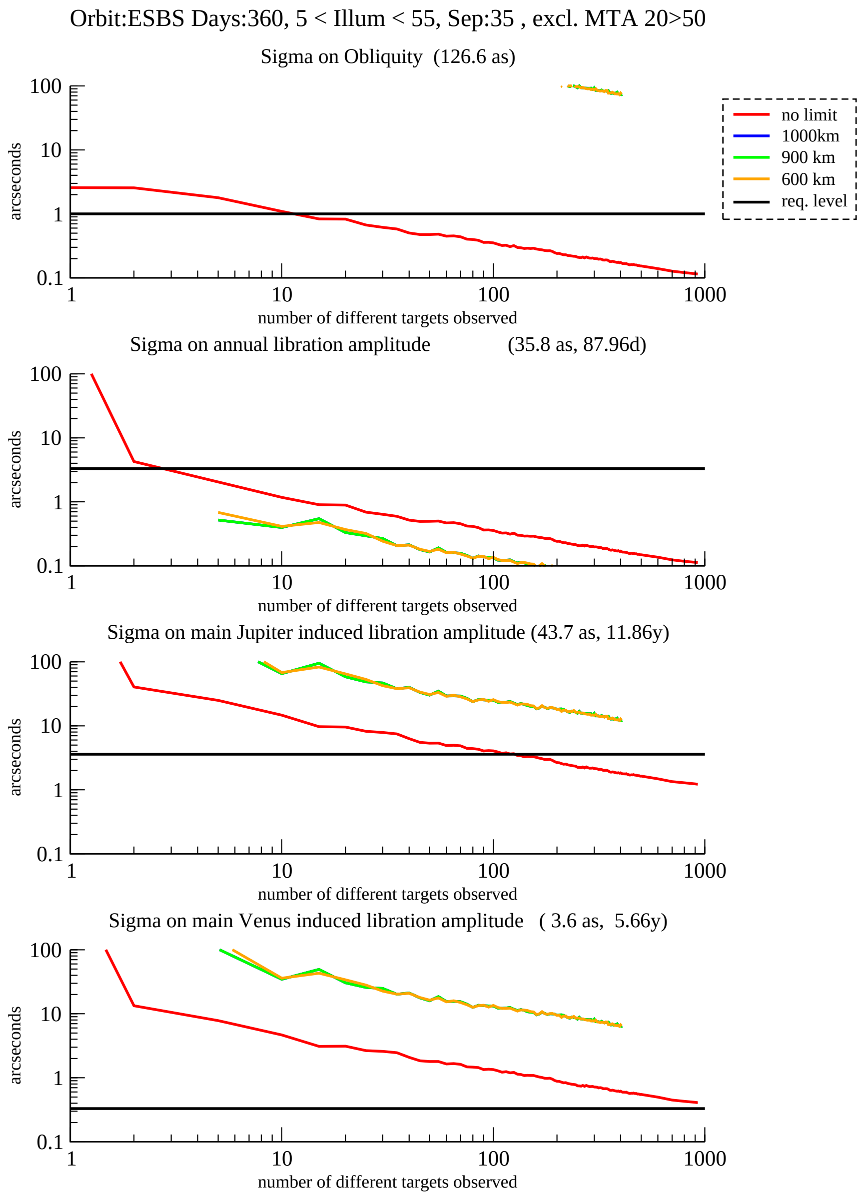

Figure 5.13: From top to bottom the **formal error (1σ)** on the four parameters we solve as a function of the number of targets used to obtain the solution: obliquity, annual libration amplitude, Jupiter induced libration amplitude and Venus induced libration amplitude. The black curve represents the error level required for a successful experiment. The red curve represents the *unlimited* scenario where images are not filtered based on the altitude. The blue, green and orange curve represent altitude limits of respectively 1000 km, 900 km, and 600 km.

increases is not a good choice if the precise determination of the obliquity is to be kept as a mission goal. Contrary to the three other parameters, the annual libration amplitude will be solved for with almost identical quality for both high and low altitude scenarios even for short mission durations and low target numbers (~ 100).

This represents a dramatic change in comparison with the results obtained in the previous section for the nominal ESAS orbit. The orbital change from ESAS to ESBS through a simple apocenter raise would be very damaging to the goals of the BepiColombo rotation experiment. Maybe some complex MPO orbit management could enable a successful experiment outcome, but this seems highly unlikely both because this would demand a lot of the spacecraft resources for this experiment only (assuming no other experiment has identical needs) and because the ESBS orbit is a backup scenario should the orbiter be at the high range of its allocated mass budget (and thus not have many resources to spare).

5.2.3 Less polar orbit

The incentive to discuss the slightly non-polar orbital plane scenario (ES85) is to increase the number of low latitude groundtrack crossings, thus boosting the number of potential image-pairs closer to the equator at the detriment of high latitudes (>60°) which are unfit for our illumination conditions anyway. This orbital choice should enable a better resolution of the obliquity for low altitude restricted datasets, because of the existence of a precession of the spacecraft's orbital plane at a rate of $\sim 12°$ per year enabling the observation of different latitudes at different Mercury mean anomalies with respect to the nominal ESAS orbit.

The formal error as a function of the mission duration for a fixed number of 100 image-pairs represented in fig.5.14(a) compared to the corresponding figure for the ESAS nominal orbit (fig.5.8(a)) shows that the obliquity estimation for the altitude restricted scenarios is delivering better results for the inclined orbit. The unlimited altitude results are quasi identical with those from the ESAS orbit for all parameters. For the annual libration the ES85 orbit delivers better results up to 300 mission days but whereas the ESAS results get better for longer mission durations, the ES85 results stagnate at the precision level reached early on in the mission. Both *minor libration* amplitudes are better resolved earlier on with the ES85 orbit, but after a long enough duration the ESAS results are the same (~ 500 days). Delivering better results on the short term only compared to the ESAS orbit could be a big advantage if the mission does not survive its nominal mission duration of 360 days. In a harsh radiation environment (both electromagnetic and particle) such as around Mercury it should be expected that the spacecraft could fail after the nominal mission and not survive for decades like Mars orbiters which evolve in a very calm radiation environment. Still the ES85 orbit does not reach the minimal precision level needed on the obliquity for the experiment to achieve its minimal goals, and

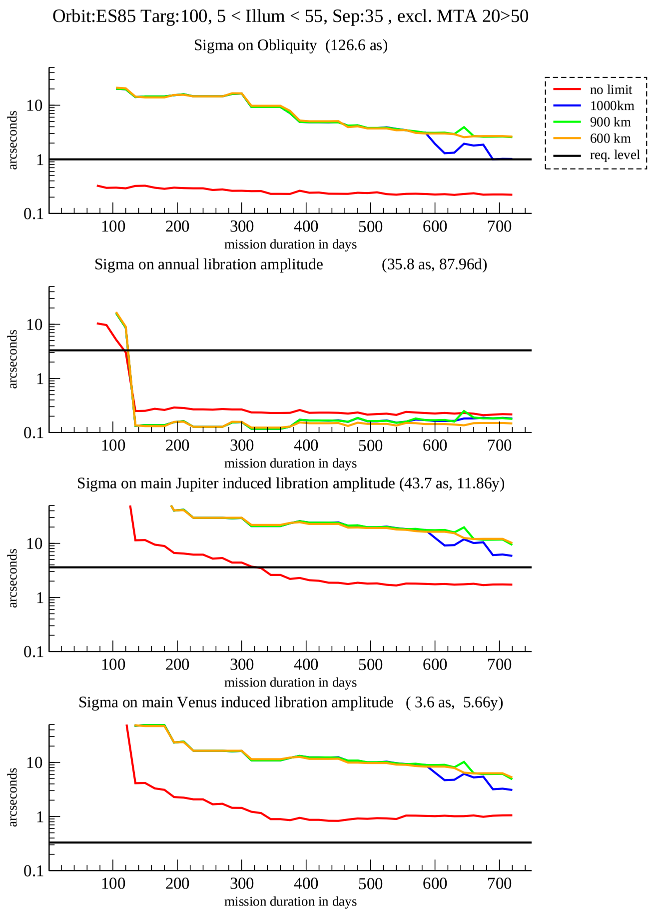

(a) Formal errors

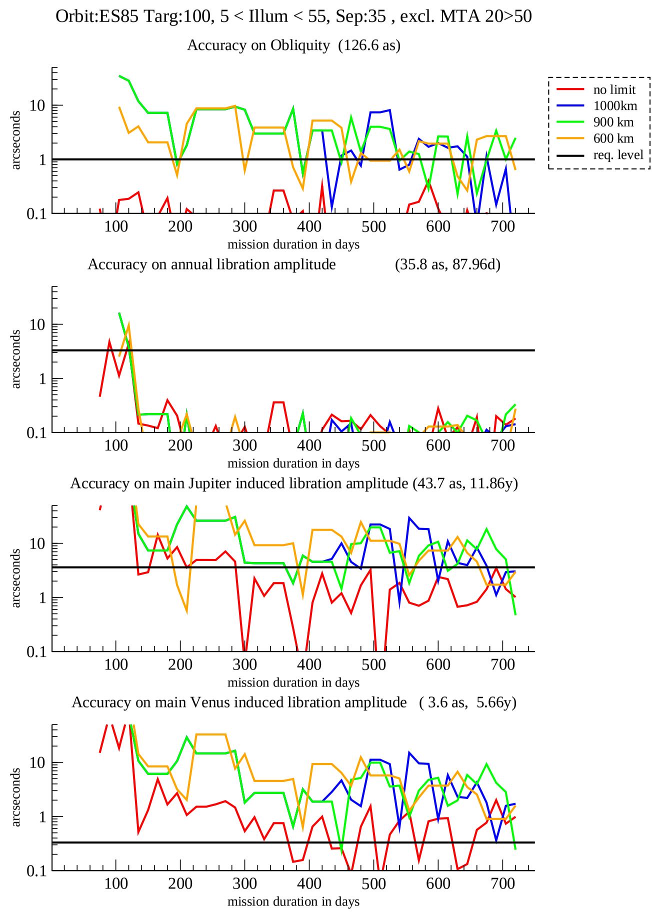

(b) True errors

Figure 5.14: From top to bottom the four parameters we solve for: obliquity, annual libration amplitude, Jupiter induced libration amplitude and Venus induced libration amplitude, as a function of the mission duration for a **fixed number of 100 targets** and for the **ES85** orbit. Each plot contains four coloured lines representing each a different upper altitude limit on the observations taking part in the result. The black line represents the required precision level for a successful experiment.

error levels on both planetary librations are hovering around 100% up to 500 mission days (fig.5.14(a)), where the ESAS error levels get better (fig.5.8(a)).

The Jupiter libration can be accurately solved for only in an altitude unlimited scenario. All other *planetary* libration estimation coupled to any altitude limitation result in worse results than for the nominal scenario. Surprisingly this orbit configuration delivers a very powerful way to solve for the annual libration amplitude with unprecedented accuracy. Unfortunately this comes at the price of heavily impairing the solution of the planetary librations over the course of a nominal mission duration. This last fact rules out any important orbital plane inclination for the BepiColombo MPO as a means to achieve better scientific results for the rotation experiment.

The obliquity is identically solved for, for all altitude limitations up to around 600 mission days. The solution for the nominal maximum altitude of 1000km is a lot better than for the nominal orbit but never fully reaches the *1 arcsec* required by the experiment (see eq.5.10).

5.2.4 Orbits with differing β-angle

In the previous chapter we discussed some orbits with a different β-angle and showed that only $\beta = 0$ delivered a significant amount of observations after 360 mission days. The consequence of this lack of data cannot be seen in fig. (5.15) for which $\beta = 20°$. All parameters can be solved for efficiently to similar precision levels and in similar mission durations as for the nominal ESAS orbit. This indicates primarily that small variations of β will not have a serious degradation effect with respect to the nominal mission configuration.

If we take $\beta = -20°$ through the ESM2 orbit all four graphs look very much like the ones for the nominal case and ESS2 case (see fig 5.16). Without any altitude limit all four parameters are solved for very early in the mission (after one Mercury day we reach the minimal precision level on all of them) as for the nominal orbit. Limiting the altitude to 1000km we reach similar levels of precision after 420 days compared to over 500 for the nominal case. After 720 mission days both mission scenarios (ESM2 and ESAS) give nearly identical results. The main difference resides in the longer time span needed for the ESM2 orbit to reach a good precision level on the annual libration: around 220 days instead of 150 days for the nominal scenario (observations limited to 1000km of altitude).

Table (5.1) presents the respective true and formal error on each parameter for different β- angles. No β-angle deviation greater than $\pm 90°$ is studied because of the mission constraint forbidding the spacecraft periherm to be located over the sun-lit side of Mercury while the planet is at perihelion. This requirement guarantees that the highest planetary thermal flux reached at perihelion does not damage the nadir pointing instruments. A β-angle of $+90°$ corresponds to an orbit where the MPO periherm is *in front* of Mercury on its orbital path, and flying above the *sunrise terminator* at the Mercury perihelion. The

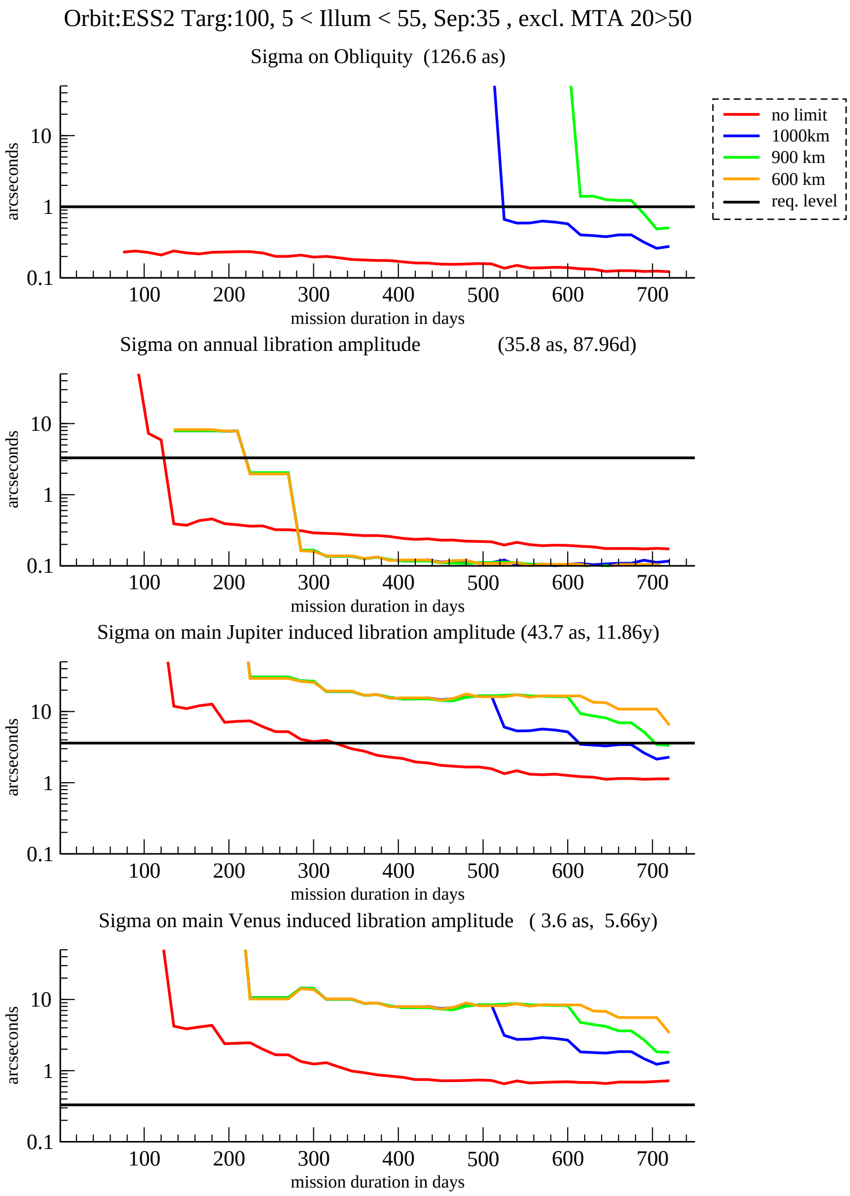

Figure 5.15: From top to bottom the four parameters we solve for, as a function of the mission duration for a **fixed number of 100 targets** and the **ESS2 orbit**. **The results presented here correspond to the ESS2 orbit**, which has a shift in β-angle of +20° relative to the ESAS orbit. Each plot contains four lines representing each a different upper altitude limit on the observations taking part in the result. The black horizontal line represents the minimum mission requirement on each parameters precision.

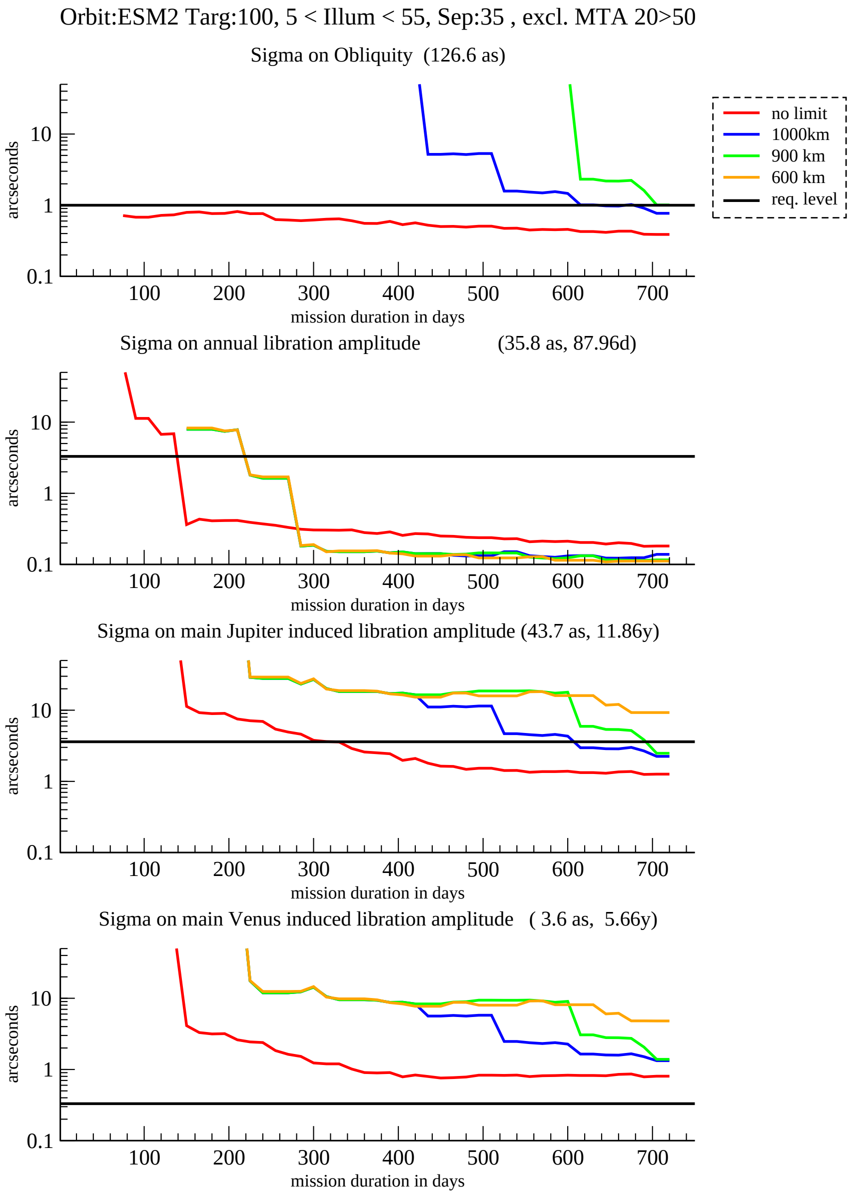

Figure 5.16: Formal errors on the parameters for the ESM2 orbital scenario. From top to bottom the four parameters we solve for, as a function of the mission duration for a fixed number of 100 targets. Each plot contains four lines representing each a different upper altitude limit on the observations taking part in the result.

Parameter	Symbol	ESAS	ESS2	ESS5	ESS9	ESM2	ESM5	ESM9
β-angle	β	0	20	50	90	-20	-50	-90
Formal error								
Obliquity	η	243.6	417.0	267.0	-	224.2	203.3	-
Ann. lib. amp.	$\gamma_☿$	0.15	0.13	0.26	-	0.16	0.39	-
Jupiter	$\gamma_♃$	19.3	19.5	16.8	-	20.5	21.6	-
Venus	$\gamma_♀$	10.2	10.2	8.7	-	10.6	11.1	-
True error								
Obliquity	η	126.6	-215.4	-88.7	-	37.0	43.3	-
Ann. lib. amp.	$\gamma_☿$	0.11	0.11	0.19	-	-0.05	0.05	-
Jupiter	$\gamma_♃$	0.6	4.6	6.2	-	-0.06	-1.4	-
Venus	$\gamma_♀$	-0.6	-2.6	-4.0	-	0.4	0.7	-
num. of obs.	n	119	113	126	0	111	111	0

Table 5.1: This table presents the respective true and formal error on each parameter for different beta angles after 360 mission days and using image-pairs generated from the observations of 100 targets at the planetary surface. **All errors are expressed in arcseconds**.

image-pairs used for the above comparison are not coming from an *identical* set of 100 targets on the planetary surface, but represent the total image-pair volume from 100 observed targets among a surveyed set of 10000 targets (subset). This choice enables us to compare the parameter-resolution-potential of each different mission scenario based on volumes of data which are close to identical for each. Our hypothesis is that the potential useful targets on the planetary surface are abundant and homogeneously distributed over the planetary surface. The important fact that is to be retained from the above table is that the best libration estimates under nominal observation conditions are made for *small* β-angles, close to zero. The best obliquity estimates are for their part made for β-angles between $-20°$ and $-50°$.

Chapter 6

Conclusions

In the frame of this work the BepiColombo rotation experiment has been simulated in order to assess the ability to attain the mission goals and to help lay out a series of constraints on the experiments possible progress. In this experiment pairs of images of identical surface regions taken at different epochs are used to retrieve information on Mercury's rotation and orientation (see chapter 3 for a detailed discussion of the process). The idea is that if we can observe a same patch of Mercury's surface at two different epochs a differential movement with respect to the uniform rotation will appear. Similarly, differences in position with respect to a *zero obliquity model* for the orientation of Mercury can be studied. Important criteria on the spacecraft orbit, to guarantee enough data volume through surface observation opportunities evenly distributed in time have been isolated (see chapter 3). The nominal image illumination constraints used in this study greatly reduce the surface regions that can be entered into consideration for target selection as well as the number of image pairs that can be made from these targets over a nominal mission duration of 360 days. This explains the relative insensitivity of the observable surface regions to *important* changes in true anomaly exclusion constraints as their consequences manifest themselves mainly outside of the observable region.

The BepiColombo orbit characteristics proposed by ESA were used in order to show their impact on the quality of the parameter restitution using the libration experiment observables. By simulating the spacecraft path above the surface of the planet and considering surface illumination conditions required for the image matching process, the distribution of potential images on the surface has been obtained. The uncertainty on the satellite position and orientation (imposed by the precision of the star tracker and radio science observations) is included by subjecting each potential image to a positioning error. In practise, the location and time of possible repeated photographic measurements of selected target positions on the surface of Mercury have been simulated and used for determining the rotation parameters. By means of a least squares process, three libration amplitudes and the obliquity as well as formal errors on these quantities are estimated. The accuracy of the estimated parameters of the rotational motion of Mercury has been studied as a function of the quantity of measurements made, the number of different targets considered and their locations on the surface of the planet. As the libration is a longitudinal motion, shifts between images are larger at lower latitudes. Therefore, images of near-equatorial regions will be of greater importance to the rotational experiment. The precision on the estimated libration amplitude also depends on the number of possible images of the same target used. In chapter 3 it has been shown that all ESA proposed orbits yield more usable image pairs at latitudes between 30° North and 30° South.

The criteria for the best determination of the obliquity are different from those of libration because the surface displacement caused by the obliquity is larger for higher latitudes, contrary to libration. The incompatible optimal requirements for obliquity and libration set additional constraints on the strategy to obtain both quantities from this image based experiment. The quality of the spacecraft positioning is very important since it greatly influences the ability to position the images taken by the spacecraft on the planetary surface and hence to estimate the planetary rotation. It is worth to remember that we have considered a worst case scenario for the magnitudes of each individual observation error. This was done in order to guarantee not to be overly optimistic in terms of the quality of the estimation process because of the basic error model used (see section 3.7).

By determining criteria for the distribution and number of target positions to maximise the precision and accuracy on the determination of the libration amplitude and obliquity the constraints on the interior structure of the planet can be optimised. Several parameters influence the quality of the libration and obliquity restitution directly and indirectly through the limitation of the surface observability. These are:

- the mission duration,
- the number of targets observed,
- the altitude limit imposed on surface observations,
- the size of the Mercury true anomaly exclusion zone,
- the surface illumination conditions,
- and all orbital parameters.

All influence the surface regions that are observable as well as the timing of the observations made of these regions. The nominal illumination constraints we consider are the dominant factor in reducing the size of, and observation volume inside of the observable surface zones. The altitude limit and true anomaly exclusion zones are the main culprits hindering a good estimation of the obliquity[1] and as a consequence also the two long period planetary induced librations. The latter are very faint signals that can only be reliably solved for if the annual libration amplitude <u>and</u> the obliquity are well determined.

6.1 Nominal mission

The nominal orbit chosen by ESA has been shown to be an ideal case for the libration and obliquity determination process from a purely geometrical point of view. After having studied the nominal mission scenario a number of conclusions have been reached:

- No accurate obliquity estimation is possible in 360 mission days if the observations are limited below 1000 km in altitude. If this limit is to be respected only a mission extension to over 540 days will enable a good enough obliquity estimate. After about 500 days the natural periherm drift of the orbit will bring low orbit altitudes onto the "aposide" of the BepiColombo orbit, enabling low altitude observations of some surface regions at a new Mercury true anomaly. In order to obtain an accurate obliquity estimate in less than 360 mission days high altitude observation of the surface made at the Mercury perihelion are needed.
- The annual libration amplitude is well solved for in almost all circumstances reaching error levels of around 1 arcsecond in true and formal error after less than 360 days and for data sets limited to 25 targets only.
- The main Jupiter and Venus induced libration amplitudes are best estimated for longer mission durations because of their long periods. As long as the obliquity is not well solved for it is impossible to obtain accurate estimations of these two parameters. The amplitude of the Jupiter induced libration is expected to be of the order of the annual libration amplitude, because the free libration period of Mercury is expected very close to the Jupiter induced libration period. A good estimation of the Jupiter libration amplitude is possible under nominal conditions (as long as the obliquity is well resolved) and could deliver a constraint on the value of the free libration period. The "Venus libration amplitude" is ten times smaller than the annual libration amplitude and cannot (even for longer mission durations) be solved for accurately enough to deliver an independent constraint on the interior parameters of Mercury. The error levels never dip below 50% of the libration amplitude.

The nominal mission scenario is not able to solve for the two *main* parameters during the nominal 360 day mission. This effect can be eliminated by including high altitude measurements (> 1000 *km*) of the surface made close to the

[1]By good estimation we mean a solution satisfying the mission requirements in terms of precision.

Mercury perihelion passage, thereby *filling the gap* in the data hindering a good resolution of Mercury's obliquity.

6.2 Perspectives

6.2.1 Other means of libration determination

Besides the rotation experiment as studied in this work, which uses the camera, the radio science and star tracker data, Mercury's libration amplitude and obliquity can be determined through other means available through the BepiColombo MPO.

Altimetry

One possible alternative makes use of BELA altimeter data (see *Koch et al.* (2008)). The BepiColombo Laser Altimeter (BELA) is designed to map Mercury's topography with an accuracy better than 10 meters. Its primary goal is to determine the global static topography, which, in combination with the gravity field, allows inferring some aspects of the internal structure, such as the crustal density and lithospheric thickness variations. Superimposed on the static topography are the time-dependent tidal changes and a longitudinal shift of the topography due to libration, which can be treated as a time-dependent variation of topography. Additionally, time deviations of altimetry crossover positions can be used to infer information on the librations of Mercury. This method measures the difference in actual and expected time of the repeated overflight of a certain surface target, in a similar way to the previously described image based technique. The simulations performed at ROB demonstrate that the use of crossover data improves the estimates of the observed libration amplitude and obliquity of Mercury. The Laser altimetry can work independently of the surface illumination offering a complementary dataset to the image-only based experiment.

Radio science

The MORE radio science experiment will enable a very accurate positioning of the BepiColombo MPO of about 3 meters up to 10 cm when tracked from Earth. This will enable to determine very accurately the coefficients of Mercury's gravity field up to degree and order 25 (*Milani et al.* 2001), as well as the time dependence for the lowest degrees of the gravity field. The libration motion of the planet underneath the spacecraft can be treated as a time-varying contribution to the gravitational field. The small variations of the gravitational field due to the libration may be be "felt" by the spacecraft. We can thus solve for a time-dependent gravitational field, and relate this to the libration amplitude.

6.2.2 Immediate perspectives of the project

A direct consequence of this work is to assess possible improvements in the determination of the libration amplitudes and obliquity through the joint use of the camera/radio science/star-tracker data (as studied in this work), the BELA altimeter data or cross-tracks, and the perturbations of the coefficients of the gravitational field (as described above). It should first be investigated whether these other BepiColombo measurements could complement or be jointly used with the images on which the rotation experiment, currently foreseen for the determination of the libration, is based. An advantage of the laser altimetry and/or radio science is that they do not depend on the solar incidence angle at the surface and on the presence of sufficiently large surface features such as craters or albedo spots. We propose to extend the study performed with the camera/radio-science/star-tracker data by using the same approach as for the image-based method in order to treat simulated altimetry data. Each altimeter measurement point representing a small image of the surface. Similarly the approach could be used on simulated gravity data. With the three alternative methods (using camera data, altimetry data, and/or gravity data) it will be possible to assess whether a better accuracy would be obtained with one of the alternative methods alone or with the combinations of two methods or the use of all three of them. The additional evaluation of the relative contributions of the different methods to the final result will enable us to determine their optimal combination.

As a more distant perspective that can be envisaged later we should mention the application of all the methods mentioned above to other objects of the Solar system such as the moons of Jupiter and Saturn, which also exhibit large amplitude librations, in order to optimize the scientific return of future missions in terms of the moon's interior (e.g. librations are enhanced by the presence of a subsurface ocean beneath the icy crust). Currently a mission to the satellites of Jupiter is under study by both NASA and ESA (JESM / Jupiter-Europa System Mission), and this additional work could be integrated into that mission.

Bibliography

Anderson, J. D., G. Colombo, P. B. Espsitio, E. L. Lau, and G. B. Trager (1987), The mass, gravity field, and ephemeris of Mercury, *Icarus*, *71*, 337–349, doi:10.1016/0019-1035(87)90033-9.

Cassini, G. D. (1693), *Traité de l'origine e de Progrès de l'astronomie*.

Chapman, C. R. (1988), *Mercury - Introduction to an end-member planet*, pp. 1–23, Mercury, University of Arizona Press.

Colombo, G. (1965), Rotational Period of the Planet Mercury, *Nature*, *208*, 575–+, doi:10.1038/208575a0.

Colombo, G. (1966), Cassini's second and third laws, *Astronomical Journal*, *71*, 891–+, doi:10.1086/109983.

Correia, A. C. M., and J. Laskar (2004), Mercury's capture into the 3/2 spin-orbit resonance as a result of its chaotic dynamics, *Nature*, *429*, 848–850, doi:10.1038/nature02609.

Correia, A. C. M., and J. Laskar (2009), Mercury's capture into the 3/2 spin-orbit resonance including the effect of core-mantle friction, *Icarus*, *201*, 1–11, doi:10.1016/j.icarus.2008.12.034.

D'Hoedt, S., and A. Lemaitre (2004), The Spin-Orbit Resonant Rotation of Mercury: A Two Degree of Freedom Hamiltonian Model, *Celestial Mechanics and Dynamical Astronomy*, *89*, 267–283, doi: 10.1023/B:CELE.0000038607.32187.d4.

D'Hoedt, S., and A. Lemaître (2008), Planetary long periodic terms in Mercury's rotation: a two dimensional adiabatic approach, *Celestial Mechanics and Dynamical Astronomy*, *101*, 127–139, doi:10.1007/s10569-007-9115-4.

D'Hoedt, S., A. Lemaitre, and N. Rambaux (2006), Note on Mercury's rotation: the four equilibria of the Hamiltonian model, *Celestial Mechanics and Dynamical Astronomy*, *96*, 253–258, doi:10.1007/s10569-006-9041-x.

D'Hoedt, S., B. Noyelles, J. Dufey, and A. Lemaitre (2009), Determination of an instantaneous Laplace plane for Mercury's rotation, *Advances in Space Research*, *44*, 597–603, doi:10.1016/j.asr.2009.05.008.

Dufey, J., A. Lemaître, and N. Rambaux (2008), Planetary perturbations on Mercury's libration in longitude, *Celestial Mechanics and Dynamical Astronomy*, *101*, 141–157, doi:10.1007/s10569-008-9143-8.

Dufey, J., B. Noyelles, N. Rambaux, and A. Lemaître (2009), Latitudinal librations of Mercury with a fluid core, *Icarus*, *203*.

Garcia, D., P. de Pascale, and R. Jehn (2007), BepiColombo Mercury Cornerstone Consolidated Report on Mission Analysis, *MAO Working Paper No. 466 BC-ESC-RP-05500, Issue 1.4*, ESOC, Robert-Bosch-Str. 5, 64293 Darmstadt, Germany.

Goldreich, P., and S. Peale (1966), Spin-orbit coupling in the solar system, *Astronomical Journal*, *71*, 425–+, doi:10.1086/109947.

Harder, H., and G. Schubert (2001), Sulfur in Mercury's Core?, *Icarus*, *151*, 118–122, doi:10.1006/icar.2001.6586.

Holin, I. (1999), Very long baseline interferometry for investigation of Mercury's spin and interior, *Uspeckhi Sovremennoi Radioelectroniki*, *7*, 16–28, in Russian.

Jault, D., C. Gire, and J. L. Le Mouel (1988), Westward drift, core motions and exchanges of angular momentum between core and mantle, *Nature*, *333*, 353–356, doi:10.1038/333353a0.

Jehn, R., C. Corral, and G. Giampieri (2004), Estimating Mercury's 88-day libration amplitude from orbit, *Planetary and Space Science*, *52*, 727–732, doi: 10.1016/j.pss.2003.12.012.

Jorda, L., and N. Thomas (2000), The accuracy of pattern matching techniques for the radio science experiment of ESAs Mercury Cornerstone mission., *Preliminary study (not published), Max-Planck Institute for Aeronomie,Katlenburg-Lindau, Germany*.

Kaula, W. M. (1966), *Theory of satellite geodesy. Applications of satellites to geodesy*, Waltham, Mass.: Blaisdell.

Koch, C., R. Kallenbach, and U. Christensen (2008), Simultaneous Determination of global Topography, tidal Love number and libration amplitude of Mercury by Laser altimetry, *Planetary and Space Science*, *56*, doi: 10.1016/j.pss.2008.04.002.

Konopliv, A. S., W. B. Banerdt, and W. L. Sjogren (1999), Venus Gravity: 180th Degree and Order Model, *Icarus*, *139*, 3–18, doi:10.1006/icar.1999.6086.

Konopliv, A. S., S. W. Asmar, E. Carranza, W. L. Sjogren, and D. N. Yuan (2001), Recent Gravity Models as a Result of the Lunar Prospector Mission, *Icarus*, *150*, 1–18, doi:10.1006/icar.2000.6573.

Konopliv, A. S., C. F. Yoder, E. M. Standish, D. Yuan, and W. L. Sjogren (2006), A global solution for the Mars static and seasonal gravity, Mars orientation, Phobos and Deimos masses, and Mars ephemeris, *Icarus*, *182*, 23–50, doi: 10.1016/j.icarus.2005.12.025.

Lemoine, F. G., S. C. Kenyon, J. C. Factor, N. K. Trimmer, N. K. Pavlis, D. S. Chinn, C. M. Cox, S. M. Klosko, S. B. Luthcke, M. H. Torrence, R. G. Wang, R. G. Williamson, E. C. Pavlis, R. H. Rapp, and T. R. Olson (1998), The Development of the Joint NASA GSFC and NIMA Geopotential Model EGM96, *NASA Goddard Space Flight Center, Greenbelt, Maryland, 20771 USA*.

Lewis, J. S. (1988), *Origin and composition of Mercury*, pp. 651–666, Mercury, University of Arizona Press.

Ma, C., E. F. Arias, T. M. Eubanks, A. L. Fey, A. Gontier, C. S. Jacobs, O. J. Sovers, B. A. Archinal, and P. Charlot (1998), The International Celestial Reference Frame as Realized by Very Long Baseline Interferometry, *The Astronomical Journal*, *116*, 516–546, doi:10.1086/300408.

Margot, J.-L., S. J. Peale, R. F. Jurgens, M. A. Slade, and I. V. Holin (2007a), Large Longitude Libration of Mercury Reveals a Molten Core, in *AAS/Division of Dynamical Astronomy Meeting*, *AAS/Division of Dynamical Astronomy Meeting*, vol. 38, pp. 07.01–+.

Margot, J. L., S. J. Peale, R. F. Jurgens, M. A. Slade, and I. V. Holin (2007b), Large Longitude Libration of Mercury Reveals a Molten Core, *Science*, *316*, 710–, doi:10.1126/science.1140514.

Milani, A., A. Rossi, D. Vokrouhlický, D. Villani, and C. Bonanno (2001), Gravity field and rotation state of Mercury from the BepiColombo Radio Science Experiments, *Planetary and Space Science*, *49*, 1579–1596.

Peale, S. J. (1969), Generalized Cassini's Laws, *Astronomical Journal*, *74*, 483–+, doi:10.1086/110825.

Peale, S. J. (1974), Possible histories of the obliquity of Mercury, *Astronomical Journal*, *79*, 722–+, doi:10.1086/111604.

Peale, S. J. (1976), Inferences from the dynamical history of Mercury's rotation, *Icarus*, *28*, 459–467, doi:10.1016/0019-1035(76)90119-6.

Peale, S. J. (1988), *The rotational dynamics of Mercury and the state of its core*, pp. 461–493, Mercury, University of Arizona Press.

Peale, S. J. (2005), The free precession and libration of Mercury, *Icarus*, *178*, 4–18, doi:10.1016/j.icarus.2005.03.017.

Peale, S. J. (2006), The proximity of Mercury's spin to Cassini state 1 from adiabatic invariance, *Icarus*, *181*, 338–347, doi:10.1016/j.icarus.2005.10.006.

Peale, S. J., R. J. Phillips, S. C. Solomon, D. E. Smith, and M. T. Zuber (2002), A procedure for determining the nature of Mercury's core, *Meteoritics and Planetary Science*, *37*, 1269–1283.

Peale, S. J., M. Yseboodt, and J. Margot (2007), Long-period forcing of Mercury's libration in longitude, *Icarus*, *187*, 365–373, doi: 10.1016/j.icarus.2006.10.028.

Peale, S. J., J. L. Margot, and M. Yseboodt (2009), Resonant forcing of Mercury's libration in longitude, *Icarus*, *199*, 1–8, doi:10.1016/j.icarus.2008.09.002.

Pettengill, G. H., and R. B. Dyce (1965), A Radar Determination of the Rotation of the Planet Mercury, *Nature*, *206*, 1240–+, doi:10.1038/2061240a0.

Pfyffer, G., N. Rambaux, A. Rivoldini, T. van Hoolst, and V. Dehant (2006), Determination of libration amplitudes from orbit, in *European Planetary Science Congress 2006*, pp. 568–+.

Pfyffer, G., T. van Hoolst, and V. Dehant (2008), Libration and obliquity of Mercury from the BepiColombo radio science and camera experiments, *AGU Fall Meeting Abstracts*, pp. A6+.

Pfyffer, G., T. van Hoolst, and V. Dehant (2009), Libration and obliquity of Mercury from the BepiColombo radio science and camera experiments, in *European Planetary Science Congress 2009, held 14-18 September in Potsdam, Germany. http://meetings.copernicus.org/epsc2009, p.371*, pp. 371–+.

Rambaux, N., and E. Bois (2004), Theory of the Mercury's spin-orbit motion and analysis of its main librations, *Astronomy and Astrophysics*, *413*, 381–393, doi:10.1051/0004-6361:20031446.

Rambaux, N., T. Van Hoolst, V. Dehant, and E. Bois (2007), Inertial core-mantle coupling and libration of Mercury, *Astronomy and Astrophysics*, *468*, 711–719, doi:10.1051/0004-6361:20053974.

Rivoldini, A., T. Van Hoolst, and O. Verhoeven (2009), The interior structure of Mercury and its core sulfur content, *Icarus*, *201*, 12–30, doi: 10.1016/j.icarus.2008.12.020.

Schubert, G., M. N. Ross, D. J. Stevenson, and T. Spohn (1988), *Mercury's thermal history and the generation of its magnetic field*, pp. 429–460, Mercury, University of Arizona Press.

Seidelmann, P. K., V. K. Abalakin, M. Bursa, M. E. Davies, C. de Bergh, J. H. Lieske, J. Oberst, J. L. Simon, E. M. Standish, P. Stooke, and P. C. Thomas (2002), Report of the IAU/IAG Working Group on Cartographic Coordinates and Rotational Elements of the Planets and Satellites: 2000, *Celestial Mechanics and Dynamical Astronomy*, *82*, 83–111.

Sohl, F., and G. Schubert (2007), *Interior Structure, Composition, and Mineralogy of the Terrestrial Planets*, vol. 10, pp. 27–68, Treatise On Geophysics, Elsevier.

Solomon, S. C., R. L. McNutt, R. E. Gold, M. H. Acuña, D. N. Baker, W. V. Boynton, C. R. Chapman, A. F. Cheng, G. Gloeckler, J. W. Head, III, S. M. Krimigis, W. E. McClintock, S. L. Murchie, S. J. Peale, R. J. Phillips, M. S. Robinson, J. A. Slavin, D. E. Smith, R. G. Strom, J. I. Trombka, and M. T. Zuber (2001), The MESSENGER mission to Mercury: scientific objectives and implementation, *Planetary Space Science*, *49*, 1445–1465.

Spohn, T. (1991), Mantle differentiation and thermal evolution of Mars, Mercury, and Venus, *Icarus*, *90*, 222–236, doi:10.1016/0019-1035(91)90103-Z.

Spohn, T., F. Sohl, K. Wieczerkowski, and V. Conzelmann (2001), The interior structure of Mercury: what we know, what we expect from BepiColombo, *Planetary and Space Science*, *49*, 1561–1570.

Stanley, S., J. Bloxham, W. E. Hutchison, and M. T. Zuber (2005), Thin shell dynamo models consistent with Mercury's weak observed magnetic field [rapid communication], *Earth and Planetary Science Letters*, *234*, 27–38, doi: 10.1016/j.epsl.2005.02.040.

Stevenson, D. J., T. Spohn, and G. Schubert (1983), Magnetism and thermal evolution of the terrestrial planets, *Icarus*, *54*, 466–489, doi:10.1016/0019-1035(83)90241-5.

Tiscareno, M. S., P. C. Thomas, and J. A. Burns (2009), The rotation of Janus and Epimetheus, *Icarus*, *204*, 254–261, doi:10.1016/j.icarus.2009.06.023.

Van Hoolst, T. (2007), *The Rotation of the Terrestrial Planets*, vol. 10, pp. 123–163, Treatise On Geophysics, Elsevier.

Van Hoolst, T., and C. Jacobs (2003), Mercury's tides and interior structure, *Journal of Geophysical Research (Planets)*, *108*, 5121–+, doi:10.1029/2003JE002126.

Van Hoolst, T., F. Sohl, I. Holin, O. Verhoeven, V. Dehant, and T. Spohn (2007), Mercury's Interior Structure, Rotation, and Tides, *SSR*, pp. 155–+, doi:10.1007/s11214-007-9202-6.

Yseboodt, M., and J. Margot (2006), Evolution of Mercury's obliquity, *Icarus*, *181*, 327–337, doi:10.1016/j.icarus.2005.11.024.

Yseboodt, M., J. L. Margot, and S. J. Peale (2009), Model of Mercury's Forced Librations in Longitude, in *AAS/Division for Planetary Sciences Meeting Abstracts*, *AAS/Division for Planetary Sciences Meeting Abstracts*, vol. 41, pp. 67.04–+.